University of Trento
Department of Civil, Environmental and Mechanical Engineering

Doctoral School in
Structural Civil and Mechanical Engineering
XXVII Cycle

Federico Bosi

Eshelby-like forces in elastic structures: theory, experiments and applications

Advisor
Prof. Davide Bigoni

Trento, Saturday 27th December, 2014

University of Trento
University of Bergamo
University of Brescia
University of Padova
University of Trieste
University of Udine
University IUAV of Venezia

Head of the Doctoral School:
Prof. Davide Bigoni   Università di Trento (IT)

Final Examination: Friday 12$^{\text{th}}$ December, 2014

Board of Examiners:
Prof. Ferdinando Auricchio   Università di Pavia (IT)
Prof. Luca Deseri   Università di Trento (IT)
Prof. Sébastien Neukirch   Université Pierre et Marie Curie, Paris (FR)
Prof. Angelo Marcello Tarantino   Università di Modena e Reggio Emilia (IT)

To my family

Summary

The Eshelbian force is the main concept of a celebrated theoretical framework associated with the motion of dislocations and, more in general, defects in solid. Similarly, it is proven that a force driving the configuration of an elastic structure is generated through the motion and release mechanism of flexural and torsional energy. This configurational force, analytically derived through different approaches and experimentally validated, provides counterintuitive but crucial effects in elasticity. In particular, it affects:

◇ equilibrium paths in systems with variable length;

◇ instabilities, bifurcation and restabilization occurring in a structure penetrating in a movable constraint.

Furthermore, this configurational force (called 'Eshelby-like' in analogy to continuum mechanics) opens a totally new perspective in the mechanics of deformable mechanisms, with possible broad applications in:

◇ new weighing devices as the 'elastica arm scale';

◇ torsional locomotion along perfectly smooth channel and configurational actuators, capable of transforming torque into propulsive force.

Acknowledgements

First and foremost, I bring my deepest gratitude to my advisor, Prof. Davide Bigoni, for his remarks, suggestions and encouragements throughout this research work. His constant optimism and overwhelming passion for Mechanics have contribute to my scientific and personal growth.

I am highly thankful to Dr. Francesco Dal Corso and Dr. Diego Misseroni for their precious help and cooperation.

I am deeply grateful to Dr. Luca Argani for his constant help and to all members of the group of Solid and Structural Mechanics at the University of Trento: Prof. Luca Deseri, Prof. Nicola Pugno, Prof. Massimiliano Gei, Prof. Andrea Piccolroaz, Dr. Roberta Springhetti, Irena Jatro. I would like to thank all my colleagues Dr. Mattia Bacca, Dr. Lorenzo Morini, Dr. Andrea Bacigalupo, Dr. Panagiotis Gourgiotis, Ing. Aldo Madaschi, Ing. Summer Shazad, Ing. Eliana Bortot, the people that worked at my group in these years and all my friends.

I would also like to thank Ing. Alessandro Cocquio, Ing. Matteo Cova and all members of Sacmi Imola s.c. for their hospitality and cooperation.

Finally, I am particularly indebted to all my family for their never-ending support and unconditioned love and, I express my thanks to my beloved Martina for her patience and unfailing encouragement.

<div style="text-align:right">

Trento, Saturday 27th December, 2014

Federico Bosi

</div>

Published papers

The main results presented in this thesis have been summarized in the following papers:

⋄ D. Bigoni, F. Dal Corso, F. Bosi and D. Misseroni. "Eshelby-like forces acting on elastic structures: theoretical and experimental proof". In: *Mechanics of Materials* (2015), **80**, pp. 368-374;

⋄ D. Bigoni, F. Bosi, F. Dal Corso and D. Misseroni. "Instability of a penetrating blade". In: *Journal of the Mechanics and Physics of Solids* (2014), **64**, pp. 411-425;

⋄ F. Bosi, D. Misseroni, F. Dal Corso and D. Bigoni. "An Elastica Arm Scale". In: *Proceedings of the Royal Society A* (2014), **470**, 20140232. *Cover Paper. Royal Society Publishing July Highlights*;

⋄ D. Bigoni, F. Dal Corso, D. Misseroni and F. Bosi. "Torsional locomotion". In: *Proceedings of the Royal Society A* (2014), **470**, 20140599.

Other results obtained during the PhD are reported in the following publications:

⋄ F. Bosi, E. Mazzocchi, I. Jatro, F. Dal Corso, A. Piccolroaz, L. Deseri, D. Bigoni, A. Cocquio, M. Cova and S. Odorizzi. "A collaborative project between Industry and Academia to enhance engineering education at graduate and PhD level in ceramic technology". In: *International Journal of Engineering Education* (2013), **29**, pp. 1-9;

⋄ F. Bosi, A. Piccolroaz, M. Gei, F. Dal Corso, A. Cocquio and D. Bigoni. "Experimental investigation of the elastoplastic response of aluminum silicate spray dried powder during cold compaction". In: *Journal of the European Ceramic Society* (2014), **34**, pp. 2633-2642.

Contents

Chapter 1

Introduction

Eshelbian (or configurational) forces have been introduced by Eshelby [1–4] to describe motion of massless (for instance: voids, microcracks, vacancies, or dislocations) or heavy (for instance inclusions) defects within a solid body as a result of mechanical or thermal loading, until an equilibrium configuration is reached. Examples are the crack-extension force of fracture mechanics, the Peach–Koehler force of dislocations, or the material force developing on a phase boundary in a solid under loading. Nowadays configurational forces are the cornerstone of a well-developed theory (see for instance the monographs by Gurtin [5], Kienzler and Herrmann [6], and Maugin [7, 8]).

The aim of this thesis is to prove analytically and experimentally the existence of configurational, and therefore called by analogy 'Eshelby-like', forces acting on elastic structures having a movable smooth and bilateral constraint which can realize the release of elastic energy. Furthermore, its action on extremely deformable systems is investigated in terms of loading paths, instabilities, critical load, bifurcation and restabilization. Finally, application of configurational mechanics to elastic structures will be shown through the deformable arm scale, torsional locomotion and torsional actuator.

The Euler elastica theory is employed in Chapter 2 to solve postcritical behaviour of elastic inextensible planar rods with various boundary conditions loaded with an end thrust. The determination of the equilibrium of beams subject to large deflection is the central thread which runs throughout the present work.

In Chapter 3 it is shown the existence of an 'Eshelby-like' or 'configurational' force in a simple elastic structure, see Fig. 1.1. This unexpected force arises from a smooth and bilateral constraint that leaves the elastic rod the possibility of sliding, thus releasing energy. It is analytically derived both through variational calculus and asymptotic approach and experimentally measured on a model structure designed, realized and tested[1].

---

[1]D. Bigoni, F. Dal Corso, F. Bosi and D. Misseroni. "Eshelby-like forces acting on elastic structures: theoretical and experimental proof". In: *Mechanics of Materials* (2015),
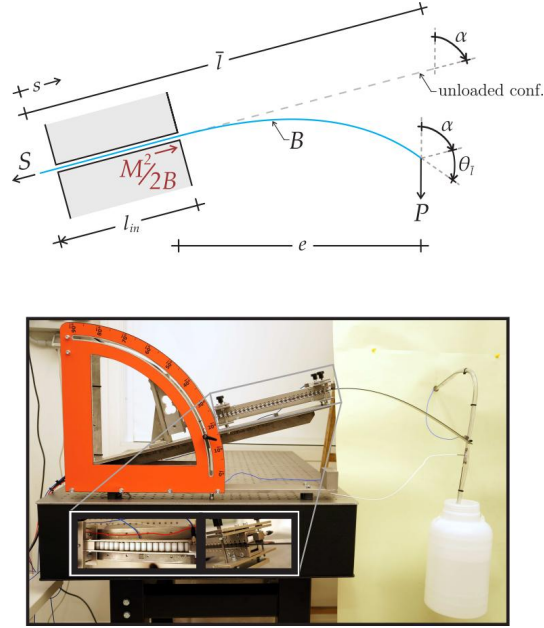
Figure 1.1: Structural scheme (upper) of the elastic system employed to disclose a Eshelby-like force and (lower) its practical realization. The elastic rod of total length $\bar{l}$ is subject to a dead vertical load P on its right end, is constrained with a sliding sleeve inclined at an angle α (with respect to the vertical) and has an axial dead force S applied at its left end. The presence of the Eshelby-like force $M^2/(2B)$ influences the force S at equilibrium, which results different from $P\cos\alpha$, as anyone would conclude from the equilibrium in the sliding direction of the sleeve.

The influence of 'Eshelby-like' force on an elastic rod which can slide into a frictionless sleeve thus varying its length, is analyzed in Chapter 4 with respect to two different loading conditions. In the former, the postcritical behaviour of the system shown in Fig. 1.2 is strongly governed by configurational forces generated by the movable constraint, whereas in the latter, presented in Fig. 1.3, a different loading path (with softening) and a new critical load (more than two times lower) have been discovered with respect to the solution present in technical literature. Due to the presence of 'Eshelby-like' force, both systems exhibit a force reversal, fully substantiated by experimental tests.

Chapter 5 addresses the bifurcation and instability analysis of an elastic rod penetrating into a sliding sleeve ending with a linear elastic spring[2]. This simple elastic system, reported in Fig. 1.4 with its practical realization where experiments have been conducted, shows several unexpected behaviours

---

80, pp. 368-374.

[2]D. Bigoni, F. Bosi, F. Dal Corso and D. Misseroni. "Instability of a penetrating blade". In: *Journal of the Mechanics and Physics of Solids* (2014), **64**, pp. 411-425.
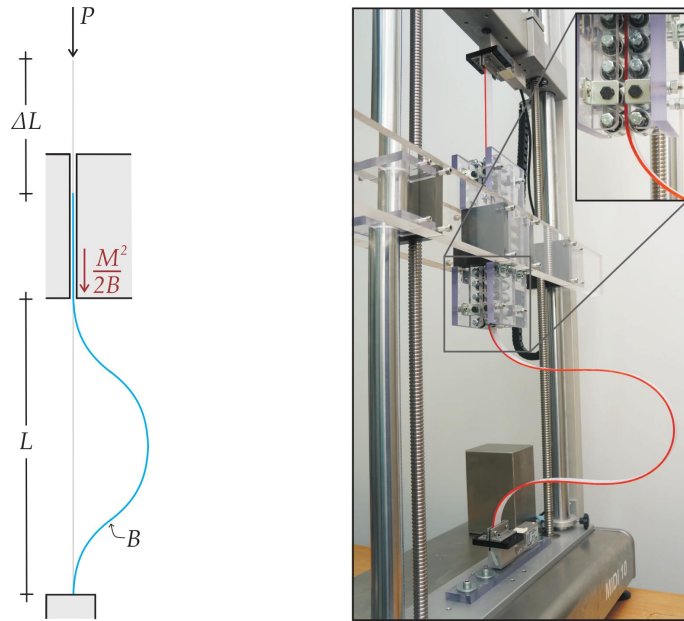
Figure 1.2: The design scheme (left) of the elastic structure with variable length subject to an end thrust P and (right) the experimental set-up. The elastic planar rod of bending stiffness B is restrained by a clamp in its bottom side, while, at a distance L, a frictionless sleeve is attached. The 'Eshelby-like' force acts as an additional axial load for the rod, whose amount changes at varying of the external axial load P.
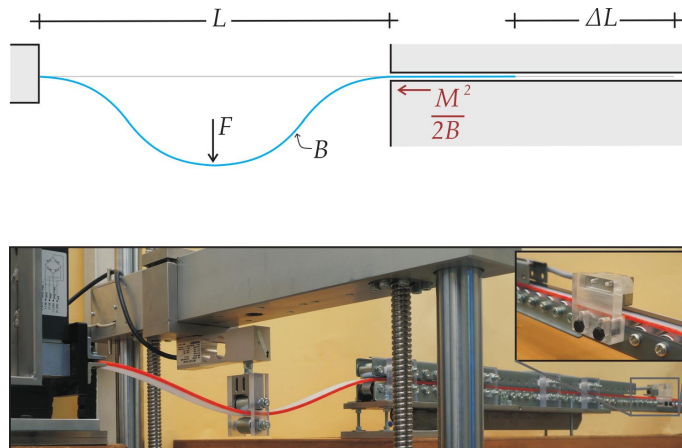
Figure 1.3: The scheme (upper) and the real model (lower) of the elastic structure subject to a concentrated transversal force F. The elastic planar rod of bending stiffness B has its left edge clamped, whereas at the opposite side, at a distance L, it is present a frictionless and bilateral sliding sleeve in which the rod can slide and may change its free deformed length. The 'Eshelby-like' deeply influences the loading path and the critical load of this system, with respect to the solution reported in literature.
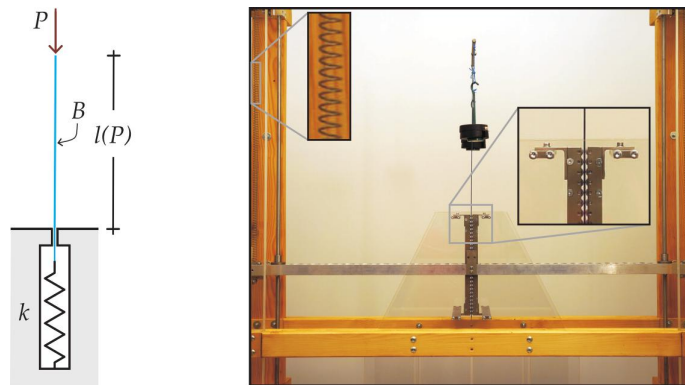
Figure 1.4: Structural scheme (left) and practical realization (right) of the structure
analyzed in Chapter 5. The penetrating blade is an elastic rod whose free
length l is a function of the applied axial load P. The blade has a free end
subject to the dead load P, while at the other edge the blade slides into a
frictionless sleeve and it is restrained by an axial linear spring of stiffness k.

including an increase of buckling load at decreasing of elastic stiffness, a finite
number of buckling loads for a system with infinite degrees of freedom (leading
to a non-standard Sturm-Liouville problem), more than one bifurcation
loads associated to each bifurcation mode, a restabilization of the straight
configuration after the second bifurcation load associated to the first instability
mode, postcritical paths and stability are deeply influenced by the presence
of an 'Eshelby-like force' and an asymptotic self-restabilization of the straight
configuration occurs for compliant systems with imperfection of tilt angle or
initial constant curvature.

Figure 1.5: Scales across millenia: a traditional balance (left) is based on the lever princi-
ple, while the innovative elastica arm scale (right) is based on deformation and
principles from configurational mechanics. In this particular configuration,
the deformable arm scale is working without counterweight.

A first innovative application of configurational mechanics to elastic systems, presented in Chapter 6, lies in the concept of the elastica arm scale, a result of nonlinear equilibrium kinematics of rods, so that deflection of the deformable arms becomes necessary for the equilibrium, which would be impossible for a rigid system. In this sense, the proposed concept (and prototype), which can work with or without counterweight, may be seen as an innovative advance with respect to the classical balances, see Fig. 1.5[3].
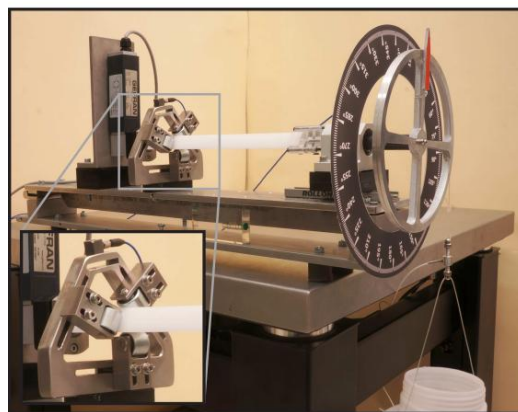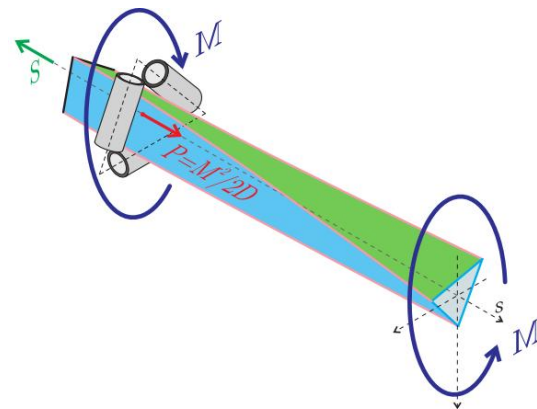
Figure 1.6: The design scheme (upper) and the torsional apparatus (lower) of the elastic system employed to disclose the 'Eshelby-like' propulsive force related to torsion. The elastic rod is subject to an applied torque M at one edge, while the other edge is inserted into a perfectly smooth and fitting female constraint, able to react to the applied moment.

Finally, Chapter 7 is devoted to the analysis of an elastic rod inserted into a frictionless and fitting socket head subject to a torque, realizing a uniform twisting moment, Fig. 1.6. It is theoretically proven and experimentally shown that, although perfectly smooth, the constraint generates an expulsive

[3]F. Bosi, D. Misseroni, F. Dal Corso and D. Bigoni. "An Elastica Arm Scale". In: *Proceedings of the Royal Society A* (2014), **470**, 20140232. *Cover paper.*
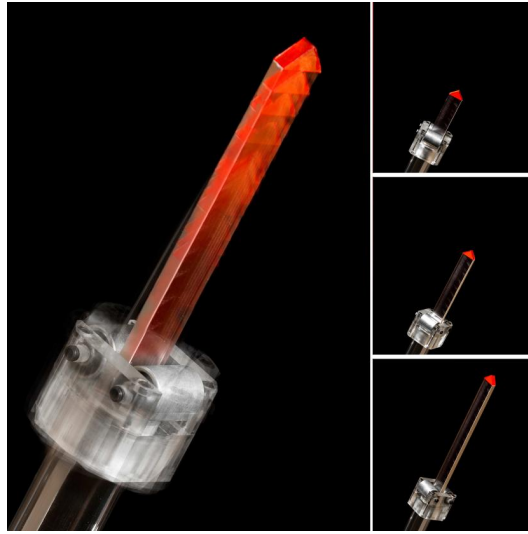
Figure 1.7: Left: a dynamic photo showing the torsional 'gun' in action; if the system is quickly twisted, the release mechanism of torsional elastic energy produces a propulsive force. Right: a sequence of three photos taken at 30 fps, showing that the propulsive force overcomes gravity.

axial force on the rod, which explains why screwdrivers at high torque have a tendency to disengage from screw heads. The smooth constraint can be viewed as a tight channel where locomotion, always linked with bending, is now generated from torsion. This new type of motion finds direct evidence in the realization of a configurational 'gun' or actuator, reported in Fig. 1.7, capable of transforming torque into propulsive force[4].

[4]D. Bigoni, F. Dal Corso, D. Misseroni and F. Bosi. "Torsional locomotion". In: *Proceedings of the Royal Society A* (2014), **470**, 20140599.

Chapter 2

The Euler elastica

> The determination of the equilibrium of an elastic *inextensible* rod subject to a large deflection is a problem of great interest, which is here addressed in its simplest form, namely, in a two-dimensional context. When a straight elastic rod is compressed, the determination of the critical load and of the postcritical behaviour provides a beautiful example of linear and nonlinear eigenvalue problem. The elastica theory will be employed throughout the present thesis in order to solve nonlinear equilibria of planar elastic rods.

The purpose of this section is to provide the Euler elastica theory with reference to an elastic rod subject to all possible boundary conditions because it will be useful in all the following chapters. We will follow and generalize Bigoni [13], classical references are Timoshenko and Gere [14], Love [15] and Reiss [16], while recent works have been presented by Wang [17], Vaz [18], Mikata [19], and O'Reilly and Peters [20, 21]. We will also address stability of equilibrium configurations, which has been treated by Maddocks [22], Manning et al. [23], Hoffman et al. [24], Manning [25, 26], Kuznetsov and Levyakov [27], Levyakov [28], Kuznetsov and Levyakov [29], Jin and Bao [30], Levyakov [31], Levyakov and Kuznetsov [32], and Sachkov and Levyakov [33].

2.1 The kinematics of an inextensible rod in a plane

We consider an inextensible rod of length l, rectilinear in a reference configuration and smoothly deformed, as shown in Fig. 2.1. In the (undeformed) deformed configuration, the generic point can be picked up using (a coordinate $x_0 \in [0, l]$) a curvilinear coordinate $s \in [0, l]$, so that inextensibility implies that $x_0 = s$ (so that $dx_0 = ds$).

The *displacement* $\mathbf{u}$ of the point $\mathbf{x}_0$ from the reference configuration is

$$\mathbf{u} = u_1(\mathbf{x}_0)\mathbf{e}_1 + u_2(\mathbf{x}_0)\mathbf{e}_2 = \mathbf{x} - \mathbf{x}_0, \tag{2.1}$$

which, introducing the (twice-continuously differentiable) deformation

$$\mathbf{x} = \mathbf{g}(\mathbf{x}_0), \tag{2.2}$$
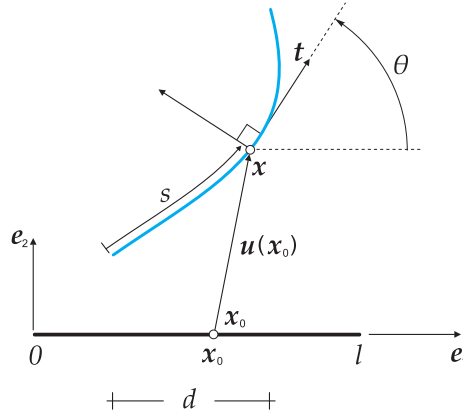
Figure 2.1: The kinematics of an elastic inextensible rod of length l, rectilinear in the reference configuration. Displacement of a point $\mathbf{x}_0$ of coordinate x_0 is $\mathbf{u}(x_0) = \mathbf{x} - \mathbf{x}_0$. Note that inextensibility implies that the curvilinear coordinate s is equal to the coordinate x_0, namely, $s = x_0$.

and noting that the point $\mathbf{x}_0$ has coordinate x_0 (so that $\mathbf{x}_0 = x_0\mathbf{e}_1$), becomes

$$\mathbf{u} = \mathbf{g}(x_0\mathbf{e}_1) - x_0\mathbf{e}_1. \tag{2.3}$$

Note that, since $\mathbf{e}_1$ is fixed, the dependence of function $\mathbf{g}$ on the unit vector could be omitted, so that equation (2.2) would become the parametric representation of the curve describing the elastica.

Let us consider now two neighbour points of the reference configuration at coordinates x_0 and $x_0 + \omega_0$, defining the vector $\mathbf{t}_0 = \omega_0\mathbf{e}_1$. This vector is mapped to

$$\mathbf{g}(\mathbf{x}_0 + \omega_0\mathbf{e}_1) - \mathbf{g}(\mathbf{x}_0), \tag{2.4}$$

so that, assuming ω_0 small and performing a Taylor series expansion of the deformation around $\omega_0 = 0$, yields the transformed vector (tangent to the deformed line at $\mathbf{x}_0$) as

$$\mathbf{F}(\omega_0\mathbf{e}_1) \tag{2.5}$$

where

$$\mathbf{F} = \frac{\partial \mathbf{g}}{\partial \mathbf{x}_0} = \left(u_1' + 1\right)\mathbf{e}_1 \otimes \mathbf{e}_1 + u_2'\mathbf{e}_2 \otimes \mathbf{e}_1 + \mathbf{e}_2 \otimes \mathbf{e}_2, \tag{2.6}$$

where the superscript $'$ denotes differentiation with respect to the coordinate $x_0 = s$ and the symbol '$\otimes$' denotes the dyadic product.

Since the elastica is assumed *inextensible*, the length of the transformed vector $\mathbf{F}(\omega_0\mathbf{e}_1)$ must maintain the same length of the initial vector $\mathbf{t}_0 = \omega_0\mathbf{e}_1$, therefore from equation (2.5) we obtain

$$|\mathbf{F}\mathbf{e}_1| = 1, \tag{2.7}$$

which, using equation (2.6) yields

$$u_1' + 1 = \sqrt{1 - (u_2')^2}. \tag{2.8}$$

Taking the derivative of equation (2.8) finally provides the inextensibility constraint in the form

$$u_1'' = -\frac{u_2' u_2''}{\sqrt{1 - (u_2')^2}}. \tag{2.9}$$

Since the inextensibility constraint is enforced and the tangent to the elastica at $\mathbf{x}$ is given by the unit vector $\mathbf{t}$

$$\mathbf{t} = \left(u_1' + 1\right)\mathbf{e}_1 + u_2'\mathbf{e}_2 = \sqrt{1 - (u_2')^2}\,\mathbf{e}_1 + u_2'\mathbf{e}_2, \tag{2.10}$$

the angle θ of inclination of the tangent $\mathbf{t}$ to the elastica at $\mathbf{x}$ is given by

$$\sin\theta = x_2' = u_2', \quad \cos\theta = x_1' = \sqrt{1 - (u_2')^2}, \tag{2.11}$$

and the length d of the projection of the elastica onto the $\mathbf{e}_1$ axis is

$$d = \int_0^l \cos\theta\,\mathrm{d}s = \int_0^l \sqrt{1 - (u_2')^2}\,\mathrm{d}. \tag{2.12}$$

The unit vector $\mathbf{n}$ normal to the elastica at $\mathbf{x}$ can be obtained through differentiation (with respect to s) of the scalar product $\mathbf{t}\cdot\mathbf{t}$, so that $\mathbf{t}'$ is found normal to $\mathbf{t}$ in the form

$$
\begin{aligned}
\mathbf{t}' &= -\frac{u_2' u_2''}{\sqrt{1 - (u_2')^2}}\mathbf{e}_1 + u_2''\mathbf{e}_2, \quad \text{or} \\
\mathbf{t}' &= -\theta'\sin\theta\mathbf{e}_1 + \theta'\cos\theta\mathbf{e}_2.
\end{aligned}
\tag{2.13}$$

The unit normal can therefore be obtained from equations $(2.13)_1$ or $(2.13)_2$, through division by the modulus (the so-called 'curvature'): [1]

$$|\mathbf{t}'| = \frac{|u_2''|}{\sqrt{1 - (u_2')^2}} = |\theta'|, \tag{2.15}$$

thus obtaining

$$
\begin{aligned}
\mathbf{n} &= \mathrm{sign}(u_2'')\left(-u_2'\mathbf{e}_1 + \sqrt{1 - (u_2')^2}\,\mathbf{e}_2\right) \quad \text{or,} \\
\mathbf{n} &= \mathrm{sign}(\theta')\left(-\sin\theta\mathbf{e}_1 + \cos\theta\mathbf{e}_2\right).
\end{aligned}
\tag{2.16}$$

---

[1] Note that the inverse of $\mathbf{F}$ is

$$\mathbf{F}^{-1} = \frac{1}{\sqrt{1 - (u_2')^2}}\mathbf{e}_1 \otimes \mathbf{e}_1 + \mathbf{e}_2 \otimes \mathbf{e}_2 - \frac{u_2'}{\sqrt{1 - (u_2')^2}}\mathbf{e}_2 \otimes \mathbf{e}_1. \tag{2.14}$$

The *signed curvature* χ is[2]

$$\chi = \frac{u_2''}{\sqrt{1-(u_2')^2}}, \quad \text{or} \quad \chi = \theta'. \qquad (2.21)$$

2.2 Total potential energy, constitutive equation and the elastica

The elastica is assumed to be loaded at its edges by forces generating a bending moment and a normal and a shearing force distribution along the deformed line.

The constitutive equation used for the elastica is the celebrated Jacob Bernoulli's assumption that the effects of normal and shearing forces are neglected and that the curvature of the deflection curve is linearly proportional to the bending moment as

$$\theta'(s) = \frac{M(s)}{B}, \qquad (2.22)$$

in which B is the bending stiffness (equal to the product between the Young modulus and the moment of inertia of the cross section area of the rod in the linear beam theory).

For the systems reported in Fig. 2.2 the total potential energy $\mathcal{V}(\theta(s))$ can be written as

$$\mathcal{V}(\theta(s)) = \int_0^l B \frac{(\theta'(s))^2}{2} \mathrm{d}s - P\left(l - \int_0^l \cos\theta(s)\mathrm{d}s\right) - R \int_0^l \sin\theta(s)\,\mathrm{d}s, \quad (2.23)$$

where the first term is the strain energy and R is a Lagrangian multiplier (representing –as will be shown below– the vertical reactions of the supports,

---

[2] If the deformed elastica is described in a Cartesian system in which its coordinates are

$$\tilde{x} = s + u_1(s) - u_1(0), \quad \tilde{y} = f(\tilde{x}), \qquad (2.17)$$

the signed curvature (2.21) can be obtained from the expression

$$\chi = \frac{\mathrm{d}^2 f/\mathrm{d}\tilde{x}^2}{[1+(\mathrm{d}f/\mathrm{d}\tilde{x})^2]^{3/2}}, \qquad (2.18)$$

by considering the identity

$$u_2(s) = f(s + u_1(s) - u_1(0)), \qquad (2.19)$$

from which the two following equations (keeping into account the inextensibility constraint) can be derived

$$\frac{\mathrm{d}f}{\mathrm{d}\tilde{x}} = \frac{u_2'}{\sqrt{1-(u_2')^2}}, \quad \frac{\mathrm{d}^2 f}{\mathrm{d}\tilde{x}^2} = \frac{u_2''}{[1-(u_2')^2]^2}, \qquad (2.20)$$

(where a prime denotes differentiation with respect to s), which have to be substituted into equation (2.18) to obtain equation (2.21).
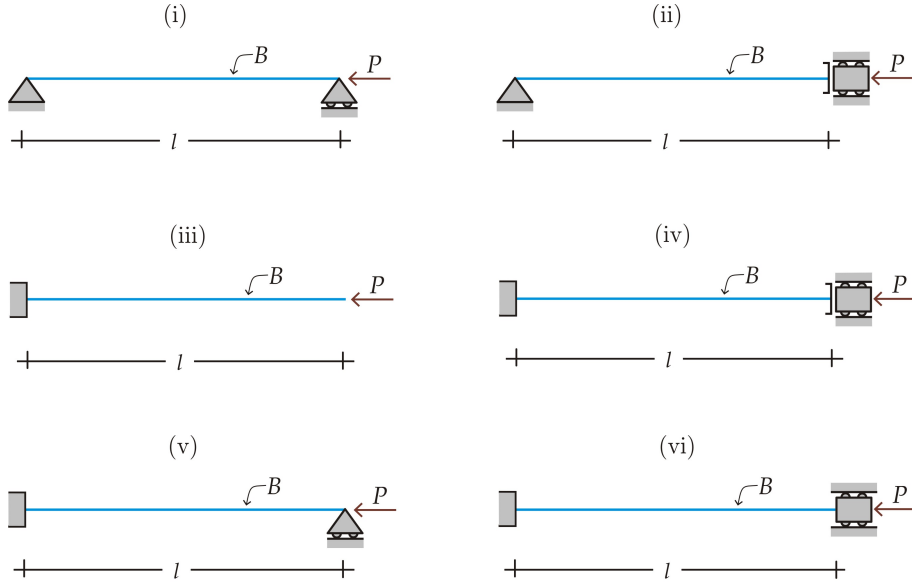
Figure 2.2: The considered elastic rods subjected to axial thrust (positive when compressive), with different constraints at their edges.

when present). Functional (2.23) is defined over the set of kinematically admissible deformed lines, meaning every twice-differentiable displacement field $\mathbf{u}$ corresponding to a rotation field θ and curvature θ' related via the constitutive equation (2.22) to the bending moment.

Considering a variation $\tilde{\theta}(s)$ of $\theta(s)$, satisfying the boundary conditions for each system

$$
\begin{aligned}
&\text{i)} \quad \theta'(0) = \theta'(l) = \tilde{\theta}'(0) = \tilde{\theta}'(l) = 0 \quad \text{and} \quad \int_0^l \sin\theta(s)\mathrm{d}s = 0 \\[2mm]
&\text{ii)} \quad \theta'(0) = \theta(l) = \tilde{\theta}'(0) = \tilde{\theta}(l) = 0 \\[2mm]
&\text{iii)} \quad \theta(0) = \theta'(l) = \tilde{\theta}(0) = \tilde{\theta}'(l) = 0 \\[2mm]
&\text{iv)} \quad \theta(0) = \theta(l) = \tilde{\theta}(0) = \tilde{\theta}(l) = 0 \\[2mm]
&\text{v)} \quad \theta(0) = \theta'(l) = \tilde{\theta}(0) = \tilde{\theta}'(l) = 0 \quad \text{and} \quad \int_0^l \sin\theta(s)\mathrm{d}s = 0 \\[2mm]
&\text{vi)} \quad \theta(0) = \theta(l) = \tilde{\theta}(0) = \tilde{\theta}(l) = 0 \quad \text{and} \quad \int_0^l \sin\theta(s)\mathrm{d}s = 0
\end{aligned}
\tag{2.24}
$$

we can evaluate the first variation $\delta\mathcal{V}$ of functional $\mathcal{V}$, which, keeping into

11

account integration by parts

$$\int_0^l \theta'(s)\tilde{\theta}'(s) = -\int_0^l \theta''(s)\tilde{\theta}(s)\,,$$

becomes

$$\delta\mathcal{V} = -\int_0^l \left[\theta''(s) + \frac{P}{B}\sin\theta(s) + \frac{R}{B}\cos\theta(s)\right]\tilde{\theta}(s)\,\mathrm{d}s, \qquad (2.25)$$

holding for all admissible perturbing fields $\tilde{\theta}(s)$.

Imposing the vanishing of the first variation (2.25) yields the 'differential equilibrium equation for the elastica'

$$\theta''(s) + \frac{P}{B}\sin\theta(s) + \frac{R}{B}\cos\theta(s) = 0, \qquad (2.26)$$

making transparent the fact that R represents the vertical reaction of the support, always null except in the following cases:

◇ for the structure (i) in the special situation (not be addressed for simplicity in the following) in which the two supports coincide;

◇ for the structure (v);

◇ for the structure (vi), when antisymmetric buckling modes are considered.

2.2.1 Simply supported elastica

Let us start considering the doubly pinned rod (i), so that, defining $\lambda^2 = P/B$, the equations governing the equilibrium of the elastica for a simply supported rod are

$\theta''(s) + \lambda^2\sin\theta(s) = 0, \quad s\in[0,l]$ governing diff. equation

$\theta'(0) = \theta'(l) = 0,$ b.c.: null moment at both supports

$u_1(0) = 0$ b.c.: null horiz. displ. at the left support

$u_2(0) = u_2(l) = 0,$ b.c.: null vert. displ. at both supports

$u_1'(s) = \cos\theta(s) - 1, \quad s\in[0,l]$ diff. equation for the horizontal displ.

$u_2'(s) = \sin\theta(s), \quad\quad\; s\in[0,l]$ diff. equation for the vertical displ.

$$(2.27)$$

Equations (2.27) define a *nonlinear eigenvalue problem*, for which the *trivial solution* $\theta = 0$ is always possible, so that the question arises whether nontrival solutions exist or not. Bifurcation corresponds to the situation in which the trivial solution (or possibly a bifurcated solution) of (2.27) splits into two or more, as λ passes through a critical value λ_{cr}, called 'bifurcation point'.

Before embarking in the solution of the problem (2.27), let us consider its linearization about the solution $\theta(s) = 0$, for which the horizontal displacement is null, $u_1(s) = 0$, so that the remaining equations are

$$\theta''(s) + \lambda^2\theta(s) = 0, \quad s \in [0, l] \quad \text{governing diff. equation}$$

$$\theta'(0) = \theta'(l) = 0, \qquad\qquad\qquad \text{boundary conditions}$$

$$u_2(0) = u_2(l) = 0, \qquad\qquad\qquad \text{boundary conditions}$$

$$u_2'(s) = \theta(s), \qquad\qquad s \in [0, l] \quad \text{diff. equation for the vertical displ.}$$
$$\tag{2.28}$$

Equations (2.28) define a *linear eigenvalue problem*, also called 'Sturm-Liouville problem' (Broman [34]). It admits the infinite solutions

$$\theta(s) = A_n \cos\frac{n\pi s}{l}, \quad n = 0, 1, 2, ... \tag{2.29}$$

and

$$\underbrace{u_2 = A_0 = 0, \quad n = 0,}_{\text{trivial solution}} \qquad \underbrace{u_2 = \frac{lA_n}{n\pi}\sin\frac{n\pi s}{l}, \quad n = 1, 2, ...}_{\text{bifurcation mode}} \tag{2.30}$$

where the trivial solution holds for every thrust P, while the nontrivial solutions hold if and only if

$$\lambda = \lambda_n = \frac{n\pi}{l}, \quad \Leftrightarrow \quad P = P_n^{cr} = \frac{n^2\pi^2 B}{l^2}, \quad n = 1, 2, ... \tag{2.31}$$

which defines the Euler's critical loads. As a consequence of the linearization, the amplitudes A_n ($n = 1, 2, ...$) of the bifurcation modes remain undetermined, nevertheless the critical loads correctly identify the bifurcation points on the trivial path, λ_n, as will be proven below.

Let us now solve the nonlinear problem (2.27). First of all, we note that if

$$\theta(s), \quad u_1(s), \quad u_2(s),$$

represent a solution corresponding to λ^2, the fields

$$\pm\theta(s) + 2n\pi, \quad u_1(s), \quad \pm u_2(s), \quad n = ..., -2, -1, 0, 1, 2, ...$$

also represent other solutions (symmetrical with respect to the x_1–axis) and the fields

$$\pm\theta(s) + (2n + 1)\pi, \quad -u_1(s) - 2s, \quad u_2(s), \quad n = ..., -2, -1, 0, 1, 2, ...$$

are valid for $-\lambda^2$. These solutions correspond to deformations symmetric with respect to the x_1 or the x_2–axis, which will be ignored without loss of generality. Therefore, defining without loss of generality $\hat\theta = \theta(\hat s)$, where $\hat s$ is curvilinear coordinate where the bending moment is null ($\hat s = 0$ for (ii), $\hat s = l$ for (iii), $\hat s = l/2$ for (iv)) so that for this particular case

$$\hat\theta = \theta(0), \tag{2.32}$$

we can only consider $0 \leq \hat\theta \leq \pi$.

A multiplication of equation $(2.27)_1$ by $\theta'(s)$ yields

$$\frac{\mathrm{d}}{\mathrm{d}s}\left[\frac{1}{2}(\theta'(s))^2 - \lambda^2\cos\theta(s)\right] = 0, \tag{2.33}$$

so that integration and consideration of equations $(2.27)_2$ and (2.32) leads to

$$\theta'(s) = \lambda\sqrt{2(\cos\theta(s) - \cos\hat\theta)}, \tag{2.34}$$

where we have selected the positive root, since the two solutions differ merely in sign.

An equation formally identical to equation (2.34) is usually obtained in the analysis of the oscillation of a simple pendulum (Temme [35]), so that it is a standard expedient to operate the following change of variables

$$\kappa = \sin\frac{\hat\theta}{2}, \quad \kappa\sin\phi(s) = \sin\frac{\theta(s)}{2}, \tag{2.35}$$

leading through trigonometric formulae to the differential problem

$$\frac{\mathrm{d}\phi(s)}{\mathrm{d}s} = \lambda\sqrt{1 - \kappa^2\sin^2\phi(s)}. \tag{2.36}$$

The boundary conditions imply that $\sin\phi(0) = 1$ and $\sin^2\phi(l) = 1$, so that

$$\phi(0) = \frac{4h + 1}{2}\pi, \quad \phi(l) = \frac{2j + 1}{2}\pi, \quad h, j = 0, \pm 1, \pm 2, ... \tag{2.37}$$

and therefore separating the variables and integrating equation (2.36) yields

$$s\lambda = \int_{\frac{4h+1}{2}\pi}^{\phi(s)} \frac{\mathrm{d}\phi}{\sqrt{1 - \kappa^2\sin^2\phi}}, \quad h = 0, \pm 1, \pm 2, ... \tag{2.38}$$

which, for $s = l$, becomes

$$l\lambda = \int_{\frac{4h+1}{2}\pi}^{\frac{2j+1}{2}\pi} \frac{\mathrm{d}\phi}{\sqrt{1 - \kappa^2 \sin^2 \phi}}, \quad h, j = 0, \pm 1, \pm 2, ... \tag{2.39}$$

Taken over one period, the integral (2.39) is equal to $2\mathcal{K}(\kappa)$, where

$$\mathcal{K}(\kappa) = \int_0^{\frac{\pi}{2}} \frac{\mathrm{d}\phi}{\sqrt{1 - \kappa^2 \sin^2 \phi}}, \tag{2.40}$$

is the complete elliptic integral of the first kind or the so-called 'real quarter period of the elliptic function' (Byrd and Friedman [36]; Temme [35]).

The integral in equation (2.39) can be rewritten as a function of an integer m as

$$l\lambda = 2m\mathcal{K}(\kappa), \quad \Leftrightarrow \quad P = \frac{B}{l^2} 4m^2 \left[\mathcal{K}\left(\sin \frac{\hat{\theta}}{2} \right) \right]^2, \tag{2.41}$$

an equation providing the relation between the applied load P and the rotation of the rod's edge on the left associated to the m–th bifurcation mode (and coincident with Reiss [16], his equation (3.16)).

For small $\hat{\theta}$, a Taylor series expansion of equation (2.41) provides exactly equation (2.31), thus proving that

> the critical Euler loads (2.31), calculated from the linearized theory, correctly determine the bifurcation points emanating from the trivial path.

Let us go back now to equation (2.38) and note that the integral on the right hand side can always be written as

$$\int_{\frac{4m+1}{2}\pi}^{\phi(s)} (\cdots) \, \mathrm{d}s = - \int_0^{\frac{4m+1}{2}\pi} (\cdots) \, \mathrm{d}s + \int_0^{\phi(s)} (\cdots) \, \mathrm{d}s, \tag{2.42}$$

so that, since (Byrd and Friedman [36])

$$\int_0^{\frac{4m+1}{2}\pi} \frac{\mathrm{d}\phi}{\sqrt{1 - \kappa^2 \sin^2 \phi}} = (4m + 1)\mathcal{K}(\kappa), \quad m = 0, \pm 1, \pm 2, ... \tag{2.43}$$

we obtain

$$s\lambda + (4m + 1)\mathcal{K}(\kappa) = \int_0^{\phi(s)} \frac{\mathrm{d}\phi}{\sqrt{1 - \kappa^2 \sin^2 \phi}}, \quad m = 0, \pm 1, \pm 2, ... \tag{2.44}$$

15

which provides

$$\phi(s) = \mathrm{am}\,(s\lambda + (4m+1)\mathcal{K}(\kappa), \kappa), \quad m = 0, \pm 1, \pm 2, ... \tag{2.45}$$

where 'am' denotes the Jacobi amplitude function of modulus κ. Employing the property (Byrd and Friedman [36])

$$\mathrm{am}\,(x \pm 2n\mathcal{K}(\kappa), \kappa) = \mathrm{am}\,(x, \kappa) \pm n\pi, \quad n = 0, \pm 1, \pm 2, ...$$

equation (2.45) can be simplified to

$$\phi(s) = \mathrm{am}\,(s\lambda + \mathcal{K}(\kappa), \kappa) + 2m\pi, \quad m = 0, \pm 1, \pm 2, ... \tag{2.46}$$

so that the definition of $\phi(s)$, equation $(2.35)_2$, yields

$$\sin\frac{\theta(s)}{2} = \kappa\,\mathrm{sn}\,(s\lambda + \mathcal{K}(\kappa), \kappa), \tag{2.47}$$

where 'sn' is the Jacobi sine amplitude function, defined as

$$\mathrm{sn}\,(x, \kappa) = \sin\,(\mathrm{am}\,(x, \kappa)).$$

A substitution of equation (2.47) into equation (2.34), where the identity $\cos\theta = 1 - 2\sin^2(\theta/2)$ is employed, yields

$$\theta'(s) = 2\lambda\kappa\,\mathrm{cn}\,(s\lambda + \mathcal{K}(\kappa), \kappa), \tag{2.48}$$

where 'cn' is the Jacobi cosine amplitude function, defined as

$$\mathrm{cn}\,(x, \kappa) = \cos\,(\mathrm{am}\,(x, \kappa)).$$

Note that, due to the properties

$$\mathrm{cn}\,(\mathcal{K}(\kappa), \kappa) = \mathrm{cn}\,(3\mathcal{K}(\kappa), \kappa) = \mathrm{cn}\,[(2m+1)\mathcal{K}(\kappa), \kappa] = 0, \quad m = 0, \pm 1, \pm 2, \pm 3$$

the boundary conditions $(2.27)_2$, namely $\theta'(0) = \theta'(l) = 0$, are satisfied[3].

According to equations (2.3) and $(2.27)_{(5,6)}$, the differential equations determining the points $\mathbf{x}$ of the deformed elastica are

$$x_1'(s) = \cos\theta(s), \quad x_2'(s) = \sin\theta(s), \tag{2.49}$$

which, since $\cos\theta = 1 - 2\sin^2(\theta/2)$ and $\sin\theta = 2\sin(\theta/2)\sqrt{1 - \sin^2(\theta/2)}$ and using equation (2.47), provide the two differential equations

$$\begin{aligned} x_1'(s) &= 1 - 2\kappa^2\,\mathrm{sn}^2(s\lambda + \mathcal{K}(\kappa), \kappa), \\[2mm] x_2'(s) &= 2\kappa\,\mathrm{sn}\,(s\lambda + \mathcal{K}(\kappa), \kappa)\mathrm{dn}\,(s\lambda + \mathcal{K}(\kappa), \kappa), \end{aligned} \tag{2.50}$$

---

[3] equation (2.41) has been used in the boundary condition at $\theta'(l)$.

where 'dn' is the Jacobi elliptic function, defined as

$$\mathrm{dn}\,(s\lambda + \mathcal{K}(\kappa), \kappa) = \sqrt{1 - \kappa^2\,\mathrm{sn}^2(s\lambda + \mathcal{K}(\kappa), \kappa)}. \qquad (2.51)$$

Since the following differentiation rules are known (Byrd and Friedman [36])

$$\frac{\partial}{\partial x} E(x, \kappa) = \sqrt{1 - \kappa^2 \sin^2 x},$$

$$\frac{\partial}{\partial x} \mathrm{am}\,(x, \kappa) = \mathrm{dn}\,(x, \kappa), \qquad (2.52)$$

$$\frac{\partial}{\partial x} \mathrm{cn}\,(x, \kappa) = -\,\mathrm{sn}\,(x, \kappa)\,\mathrm{dn}\,(x, \kappa),$$

where $E(x, \kappa)$ is the incomplete elliptic integral of the second kind of modulus κ, defined as

$$E(x, \kappa) = \int\limits_0^x \sqrt{1 - \kappa \sin^2 t}\,\mathrm{d}t,$$

taking into account the boundary conditions $(2.27)_{3,4}$, we integrate equations (2.50), thus arriving at the equations describing the shape of the elastica [4]

$$x_1(s) \;\; = -s + \frac{2}{\lambda} \left\{ E\left[\mathrm{am}\,(s\lambda + \mathcal{K}(\kappa), \kappa), \kappa\right] - E\left[\mathrm{am}\,(\mathcal{K}(\kappa), \kappa), \kappa\right] \right\},$$

$$x_2(s) \;\; = -\frac{2\kappa}{\lambda} \mathrm{cn}(s\lambda + \mathcal{K}(\kappa)),$$

$$(2.53)$$

which are identical with those provided by Love [15] (his equations (12) at n. 263).

The displacement of the point of application of the force P is negative (for $P > 0$) and its absolute value can be immediately obtained from equations $(2.53)_1$, since $|u_1(l)| = l - x_1(l)$, in the form

$$|u_1(l)| = 2l - \frac{2}{\lambda} \left\{ E\left[\mathrm{am}\,(l\lambda + \mathcal{K}(\kappa), \kappa), \kappa\right] - E\left[\mathrm{am}\,(\mathcal{K}(\kappa), \kappa), \kappa\right] \right\}, \quad (2.54)$$

so that using now equation (2.41) we obtain

$$\frac{|u_1(l)|}{l} = 2 - \frac{E\left[\mathrm{am}\,((2m+1)\mathcal{K}(\kappa), \kappa), \kappa\right] - E\left[\mathrm{am}\,(\mathcal{K}(\kappa), \kappa), \kappa\right]}{m\mathcal{K}(\kappa)}, \quad m = 1, 2, \dots$$

$$(2.55)$$

---

[4]These relations are valid also for the hinged-clamped case (ii), where the value of λ as a function of the angle of $\hat{\theta}$ is obtained through the relation $l\lambda = (2m - 1)\mathcal{K}(\sin\frac{\hat{\theta}}{2})$

which eventually can be simplified to (an equation given by Reiss [16], his equation (3.20))[5]

$$\frac{|u_1(l)|}{l} = 2 - \frac{2\,E\,(\kappa)}{\mathcal{K}(\kappa)}, \tag{2.56}$$

where $E(\pi/2, \kappa) = E(\kappa)$ represents the complete elliptic integral of the second kind. Note that (2.56) is independent of the bifurcation mode m, so that the displacement of the right pin of the rod depends only on $\hat{\theta}$ (through κ).

The mid-span deflection of the rod is null for even values of the mode m, while for odd m can be evaluated as

$$\frac{|u_2(l/2)|}{l} = \frac{\kappa}{m\,\mathcal{K}(\kappa)}, \quad m = 1, 3, 5, \dots \tag{2.57}$$

In summary, for a given $\hat{\theta}$ and a given mode m we can calculate the corresponding λ (using equation (2.41)) and $u_1(l)$ (using equation (2.56)) and plot the elastica (using equations (2.53)). The bifurcation diagram showing the load P (normalized through division by $\pi^2 B$ and multiplication by l^2) as a function of the displacement of the right pin of the rod (normalized through division by l) is shown in Fig. 2.3. In the figure the first three critical loads and the corresponding three branches are reported. We may note that the branches do not cross each other and the load is continuously increasing during the post-critical behaviour.

The deformed elastic lines have been evaluated and plotted in Fig. 2.4 for the first two branches at fixed values of $\hat{\theta}$, namely, $\{10°, 45°, 90°, 135°, 160°\}$. These values of rotation correspond to rod end displacements, respectively equal to $\{0.008, 0.149, 0.543, 1.049, 1.340\}\,l$. Note that in Fig. 2.4 also the undeformed configuration, $\hat{\theta} = 0°$, is reported in order to provide the scale of the displacement.

It should be noticed that the line of thrust (joining the two forces in Fig. 2.4) intersects the elastica at points of inflexion ($\theta' = 0$), separating (using the Love's nomenclature) different 'bays'.

2.2.2 In-plane secondary bifurcations of the simply-supported elastica

Let us go back to Fig. 2.3 and note that on each bifurcated branch there is a secondary bifurcation point (marked with a circle), which occurs when the two supports of the rod coincide, namely, when $u_1(l) = -l$, corresponding to $\hat{\theta} = 130.7099°$ and different load values: $Pl^2/(\pi B) = 2.1833$ for the first

---

[5] The following identities turn out to be useful (Byrd and Friedman [36])

$$\mathrm{am}\,[\mathcal{K}(\kappa), \kappa] = \pi/2, \quad \mathrm{am}[(2m+1)\mathcal{K}(\kappa), \kappa] = (2m+1)\pi/2, \quad E(n\pi/2, \kappa) = n\,E(\kappa).$$
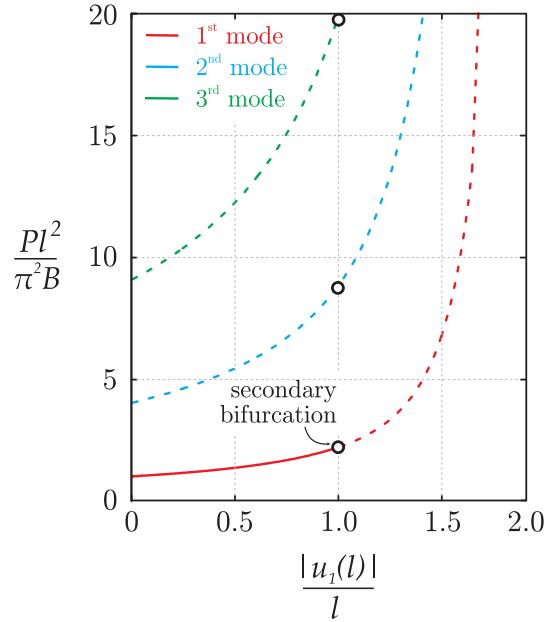
Figure 2.3: Dimensionless load $Pl^2/(\pi^2 B)$ of a doubly supported rod versus dimensionless displacement $u_1(l)/l$. The first three principal bifurcation points and branches are reported together with the first three secondary bifurcation points. All equilibrium configurations on the second and third branch are unstable (dashed curves). The first branch becomes unstable after the secondary bifurcation points.
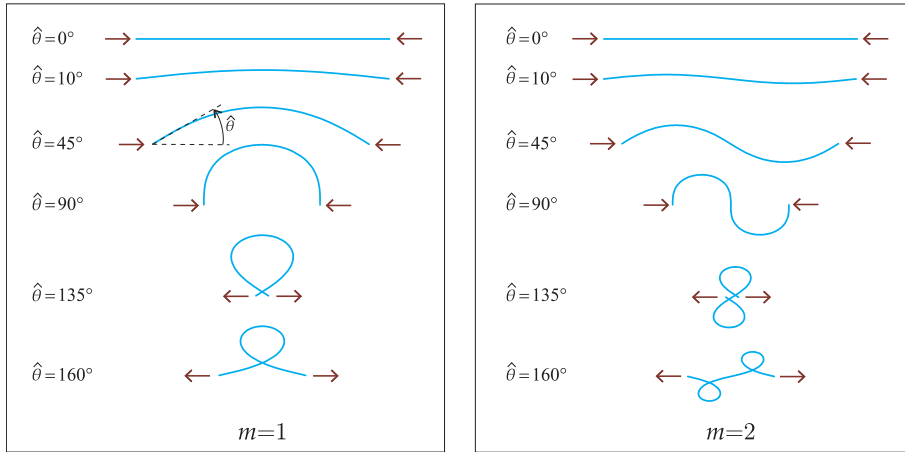
Figure 2.4: Deformed elastic lines for the first two modes $m = 1, 2$ at different values of parameters setting the deformation: the initial inflexion angle $\hat{\theta} = \{0, 10°, 45°, 90°, 135°, 160°\}$ and corresponding dimensionless displacement of the end of the rod $u_1(l)/l = \{0, 0.008, 0.149, 0.543, 1.049, 1.340\}$. The deformed shapes of the elastica represent the post-critical behaviour of the structure.

19
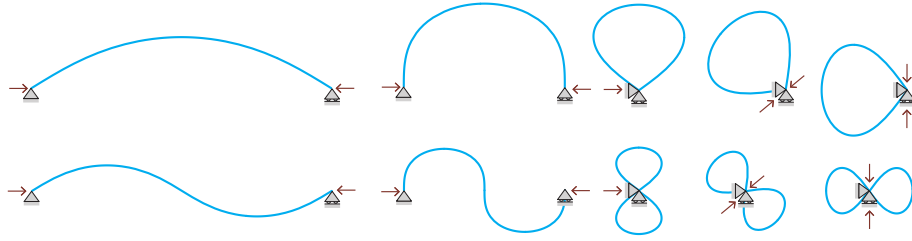
Figure 2.5: Sketch of the in-plane secondary bifurcation modes of the elastica, referred to the first (upper part) and second (lower part) mode. When the two supports coincide the structure can suffer a rigid-body rotation. During this rotation, the horizontal load drops to zero (value reached when the elastica is rotated at 90°), so that the force is maintained by the vertical reaction of the support. For rotation angles greater than 90° (not reported) the force changes sign. For imposed horizontal load, the structure becomes unstable when the two supports coincide and snaps to the configuration $u_1 = -2l$, where it is in equilibrium with a tensile load.

mode, $Pl^2/(\pi B) = 8.7335$ for the second mode, $Pl^2/(\pi B) = 19.6504$ for the third mode, and so on.

These secondary bifurcation modes, passed unnoticed until Maddocks [22] (see also Kuznetsov and Levyakov [29]; Sachkov and Levyakov [33]), have a simple explanation. In fact, *when the two supports of the rod momentarily coincide during deformation along the bifurcation path, the structure can rigidly rotate about the pin*. During the rigid-body rotation, vertical reactions of the supports are generated, so that the horizontal load drops until, when the structure is rotated at 90°, the horizontal load is reduced to zero and, finally, further rotation requires a negative force. The situation is sketched in Fig. 2.5, with reference to the first two modes. For imposed horizontal load, the situation in which the two supports coincide marks an instability point, in the sense that: (i.) at this point the structure rigidly rotates and snaps to the configuration $u_1 = -2l$, where it is subject to a tensile load; (ii.) equilibrium configurations belonging to the post-critical path $m = 1$ and $\hat{\theta} > 130.7099°$ are unstable, as shown in Fig. 2.12.

2.2.3 Doubly clamped elastica

The equations governing the equilibrium of the elastica for a doubly clamped rod are

$$\theta''(s) + \frac{P}{B}\sin\theta(s) + \frac{R}{B}\cos\theta(s) = 0, \quad s \in [0,l] \quad \text{governing diff. equation}$$

$$\theta(0) = \theta(l) = 0, \qquad\qquad\qquad\qquad \text{b.c.: null rotation}$$

$$u_1(0) = 0 \qquad\qquad\qquad\qquad\qquad \text{b.c.: null horizontal displ.}$$

$$u_2(0) = u_2(l) = 0, \qquad\qquad\qquad\qquad \text{b.c.: null vertical displ.}$$

$$u_1'(s) = \cos\theta(s) - 1, \qquad\qquad s \in [0,l] \quad \text{diff. eq. for horiz. displ.}$$

$$u_2'(s) = \sin\theta(s), \qquad\qquad\qquad s \in [0,l] \quad \text{diff. eq. for vert. displ.}$$

$$(2.58)$$

As the simply supported elastica, also equations (2.58) define a *nonlinear eigenvalue problem*, for which the *trivial solution* $\theta(s) = 0$ is always possible, so that we are looking for non-trivial solutions. Considering for this particular system symmetric deformed configurations with $2m$ inflection points, vertical equilibium imposes $R = 0$, so that the differential equation turns out to be the same as in the previous doubly supported problem. For antisymmetric configurations with $2m + 1$ inflection points a non null vertical reaction R is generated.

Linearisation of the problem (2.58) about the solution $\theta(0) = 0$ leads to

$$\theta''(s) + \frac{P}{B}\theta(s) = -\frac{R}{B}, \qquad\qquad s \in [0,l] \quad \text{governing diff. equation}$$

$$\theta(0) = \theta(l) = 0, \quad \int_0^l \theta(s)\mathrm{d}s = 0, \qquad\qquad \text{boundary conditions}$$

$$(2.59)$$

Equations (2.59) define *linear eigenvalue problem* that admits the trivial solution $\theta(s) = 0$ for every thrust P, whereas the infinite non trivial solutions are only possible when the following equation is satisfied

$$2\left(1 - \cos\sqrt{\frac{Pl^2}{B}}\right) = \frac{Pl^2}{B}\sin\sqrt{\frac{Pl^2}{B}}, \qquad\qquad (2.60)$$

defining the Euler's bifurcation loads for the doubly clamped rod as

$$P_1^{cr} = \frac{4\pi^2 B}{l^2}, \quad P_2^{cr} = \frac{8.9868^2 B}{l^2}, \quad P_3^{cr} = \frac{16\pi^2 B}{l^2}, \quad P_4^{cr} = \frac{15.4505^2 B}{l^2}, \ldots$$

$$(2.61)$$

where the odd (even) bifurcation loads determine the symmetric (antisymmetric) bifurcation paths.
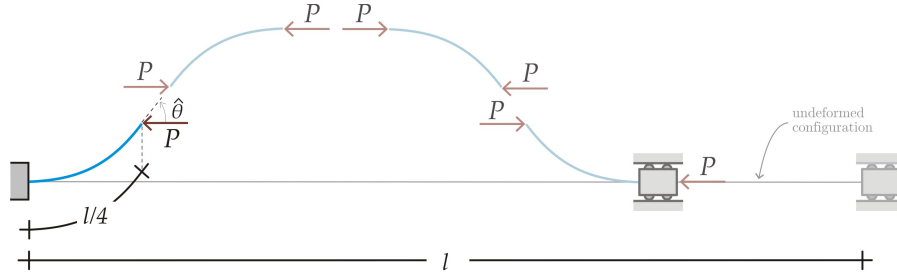
Figure 2.6: Deformed (and undeformed) configuration for the first (symmetric) mode of the doubly clamped rod. Note that, thanks to symmetry, the problem is reduced to the analysis of a cantilever rod of length $l/4$ loaded with an end thrust P.

Symmetric buckling modes

With reference to the symmetric buckling modes with $2m$ inflection points ($R = 0$), the rotation field $\theta(s)$ is a solution of the following differential problem

$$\theta''(s) + \lambda^2 \sin \theta(s) = 0, \quad s \in [0, l]$$

$$\theta(0) = \theta(l) = 0,$$

(2.62)

so that, a multiplication of equation $(2.62)_1$ by $\theta'(s)$ and its integration leads to

$$\theta'(s) = \pm\lambda\sqrt{2(\cos\theta(s) - \cos\hat{\theta})}, \tag{2.63}$$

where, in this case, $\hat{\theta}$ represents the angle of rotation at the inflection point $s = l/4$.

In order to facilitate the analytical description, the symmetry properties can be exploited, so that four simply clamped rods, of equal length $l/4$, can be identified, see Fig. 2.6.

Therefore, limiting the attention only to one quarter of the rod and selecting the positive root (representing the curvature) of equation (2.63) for $s \in [0, l/4]$, the change of variables (2.35) leads to the differential problem

$$\frac{\mathrm{d}\phi(s)}{\mathrm{d}s} = \lambda\sqrt{1 - \kappa^2 \sin^2 \phi}. \tag{2.64}$$

The boundary conditions for the considered problem imply that $\sin\phi(0) = 0$ and $\sin\phi(l/4) = 1$, so that

$$\phi(0) = h\pi, \quad \phi(l/4) = \frac{2j+1}{2}\pi, \quad h, j = 0, \pm 1, \pm 2, ... \tag{2.65}$$

and therefore separating the variables and integrating equation (2.64) yields

$$s\lambda = \int_{h\pi}^{\phi(s)} \frac{\mathrm{d}\phi}{\sqrt{1 - k^2 \sin^2\phi}}, \quad h = 0, \pm1, \pm2, ... \tag{2.66}$$

which, for $s = l/4$, becomes

$$\frac{l}{4}\lambda = \int_{h\pi}^{\frac{2j+1}{2}\pi} \frac{\mathrm{d}\phi}{\sqrt{1 - k^2 \sin^2\phi}}, \quad h, j = 0, \pm1, \pm2, ... \tag{2.67}$$

and can be rewritten as a function of an odd integer m as

$$l\lambda = 2(m+1)\mathcal{K}(\kappa), \quad \Leftrightarrow \quad P = \frac{B}{l^2} 4(m+1)^2 \left[\mathcal{K}\left(\sin\frac{\hat{\theta}}{2}\right)\right]^2, \quad m = 1, 3, 5, ... \tag{2.68}$$

This equation provides the relation between the applied load P and the rotation $\hat{\theta}$ of the first inflection point ($s = l/4$) associated with the odd (symmetric) m–th buckling mode.

For small $\hat{\theta}$, a Taylor series expansion of equation (2.68) provides exactly the odd critical Euler loads calculated from the linearized theory in equation (2.61).

Going back to to equation (2.66) and employing the definition of $\phi(s)$, equation (2.35), in addition to the odd nature of Jacobi amplitude function, namely,

$$\mathrm{am}\,(x, \kappa) = -\mathrm{am}\,(-x, \kappa),$$

we can write the rotation field for the entire rod as [6]

$$\theta(s) = 2\arcsin\left(\kappa\,\mathrm{sn}\,(s\lambda, \kappa)\right) \qquad s \in [0, l]. \tag{2.69}$$

According to equations (2.11) and (2.69) and taking into account the boundary conditions (2.24)$_6$, the analytical formulae describing the shape of the elastica for the entire rod, $s \in [0, l]$ can be written as [7]

$$\begin{aligned} x_1(s) &= -s + \frac{2}{\lambda}\left\{E\left[\mathrm{am}\,(s\lambda, \kappa), \kappa\right]\right\}, \\ x_2(s) &= \frac{2\kappa}{\lambda}\left[1 - \mathrm{cn}(s\lambda)\right]. \end{aligned} \tag{2.70}$$

---

[6]We may note that the equations describing the rotational field, equation (2.69), and the shape of the elastica, equation (2.70), remain the same also for structure (iii). The only difference lies in the relation between the load P and the angle of the free edge $\hat{\theta} = \theta(l)$, associated to the mth bifurcation mode, which is $l\lambda = (2m - 1)\mathcal{K}(\sin\frac{\hat{\theta}}{2})$.

[7]equation (2.70) describes also the deformed configuration of system (iv), together with the relation (2.41), providing a connection between the thrust P and the angle $\hat{\theta} = \theta(l/2)$ for different m buckling modes.

The displacement of the point of application of the force can be immediately obtained from equations $(2.70)_1$, since $|u_1(l)| = l - x_1(l)$, in the form

$$\frac{|u_1(l)|}{l} = -2\left(\frac{E(\kappa)}{\mathcal{K}(\kappa)} - 1\right), \tag{2.71}$$

which is independent of the bifurcation mode m, so that the displacement of the right edge of the rod depends only on $\hat{\theta}$ (through κ). The bifurcation diagram showing the load P (normalized through division by $\pi^2 B$ and multiplication by l^2) as a function of the displacement of the right movable edge of the rod (normalized through division by l) is shown in Fig. 2.8 together with the bifurcation diagram valid for antisymmetric buckling modes. In the figure the first three critical loads and the corresponding three branches (two symmetric and one antisymmetric) are reported. The deformed elastic lines have been evaluated and plotted in Fig. 2.9 for the first symmetric branch (first buckling mode) at fixed values of $|u_1(l)|/l$, namely, $\{0, 0.2, 0.6, 1.0, 1.4\}$, together with the first anti-symmetric branch (second buckling mode), described by equations (2.86), (2.89), and (2.95). Note that in Fig. 2.9 also the undeformed configuration, $P = 0$, is reported, providing the scale bar for displacements.

Antisymmetric buckling modes

Let us go back now to equation (2.58) and solve the non linear differential equation in the case of antisymmetric (even) buckling modes with $2m + 1$ inflection points ($R \neq 0$). Antisymmetry properties allow us to conclude that one inflection point is located at $s = l/2$, so that we may observe that the structure can be regarded as formed with two equal clamped-hinged rods subject to end thrust, Fig. 2.7. Therefore, we can consider only one half of the rod represented by the following differential problem [8]

$$\theta''(s) + \frac{P}{B}\sin\theta(s) + \frac{R}{B}\cos\theta(s) = 0, \quad s \in \left[0, \frac{l}{2}\right]$$

$$\theta(0) = \theta'\left(\frac{l}{2}\right) = 0, \tag{2.72}$$

$$\int_0^{l/2} \sin\theta(s)\mathrm{d}s = 0.$$

Defining $\gamma^2 = \sqrt{P^2 + R^2}/B$ and the angle $\psi(s) = \theta(s) + \beta$, where β is the angle defining the inclination of the resultant of P and R with respect to the

---

[8]We can note that equilibrium equations for the structure (v) are exactly the same of the antisymmetric configuration of the structure (vi).
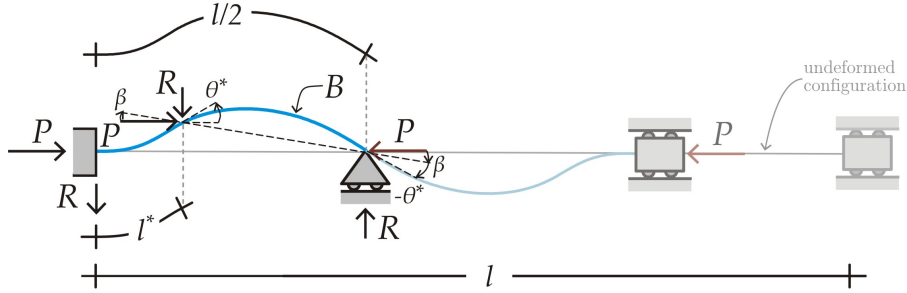
Figure 2.7: Deformed configuration for the second (antisymmetric) mode for the doubly clamped rod. Note that, thanks to antisymmetry, one inflection point is located at the mid-span, so that the problem is reduced to a clamped-guided rod of length $l/2$.

horizontal direction, so that

$$\cos \beta = \frac{F}{\sqrt{P^2 + R^2}}, \qquad \sin \beta = \frac{R}{\sqrt{P^2 + R^2}}, \tag{2.73}$$

the differential problem (2.72) can be rewritten as

$$\psi''(s) + \gamma^2 \sin \psi(s) = 0, \qquad s \in \left[0, \frac{l}{2}\right],$$

$$\psi(0) = \beta,$$

$$\psi'\left(\frac{l}{2}\right) = 0, \tag{2.74}$$

$$\int_0^{l/2} \sin\left(\psi(s) - \beta\right) \mathrm{d}s = 0.$$

Before proceeding with the non-trivial solutions of the differential problem (2.74), let us define $\theta(l/2) = -\theta^*$, so that $\psi(l/2) = -\psi^* = -\theta^* + \beta$ and an inflection point exists in the buckled rod, located at $s = l^*$, where the angle of rotation is $\theta(l^*) = \theta^*$ and $\theta'(l^*) = 0$ ($\psi(l^*) = \psi^*$ and $\psi'(l^*) = 0$), as reported in Fig. 2.7. Multiplication of equation $(2.74)_1$ by $\psi'(s)$ and integration in the variable s yields

$$\frac{\mathrm{d}}{\mathrm{d}s}\left[\frac{1}{2}(\psi'(s))^2 - \gamma^2 \cos \psi(s)\right] = 0, \tag{2.75}$$

so that consideration of boundary conditions at the inflection point $s = l^*$ leads to

$$\psi'(s) = \pm \lambda \sqrt{2(\cos \psi(s) - \cos \psi^*)}, \tag{2.76}$$

where the $+$ $(-)$ sign means a positive (negative) curvature. From equation (2.76) and considering Fig. 2.7, the following conditions can be derived

$$\psi^{'}(s) = +\lambda\sqrt{2\left(\cos\psi(s) - \cos\psi^*\right)}, \qquad s \in (0, l^*),$$

$$\psi^{'}(s) = -\lambda\sqrt{2\left(\cos\psi(s) - \cos\psi^*\right)}, \qquad s \in \left(l^*, \frac{l}{2}\right). \tag{2.77}$$

It is a standard expedient to operate the following change of variables

$$\eta = \sin\frac{\psi^*}{2}, \qquad \eta\sin\omega(s) = \sin\frac{\psi(s)}{2}, \tag{2.78}$$

leading to the following differential equation

$$\frac{\mathrm{d}\,\omega(s)}{\mathrm{d}s} = \pm\gamma\sqrt{1 - \eta^2\sin^2\omega(s)}. \tag{2.79}$$

The boundary conditions imply that

$$\omega(0) = \omega_\beta, \quad \omega(l^*) = \frac{\pi}{2} \quad \omega\left(\frac{l}{2}\right) = -\frac{\pi}{2}, \tag{2.80}$$

where $\omega_\beta = \arcsin\left(\dfrac{1}{\eta}\sin\left(\dfrac{\beta}{2}\right)\right)$.

Therefore, separation of variable and integration of the positive root of equation (2.79) between 0 and l^* yields

$$\int\limits_0^{l^*}\gamma\mathrm{d}s = \int\limits_{\omega_\beta}^{\frac{\pi}{2}}\frac{\mathrm{d}\omega}{\sqrt{1 - \eta^2\sin^2\omega}}, \tag{2.81}$$

which expresses the non-trivial solution for l^*, related to η, γ and β, as

$$l^*\gamma = \mathcal{K}(\eta) - \mathcal{K}\left(\omega_\beta, \eta\right), \tag{2.82}$$

where

$$\mathcal{K}(x, \eta) = \int\limits_0^x\frac{\mathrm{d}\omega}{\sqrt{1 - \eta^2\sin^2\omega}}, \tag{2.83}$$

is the incomplete elliptic integral of the first kind. Now, let us integrate the negative root of equation (2.79) between l^* and $l/2$ and recall Riemann theorem and the property of integral of even functions

$$-\int\limits_{\frac{\pi}{2}}^{-\frac{\pi}{2}}\frac{\mathrm{d}\omega}{\sqrt{1 - \eta^2\sin^2\omega}} = 2\int\limits_0^{\frac{\pi}{2}}\frac{\mathrm{d}\omega}{\sqrt{1 - \eta^2\sin^2\omega}} \tag{2.84}$$

to obtain

$$\gamma \left(\frac{l}{2} - l^* \right) = 2\mathcal{K}(\eta), \qquad (2.85)$$

so that, considering the periodicity of boundary conditions (2.80) and using equations (2.82) and (2.85), we arrive at

$$\gamma l = 2\left[(m+1)\mathcal{K}(\eta) - \mathcal{K}\left(\omega_\beta, \eta\right)\right] \qquad m = 2, 4, 6, ... \qquad (2.86)$$

Note that equation (2.86) provides the relation between the load P and the angles θ^* (through η and ψ^*) and β associated with the even (antisymmetric) m–th buckling mode. The above equation is one of the two equations to be solved in our problem. The other relation that allows the resolution of the problem can be obtained from condition $(2.72)_3$, which can be rewritten as

$$\int_0^{l^*} \sin\left(\psi(s) - \beta\right) \mathrm{d}s + \int_{l^*}^{\frac{l}{2}} \sin\left(\psi(s) - \beta\right) \mathrm{d}s = 0 \qquad (2.87)$$

and considering equation (2.78) and trigonometric angle difference identity, as

$$\int_\beta^{\psi^*} \frac{\sin\psi\cos\beta}{\gamma\sqrt{2(\cos\psi - \cos\psi^*)}}\mathrm{d}\psi - \int_\beta^{\psi^*} \frac{\sin\beta\cos\psi}{\gamma\sqrt{2(\cos\psi - \cos\psi^*)}}\mathrm{d}\psi$$
$$- \int_{\psi^*}^{-\psi^*} \frac{\sin\psi\cos\beta}{\gamma\sqrt{2(\cos\psi - \cos\psi^*)}}\mathrm{d}\psi + \int_{\psi^*}^{-\psi^*} \frac{\sin\beta\cos\psi}{\gamma\sqrt{2(\cos\psi - \cos\psi^*)}}\mathrm{d}\psi = 0. \qquad (2.88)$$

The third integral of equation (2.88) is null because the integrand is an odd function, while the other terms, since the following relations are considered

$$\cos\psi = 1 - 2\sin^2(\psi/2), \qquad \sin\psi = 2\sin(\psi/2)\sqrt{1 - \sin^2(\psi/2)},$$

can be rewritten, using equation (2.78), in the final form (Mikata [19])

$$-2\eta\cos\omega_\beta\left(1 - 2\eta^2\sin^2\omega_\beta\right) + 2\eta\sin\omega_\beta\sqrt{1 - \eta^2\sin^2\omega_\beta}\Big\{(m+1)\big[2E(\eta)$$
$$-\mathcal{K}(\eta)\big] - [2E(\omega_\beta, \eta) - \mathcal{K}(\omega_\beta, \eta)]\Big\} = 0, \qquad m = 2, 4, 6, ... \qquad (2.89)$$

Equations (2.86) and (2.89) are highly non-linear and represent the non-trivial solution. The relation between β and θ^* (the former contained in ω_β and the latter in η) can be numerically obtained from equation (2.89) and used into equation (2.86) to obtain the relation $P - \theta^*$.

Our aim now is to calculate the transverse and axial components of the deflected rod. To this purpose, if we integrate equation (2.79) from $s = 0$ up to a generic point before the inflection point $s = l^*$

$$\int\limits_0^s \gamma \mathrm{d}s = \int\limits_{\omega_\beta}^{\omega(s)} \frac{\mathrm{d}\omega}{\sqrt{1 - \eta^2 \sin^2 \omega}}, \qquad (2.90)$$

we would arrive, considering decomposition (2.42) and equation (2.78)$_2$, at

$$\sin\left(\frac{\omega}{2}\right) = \eta \operatorname{sn}\left[\gamma s + \mathcal{K}(\omega_\beta, \eta), \eta\right], \qquad (2.91)$$

where this relation is valid for the entire rod once the following properties of elliptic integral (Byrd and Friedman [36]) are considered

$$\operatorname{sn}(-x + 2\mathcal{K}(\eta), \eta) = -\operatorname{sn}(-x, \eta) = \operatorname{sn}(x, \eta). \qquad (2.92)$$

Finally, from integration of the kinematic fields (2.11), the analytical form for the transverse and axial displacements can be obtained, valid for the entire rod $s \in (0, l)$, as [9]

$$
\begin{aligned}
x_1(s) = {}& +\sin\beta\left[-\frac{2\eta}{\gamma}\operatorname{cn}\big(\gamma s + \mathcal{K}(\omega_\beta, \eta), \eta\big) + \frac{2\eta}{\gamma}\operatorname{cn}\big(\mathcal{K}(\omega_\beta, \eta), \eta\big)\right] \\
& \cos\beta\left\{-s + \frac{2}{\gamma}\left[E\left[\operatorname{am}\left(\gamma s + \mathcal{K}(\omega_\beta, \eta), \eta\right), \eta\right]\right.\right. \\
& \left.\left. - E\left[\operatorname{am}\left(\mathcal{K}(\omega_\beta, \eta), \eta\right), \eta\right]\right]\right\}, \\[4pt]
x_2(s) = {}& \cos\beta\left[-\frac{2\eta}{\gamma}\operatorname{cn}\big(\gamma s + \mathcal{K}(\omega_\beta, \eta), \eta\big) + \frac{2\eta}{\gamma}\operatorname{cn}\big(\mathcal{K}(\omega_\beta, \eta), \eta\big)\right] \\
& -\sin\beta\left\{-s + \frac{2}{\gamma}\left[E\left[\operatorname{am}\left(\gamma s + \mathcal{K}(\omega_\beta, \eta), \eta\right), \eta\right]\right.\right. \\
& \left.\left. - E\left[\operatorname{am}\left(\mathcal{K}(\omega_\beta, \eta), \eta\right), \eta\right]\right]\right\}.
\end{aligned}
\qquad (2.95)
$$

---

[9]equation (2.95) holds also for the structure (v), together with

$$\gamma l = (2m + 1)\mathcal{K}(\eta) - \mathcal{K}(\omega_\beta, \eta), \qquad m = 1, 2, 3, \ldots \qquad (2.93)$$

and

$$-2\eta \cos\omega_\beta\left(1 - 2\eta^2 \sin^2 \omega_\beta\right)$$

$$+2\eta \sin\omega_\beta \sqrt{1 - \eta^2 \sin^2 \omega_\beta}\left\{(2m + 1)\left[2E(\eta) - K(\eta)\right] - \left[2E(\omega_\beta, \eta) - K(\omega_\beta, \eta)\right]\right\} = 0, \qquad (2.94)$$

defining the relation between P, β and θ^* associated with the m–th bifurcation mode.

The displacement of the movable clamped edge, where the thrust is applied, can be obtained from equation (2.95), since $|u_1(l)| = l - x_1(l)$. For a given θ^* and a given even mode m, we can obtain β (through equation (2.89)), P (using equations (2.86) and (2.73)) and $|u_1(l)|$ (through equation (2.95)$_1$). The bifurcation diagram showing the load P (normalized through division by $\pi^2 B$ and multiplication by l^2) as a function of the displacement of the right movable edge of the rod (normalized through division by l) is shown in Fig. 2.8 together with the bifurcation diagram valid for the first and third symmetric buckling mode, equation (2.71).
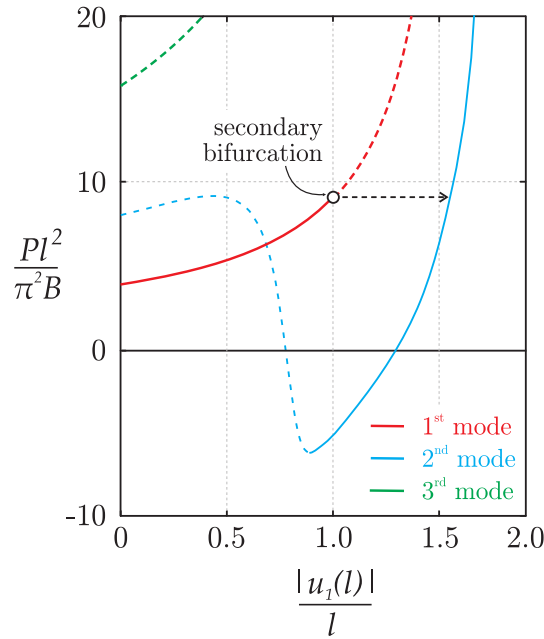
Figure 2.8: Dimensionless load $Pl^2/(\pi^2 B)$ for a doubly clamped rod versus the dimensionless displacement $|u_1(l)|/l$. The first three bifurcation points and branches are reported together the secondary bifurcation point. The solid lines represent stable equilibrium configurations, while dashed curves correspond to unstable configurations. Note that the first branch becomes unstable after the secondary bifurcation point.

2.2.4   In-plane secondary bifurcation of doubly clamped elastica

It can be noticed from Fig. 2.8 that for the doubly clamped elastica (structure (vi)) a secondary bifurcation point (marked with a circle) exists, occurring when the two edges of the rod coincide, namely, $\hat{\theta} = 130.7099°$ [10]. When

---

[10]The angle $\hat{\theta} = 130.7099°$ corresponds to the value $\kappa = 0.9089$, which is the root of the equation $2E(\kappa) - \mathcal{K}(\kappa) = 0$.
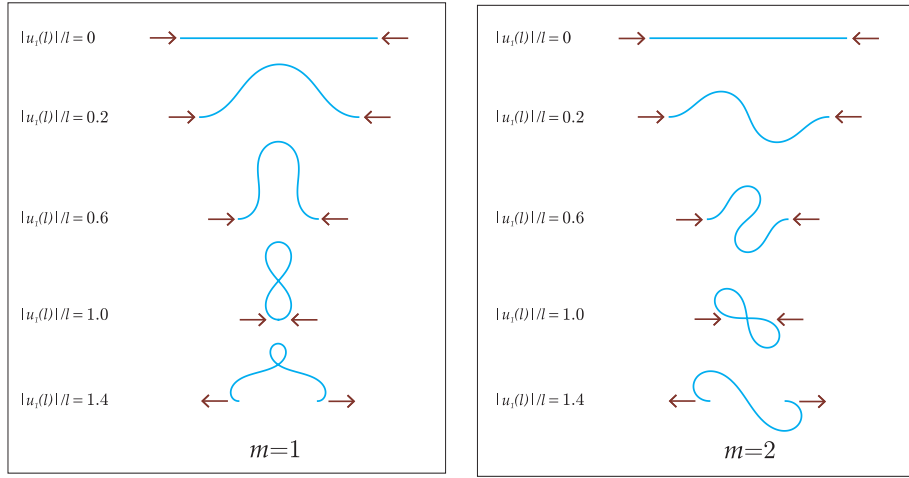
Figure 2.9: Deformed elastic lines for the first two modes $m = 1, 2$ (symmetric and antisymmetric) at different values of dimensionless displacements $|u_1(l)|/l = \{0, 0.2, 0.6, 1.0, 1.4\}$. The deformed shapes of the elastica represent the post-critical behaviour of the structure.

this value of the load is attained, the rod configuration becomes '8-shaped' (Fig. 2.9) and vertical reactions are generated at the edges, so that, increasing the thrust P the rod snaps on the stable 'S-shaped' configuration of the antisymmetric second mode [37], Fig. 2.13. Issues on stability will be addressed in the next section.

2.3 Stability of the elastica

Stability of the elastica's configurations can be judged by analyzing the second variation of the total potential energy $\mathcal{V}$ with respect to variations $\tilde{\theta}(s)$ satisfying the boundary conditions reported in equation (2.24), plus the supplementary condition

$$\int_0^l \tilde{\theta}(s) \cos \theta(s) \, \mathrm{d}s = 0, \tag{2.96}$$

following from the vanishing of the first variation of the constraint represented by equation $(2.24)_{1,5,6}$ and holding for the systems (i), (v) and (vi) in which both the edges of the rod have null vertical displacements.

The second variation of $\mathcal{V}$ can be calculated as

$$\delta^2 \mathcal{V} = \int_0^l \left[\left(\tilde{\theta}'(s) \right)^2 - \frac{P}{B} \tilde{\theta}^2(s) \cos \theta(s) + \frac{R}{B} \tilde{\theta}^2(s) \sin \theta(s) \right] , \tag{2.97}$$

which, using integration by parts

$$\int_0^l \left(\tilde{\theta}'(s) \right)^2 = -\int_0^l \tilde{\theta}''(s)\tilde{\theta}(s) \,,$$

yields

$$\delta^2 \mathcal{V} = -\int_0^l \left[\tilde{\theta}''(s) + \frac{P}{B}\tilde{\theta}(s)\cos\theta(s) - \frac{R}{B}\tilde{\theta}(s)\sin\theta(s) \right] \tilde{\theta}(s)\,\mathrm{d}s \qquad (2.98)$$

for all admissible $\tilde{\theta}(s)$, subject to the different boundary conditions, in relation with the considered structural system. Therefore, the *stability criterion* is

$$\delta^2 \mathcal{V} \begin{cases} > 0 & \text{stability} \\ \\ < 0 & \text{instability} \end{cases} \qquad (2.99)$$

In order to treat condition (2.98), let us denote with $\phi_n(s)$ ($s \in [0, l]$) the non-trivial solutions of the following Sturm-Liouville problem[11]

$$\phi_n''(s) + \delta_n \left(\frac{P}{B}\cos\theta(s) - \frac{R}{B}\sin\theta(s) \right) \phi_n(s) = C_{Rn}\cos\theta(s), \qquad (2.101)$$

subject to the following constraints representing the boundary conditions (2.24)

i) $\phi_n'(0) = \phi_n'(l) = 0$ and $\displaystyle\int_0^l \cos\theta(s)\phi_n(s)\mathrm{d}s = 0$

ii) $\phi_n'(0) = \phi_n(l) = 0$

iii) $\phi_n(0) = \phi_n'(l) = 0$

iv) $\phi_n(0) = \phi_n(l) = 0$ $\qquad\qquad\qquad\qquad\qquad\qquad\qquad$ (2.102)

v) $\phi_n(0) = \phi_n'(l) = 0$ and $\displaystyle\int_0^l \cos\theta(s)\phi_n(s)\mathrm{d}s = 0$

vi) $\phi_n(0) = \phi_n(l) = 0$ and $\displaystyle\int_0^l \cos\theta(s)\phi_n(s)\mathrm{d}s = 0$

---

[11]When isoperimetric constraints are not present, namely there is not the condition (2.96), stability can be also addressed evaluating the eigenvalues δ_n of the following Sturm-Liouville problem

$$- \phi_n''(s) - \left(\frac{P}{B}\cos\theta(s) - \frac{R}{B}\sin\theta(s) \right) \phi_n(s) = \delta_n\phi_n(s). \qquad (2.100)$$

When at least one eigenvalue is negative, the associated equilibrium configuration is *unstable*, while, if all eigenvalues are positive, the equilibrium is *stable*, see Manning et al. [23] and Hoffman et al. [24].

where $\phi_n(s)$ are the eigenfunctions associated to the eigenvalues δ_n with weight function

$$\frac{P}{B}\cos\theta(s) - \frac{R}{B}\sin\theta(s), \tag{2.103}$$

and C_{Rn} is a constant that represents the isoperimetric constraint (2.96) and 'has the meaning of R', so that in the unconstrained systems (for systems (ii), (iii), (iv) and (i), except when the two supports coincide) $C_{Rn} = 0$.

It is known (see for instance Broman [34]) that: (i.) problem (2.101) admits a countably infinite set of eigenvalues δ_n and these can be arranged in an increasing sequence ($\delta_n < \delta_{n+1}$ for each integer n)[12], (ii.) $\delta_n \longrightarrow \infty$ when $n \longrightarrow \infty$, (iii.) the system $\phi_n(s)$, $s \in [0, l]$ is an orthogonal system with the weight function (2.103). Multiplication of the differential equation (2.101) by ϕ_n and integration between 0 and l yields (keeping into account the boundary conditions (2.102) and using integration by parts)

$$\delta_n \int_0^l \left(\frac{P}{B}\cos\theta(s) - \frac{R}{B}\sin\theta(s)\right)\phi_n^2(s)\,\mathrm{d}s = \int_0^l (\phi_n'(s))^2\,\mathrm{d}s, \tag{2.104}$$

while writing equation (2.101) for the eigenfunction ϕ_m

$$\phi_m''(s) + \delta_m\left(\frac{P}{B}\cos\theta(s) - \frac{R}{B}\sin\theta(s)\right)\phi_m(s) = C_{Rm}\cos\theta(s), \tag{2.105}$$

combining equations (2.101) and (2.105) multiplied by ϕ_m and ϕ_n respectively, integrating between 0 and l and taking into account boundary conditions, the following orthogonality condition is obtained

$$\int_0^l \phi_n(s)\phi_m(s)\left(\frac{P}{B}\cos\theta(s) - \frac{R}{B}\sin\theta(s)\right)\mathrm{d}s = 0, \quad n \neq m. \tag{2.106}$$

Condition (2.104) defines a norm and equation (2.106) a weighted orthogonality condition for the functions $\phi_n(s)$ with weight function (2.103).

Therefore, system $\phi_n(s)$ with weight function (2.103) can be used to give a Fourier series representation (converging in the mean) to the square-integrable function $\tilde{\theta}(s)$,

$$\tilde{\theta}(s) = \sum_{n=1}^{\infty} c_n\phi_n(s), \tag{2.107}$$

where c_n are the Fourier coefficients.

We do not need to specify coefficients c_n, rather we can simply substitute the Fourier representation (2.107) into condition (2.98) and keep into

---

[12]$\delta_n \geq 0$, see [34], pag. $41 - 44$.

consideration equation (2.101) to obtain

$$\delta^2\mathcal{V} = \int_0^l \left[\sum_{n=1}^\infty (\delta_n - 1) c_n \phi_n(s) \left(\frac{P}{B} \cos\theta(s) - \frac{R}{B} \sin\theta(s) \right) \right] \\ \times \left[\sum_{m=1}^\infty c_m \phi_m(s) \right] \mathrm{d}s \tag{2.108}$$

which, employing conditions (2.104) and (2.106) finally becomes

$$\delta^2\mathcal{V} = \sum_{n=1}^\infty (1 - \frac{1}{\delta_n}) c_n^2 \int_0^l (\phi_n'(s))^2 \,\mathrm{d}s \quad \begin{cases} > 0 & \text{stability} \\ \\ < 0 & \text{instability} \end{cases} \tag{2.109}$$

so that we arrive at the stability requirement

$$\begin{cases} \delta_n \notin [0,1] & \text{stability} \\ \\ \delta_n \in [0,1] & \text{instability} \end{cases} \tag{2.110}$$

where δ_n are solutions of the Sturm-Liouville problem (2.101). The values $\delta_n = 0$ or $\delta_n = 1$ represent 'transition' points and thus are called 'critical'.

2.3.1 Stability of the simply supported elastica

Let us begin considering the stability of the straight configuration of the simply supported rod, $\cos\theta(s) = 1$. In this case, the Sturm-Liouville problem (2.101), with $R = C_{Rn} = 0$ becomes

$$\phi_n''(s) + \delta_n \frac{P}{B} \phi_n(s) = 0, \quad \phi_n'(0) = \phi_n'(l) = 0, \tag{2.111}$$

which has the nontrivial solutions

$$\phi_n(s) = \cos\frac{n\pi s}{l}, \quad \delta_n = \frac{P_n^{cr}}{P}, \tag{2.112}$$

where P_n^{cr} are the Euler's critical loads at different modes n, equation (2.31), so that when $\delta_1 < 0$ or $\delta_1 > 1$ $(0 < \delta_1 < 1)$ the straight configuration is stable (unstable), which corresponds to $P < P_1^{cr}$ $(P > P_1^{cr})$[13].

---

[13]This statements is valid also for the other systems with $R = 0$, namely (ii), (iii) and (iv), whose nontrivial solutions are

ii) $\phi_n(s) = \cos\dfrac{\pi + 2n\pi}{2} \dfrac{s}{l}$

iii) $\phi_n(s) = \sin\dfrac{\pi + 2n\pi}{2} \dfrac{s}{l}$

iv) $\phi_n(s) = \sin\dfrac{n\pi s}{l}$

and $\delta_n = \dfrac{P_n^{cr}}{P}$.

To judge stability of the deformed elastica, we can substitute equation (2.41) into equation (2.50) to obtain

$$\cos\theta(s) = 1 - 2\kappa^2 \operatorname{sn}^2\left[\left(\frac{s}{l}2m + 1\right)\mathcal{K}(\kappa), \kappa\right], \tag{2.113}$$

and rewrite with the nondimensional variable $\tilde{s} = s/l \in [0,1]$ the Sturm-Liouville problem (2.101), so that for a given mode m and inclination of the rod edge $\kappa = \sin(\hat{\theta}/2)$ the *smallest eigenvalue* δ_m has to be determined as the solution of

$$\phi_m''(\tilde{s}) + \delta_m\, 4m^2\mathcal{K}^2(\kappa)\left\{1 - 2\kappa^2\operatorname{sn}^2\left[(2m\,\tilde{s}+1)\mathcal{K}(\kappa), \kappa\right]\right\}\phi_m(\tilde{s}) = 0, \tag{2.114}$$

(where $'$ denotes differentiation with respect to $\tilde{s}$) subject to the boundary conditions $(2.101)_2$, namely $\phi_m'(0) = \phi_m'(1) = 0$.

Problem (2.114) can be easily solved with a numerical routine. As noticed by Kuznestov and Levyakov [29], a numerical procedure can be easily set, solving the differential equation (2.114) with the boundary conditions

$$\phi_m(0) = 1, \quad \phi_m'(0) = 0, \tag{2.115}$$

so that the trivial solution is always eliminated and iterations on δ_m can be performed to match the condition $\phi_m'(1) = 0$ [14]. The iterations have been performed on the basis of a bisection method and the integration produces the graphs reported in Fig. 2.10. The smallest eigenvalues δ_m for the first three modes $m = 1, 2, 3$ are reported versus the inclination $\hat{\theta}$ (in degrees) of the ends of the deformed rod. It is clear that the first mode, $m = 1$, is stable (the eigenvalues range between 1 and 10) until the two supports coincide for $\hat{\theta} = 130.7099°$, at which point the eigenvalues become discontinuous and fall to values within $[0,1]$ (in particular, $\delta_1 = 9.9228$ at $\hat{\theta} = 130.7°$ and $\delta_1 = 0.0059$ at $\hat{\theta} = 130.8°$). All modes higher than the first ($m = 2, 3$) are unstable with eigenvalues belonging to $[0,1]$. Note that for all the considered modes the eigenvalues for $\hat{\theta} \geq 130.7099°$ are all coincident with the values for $m = 1$.

The instability mode associated to the unstable configurations occurring for $m = 1$ and $\hat{\theta} > 130.7099°$ (discovered by Maddocks [22]) and corresponding to 'self-intersecting' elastica is not easy to be illustrated and understood.

---

[14] The nontrivial solution of the Sturm-Liouville problem (2.101) for the systems (ii), (iii) and (iv) can be numerically found using the following boundary conditions

  ii) $\phi_m'(0) = 0, \quad \phi_m(l) = 0, \quad \phi_m(0) = 1,$

  iii) $\phi_m(0) = 0, \quad \phi_m'(l) = 0, \quad \phi_m(l) = 1,$

  iv) $\phi_m(0) = 0, \quad \phi_m(l) = 0, \quad \phi_m'(0) = 1.$

For all these systems, the first mode, $m = 1$, is stable (no eigenvalues belong to $[0,1]$), while upper investigated modes, $m = 2, 3$ are unstable with at least one eigenvalue belonging to $[0,1]$.
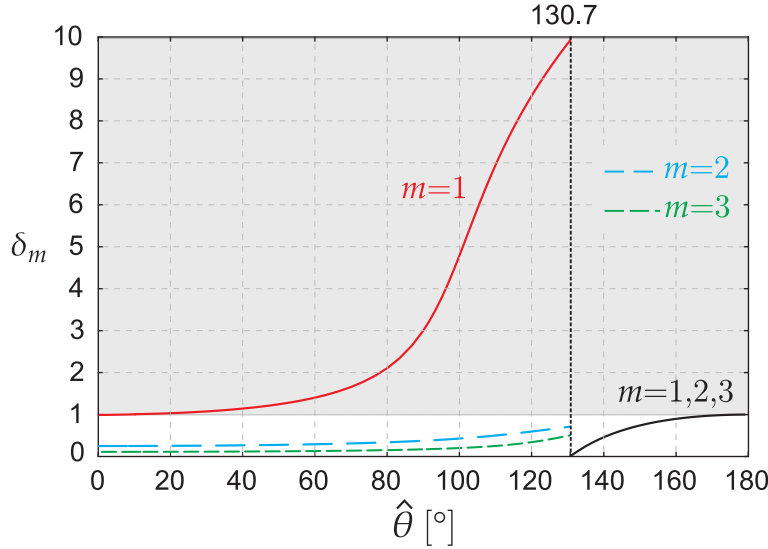
Figure 2.10: The smallest eigenvalues δ_m for the Sturm-Liouville problem (2.114) as functions of the rotation $\hat{\theta}$ of the ends of the rod. These determine the stability of the different modes of elastica ($m = 1, 2, 3$ are investigated). The light gray region corresponds to stability, so that only the first mode $m = 1$ is stable and only until the two supports of the rod coincide, a situation corresponding to $\hat{\theta} = 130.7099°$.

Therefore, we have performed an experiment with the beam model shown in Fig. 2.11, made up of an AISI 1095 steel strip ($180\,\text{mm} \times 12\,\text{mm} \times 0.07\,\text{mm}$), having a 7 mm wide cut, dividing the strip into two parts (one 5 mm wide and the other '∩-shaped' with each of the two legs 2.5 mm wide). The model is suspended vertically in a self-intersecting configuration, in equilibrium with a 7 g dead weight. This equilibrium is only possible due to a 'minimal' friction between a contact point internal to the '∩-shaped' part of the rod. If this configuration is just touched, the curved loop moves and flips around one hinge so violently that the images shown in Fig. 2.12 are blurred although taken with $1/500\,\text{s}$ exposure time (a Genie HM1400, DALSA Corporation) of a high speed camera (equipped with a 18-35mm 1:3.5-4.5 D AF Nikkor lens, from Nikon Corporation, at 50 shots per second).

We finally note that with the proposed procedure to check stability of the elastica configurations it is not directly possible to conclude that *all* modes $m > 1$ are unstable, though mechanical considerations suggest that this might be the case. Our check of the instability of the modes $m = 2, 3$ substantiates the Love's [15] statement 'the instability of forms of the elastica with more than the smallest possible number of inflexions between the ends is well known as an experimental fact'.
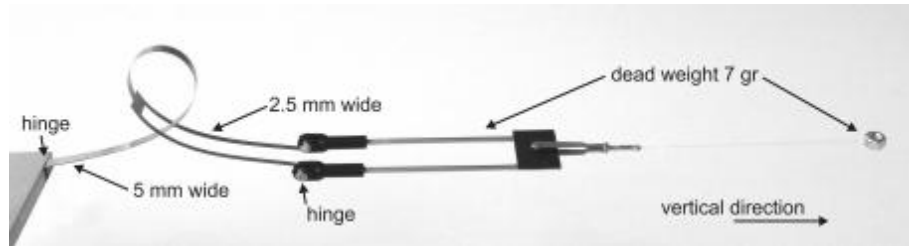
Figure 2.11: An unstable configuration of a rod model used to experimentally check the instability of 'self-intersecting elastica' (cut from a $180\,\text{mm} \times 12\,\text{mm} \times 0.07\,\text{mm}$ steel strip) suspended vertically and subject to a $7\,\text{g}$ weight. The unstable configuration is maintained due to a minimal friction at one intersection point. A gentle movement of air is sufficient to break equilibrium, thus generating the motion recorded in Fig. 2.12.
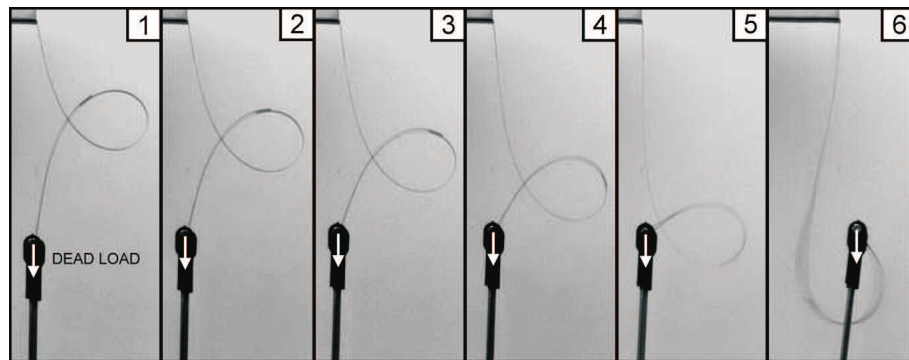
Figure 2.12: Experiment documenting the instability of 'self-intersecting elastica': the curved loop moves vertically towards the hinge and finally flips around this at the bottom of the sample. Photos have been taken at a speed of 50 shots per second, with an exposure time of $1/500\,\text{s}$.

2.3.2 Stability of the doubly clamped elastica

The stability of the straight configuration of the doubly clamped rod (vi) can be analyzed considering that $\sin\theta(s) = 0$ and $\cos\theta(s) = 1$, therefore the Sturm-Liouville problem (2.101) becomes

$$\phi_n''(s) + \delta_n \frac{P}{B} \phi_n(s) = C_{Rn}, \quad \phi_n(0) = \phi_n(l) = 0, \quad \int_0^l \phi_n(s)\mathrm{d}s = 0 \quad (2.116)$$

where the solutions of this differential problem is

$$\phi_n(s) = A_1 \cos\left[\sqrt{\frac{\delta_n P}{B}}\, s\right] + A_2 \sin\left[\sqrt{\frac{\delta_n P}{B}}\, s\right] + \frac{A_3 B}{\delta_n P}, \quad (2.117)$$

so that inserting solution (2.117) into the boundary conditions in (2.116) we arrive at a system of equations for A_1, A_2 and A_3 which can be written in the following matrix form

$$\begin{bmatrix} \dfrac{\delta_n P}{B} & 0 & 1 \\ \cos\left[\sqrt{\dfrac{\delta_n P}{B}}\, l\right] & \sin\left[\sqrt{\dfrac{\delta_n P}{B}}\, l\right] & \dfrac{B}{\delta_n P} \\ \dfrac{\delta_n P}{B}\sin\left[\sqrt{\dfrac{\delta_n P}{B}}\, l\right] & \dfrac{\delta_n P}{B}\cos\left[\sqrt{\dfrac{\delta_n P}{B}}\, l\right] & l \end{bmatrix} \begin{bmatrix} A_1 \\ A_2 \\ A_3 \end{bmatrix} = \begin{bmatrix} 0 \\ 0 \\ 0 \end{bmatrix}. \quad (2.118)$$

The non trivial solution of (2.117) can be obtained when the following determinant of the previous matrix is null

$$2\left(\cos\left[\sqrt{\frac{\delta_n P}{B}}\, l\right] - 1\right) + \sqrt{\frac{\delta_n P}{B}}\, l \sin\left[\sqrt{\frac{\delta_n P}{B}}\, l\right] = 0, \quad (2.119)$$

so that δ_n can be numerically obtained showing that the straight configuration is stable only for $P < P_1^{cr}$, whereas for $P > P_1^{cr}$ at least one eigenvalue δ_n belongs to $[0, 1]$, therefore those configurations are unstable.

To investigate stability of the deformed elastica, the numerical procedure proposed by Levyakov and Kuznetsov [32] is reported in the following and, where feasible, we retain as much of the notation and conventions of [32] as possible[15]. The Sturm-Liouville problem (2.101) can be rewritten with the nondimensional variable $\tilde{s} = s/l \in [0, 1]$ for a given mode m as

$$\phi_m''(\tilde{s}) + \delta_m L(\tilde{s})\,\phi_m(\tilde{s}) = C_{Rm} N(\tilde{s}), \quad (2.120)$$

---

[15]The analysis of stability with isoperimetric constraints can be also performed following Manning et al. [23], Hoffman et al. [24] and Manning [25, 26] through the conjugate point theory.

where

$$
L(\tilde{s}) = \begin{cases} \dfrac{P}{B}\cos\theta(\tilde{s}) & \text{for odd modes} \\[2ex] \dfrac{P}{B}\cos\theta(\tilde{s}) - \dfrac{R}{B}\sin\theta(\tilde{s}) & \text{for even modes} \end{cases} \qquad (2.121)
$$

and $N(\tilde{s}) = \cos\theta(\tilde{s})$. Note that, for the odd buckling modes with $2m$ inflextion points, equation (2.68) can be inserted into the definition of $\cos\theta(s)$, similarly to equation (2.50), to obtain

$$
\cos\theta(\tilde{s}) = 1 - 2\kappa^2 \operatorname{sn}^2\left[(2(m+1)\tilde{s})\,\mathcal{K}(\kappa), \kappa\right], \qquad m = 1, 3, 5, \qquad (2.122)
$$

where it is a function of the inclination of the rod inflection point $\hat{\theta}$, while for the even buckling modes with $2m+1$ inflection points we can write

$$
\begin{aligned}
\cos\theta(\tilde{s}) &= \sin\beta\left[2\eta\operatorname{sn}\left[\gamma\tilde{s} + \mathcal{K}(\omega_\beta, \eta), \eta\right]\operatorname{dn}\left[\gamma\tilde{s} + \mathcal{K}(\omega_\beta, \eta), \eta\right]\right] \\
&\quad + \cos\beta\left[1 - 2\eta^2\operatorname{sn}^2\left[\gamma\tilde{s} + \mathcal{K}(\omega_\beta, \eta), \eta\right]\right], \\[1.5ex]
\sin\theta(\tilde{s}) &= \cos\beta\left[2\eta\operatorname{sn}\left[\gamma\tilde{s} + \mathcal{K}(\omega_\beta, \eta), \eta\right]\operatorname{dn}\left[\gamma\tilde{s} + \mathcal{K}(\omega_\beta, \eta), \eta\right]\right] \\
&\quad - \sin\beta\left[1 - 2\eta^2\operatorname{sn}^2\left[\gamma\tilde{s} + \mathcal{K}(\omega_\beta, \eta), \eta\right]\right],
\end{aligned} \qquad (2.123)
$$

and the parameters β, γ, P and R can be calculated through equations (2.89), (2.86) and (2.73) as a function of the inclination of the rod at inflection point θ^*.

Equation (2.120) is subjected to the boundary conditions $\phi_m(0) = 0$, $\phi_m(1) = 0$ and the constraint [16]

$$
\int_0^1 \phi_m(\tilde{s})N(\tilde{s})\mathrm{d}\tilde{s} = 0. \qquad (2.124)
$$

The numerical method for calculating the eigenvalues δ_m consist of dividing the interval $0 \leq \tilde{s} \leq 1$ into n segments of equal length $h = n^{-1}$ and denoting the coordinate of the starting points of the segments by $s_{i-1} = h(i-1)$, with $i = 1, ..., n$. For the ith segment, the functions $L(\tilde{s})$ and $N(\tilde{s})$ are approximated by their average values L_i and N_i calculated at the midpoint of the ith segment, so that equation (2.120) becomes

$$
\phi_m''(\tilde{s}) + \delta_m\, L_i\, \phi_m(\tilde{s}) = C_{Rm}\, N_i, \qquad (2.125)
$$

which is an ordinary differential equation with constant coefficients. The solution equation (2.125) is

$$
\phi_m(\tilde{s}) = A_{1i}F_{1i}(\tilde{s} - \tilde{s}_{i-1}) + A_{2i}F_{2i}(\tilde{s} - \tilde{s}_{i-1}) + C_{Rm}\frac{N_i}{\delta_n L_i}, \qquad (2.126)
$$

---

[16] for system (v) the boundary conditions are $\phi_m(0) = \phi_m'(1) = 0$, while the constraint remains $\int_0^1 \phi_m(\tilde{s})N(\tilde{s})\mathrm{d}\tilde{s} = 0$

where A_{1i} and A_{2i} are constants, whereas the coefficients F_{1i} and F_{2i} are defined for $\delta_m L_i > 0$ as

$$F_{1i}(\tilde{s} - \tilde{s}_{i-1}) = \cos a_i(\tilde{s} - \tilde{s}_{i-1}) \qquad F_{2i}(\tilde{s} - \tilde{s}_{i-1}) = \sin a_i(\tilde{s} - \tilde{s}_{i-1}) \quad (2.127)$$

while for $\delta_m L_i < 0$ they are

$$F_{1i}(\tilde{s} - \tilde{s}_{i-1}) = \cosh a_i(\tilde{s} - \tilde{s}_{i-1}) \qquad F_{2i}(\tilde{s} - \tilde{s}_{i-1}) = \sinh a_i(\tilde{s} - \tilde{s}_{i-1}) \quad (2.128)$$

with $a_i = \sqrt{|\delta_m L_i|}$.

The constants A_{1i} and A_{2i} can be expressed by means of $\phi_m(\tilde{s}_{i-1}) = \phi_{m,i-1}$ and $\phi'_m(\tilde{s}_{i-1}) = \phi'_{m,i-1}$ as

$$A_{1i} = \phi_{m,i-1} - C_{Rm}\frac{N_i}{\delta_m L_i}, \qquad A_{2i} = \frac{\phi'_{m,i-1}}{a_i}, \qquad (2.129)$$

so that the quantity $\phi_m(\tilde{s}_i) = \phi_{m,i}$ at the right end of the segment are calculated

$$\phi_{m,i} = \phi_{m,i-1} F_{1i}(h) + \phi'_{m,i-1}\frac{F_{2i}(h)}{a_i} + C_{Rm}N_i\frac{1 - F_{1i}(h)}{\delta_m L_i}, \qquad (2.130)$$

as well as its derivative

$$\phi'_{m,i} = \phi_{m,i-1} F'_{1i}(h) + \phi'_{m,i-1}\frac{F'_{2i}(h)}{a_i} - C_{Rm}N_i\frac{F'_{1i}(h)}{\delta_m L_i}. \qquad (2.131)$$

Equations (2.130) and (2.131) have to be used for constructing the general solution of equation (2.125) satisfying the condition of continuity of ϕ_m and ϕ'_m at the ends of each integration segments. Since equation (2.125) is linear, its general solution can be written as a combination of three particular solutions

$$\phi_m(\tilde{s}) = c_1\varphi_1(\tilde{s}) + c_2\varphi_2(\tilde{s}) + C_{Rm}\varphi_3(\tilde{s}), \qquad (2.132)$$

where c_1 and c_2 are constants. Using the following initial data

$$\varphi_1(0) = 1, \qquad \varphi'_1(0) = 0, \qquad C_{Rm} = 0,$$
$$\varphi_2(0) = 0, \qquad \varphi'_2(0) = 1, \qquad C_{Rm} = 0, \qquad (2.133)$$
$$\varphi_3(0) = 0, \qquad \varphi'_3(0) = 0, \qquad C_{Rm} = 1,$$

the functions $\varphi_i(\tilde{s})$ ($i = 1, 2, 3$) can be constructed separately using the recurrence relations (2.130) and (2.131). Note that solutions $\varphi_i(\tilde{s})$ can be directly obtained solving numerically the differential equation (2.120) (where $\phi_m(\tilde{s})$ is substituted with $\varphi_i(\tilde{s})$) through NDSolve of Mathematica$^{©}$ with the boundary conditions (2.133).

Inserting the general solution (2.132) into relation (2.124), the constraint can be rewritten as

$$\int_0^1 \left[c_1 \varphi_1(\tilde{s}) + c_2 \varphi_2(\tilde{s}) + C_{Rm} \varphi_3(\tilde{s}) \right] N(\tilde{s}) \mathrm{d}\tilde{s} = 0, \qquad (2.134)$$

while the boundary conditions $\phi_m(0) = 0$ and $\phi_m(1) = 0$ bring to the following relations

$$c_1 = 0,$$
$$c_1 \varphi_1(1) + c_2 \varphi_2(1) + C_{Rm} \varphi_3(1) = 0. \qquad (2.135)$$

Equations (2.134) and (2.135)$_2$ constitute a homogeneous system of algebraic equation for c_2 and C_{Rm} which can be written in the matrix form

$$\begin{bmatrix} \varphi_2(1) & \varphi_3(1) \\ \int_0^1 \varphi_2(\tilde{s}) N(\tilde{s}) \mathrm{d}\tilde{s} & \int_0^1 \varphi_3(\tilde{s}) N(\tilde{s}) \mathrm{d}\tilde{s} \end{bmatrix} \begin{bmatrix} c_2 \\ C_{Rm} \end{bmatrix} = \begin{bmatrix} 0 \\ 0 \end{bmatrix}. \qquad (2.136)$$

The non trivial solution of the system (2.136) can be obtained imposing the vanishing of the matrix's determinant Δ, so that, varying the eigenvalue δ_m from 0 to 1 we can study the behaviour of Δ. If exists at least a value of $\delta_m \in [0; 1]$ such as $\Delta = 0$, the non trivial solution of (2.132) satisfies boundary conditions and the corresponding equilibrium is *unstable*, otherwise it is *stable*. Therefore, for the doubly clamped elastica the study of stability can be conducted analyzing the determinant Δ, which becomes[17]

$$\Delta = \varphi_2(1) \int_0^1 \varphi_3(\tilde{s}) N(\tilde{s}) \mathrm{d}\tilde{s} - \varphi_3(1) \int_0^1 \varphi_2(\tilde{s}) N(\tilde{s}) \mathrm{d}\tilde{s}, \qquad (2.137)$$

where the integrals have to be numerically solved. The above mentioned numerical procedure bring to the results of stability (solid curve) or instability (dashed curve) reported in Fig. 2.8, showing clearly the secondary bifurcation and the jump from the first to the second mode once the two edges of the rod are overlapped.

In order to understand the instability mode associated to the unstable configurations occurring for $m = 1$ and $\hat{\theta} > 130.7099°$ and corresponding to 'self-intersecting' elastica an experiment has been performed with the beam model made up of a PMMA strip (490 mm $\times$ 15 mm $\times$ 1.5 mm), having a 13 mm wide cut, dividing the strip into two parts (one 12 mm wide and the other '∩-shaped' with each of the two legs 6 mm wide). Four configurations have been reported in Fig. 2.13, confirming theoretical predictions.

---

[17]for the system (v) the determinant is $\Delta = \varphi_2'(1) \int_0^1 \varphi_3(\tilde{s}) N(\tilde{s}) \mathrm{d}\tilde{s} - \varphi_3'(1) \int_0^1 \varphi_2(\tilde{s}) N(\tilde{s}) \mathrm{d}\tilde{s}$
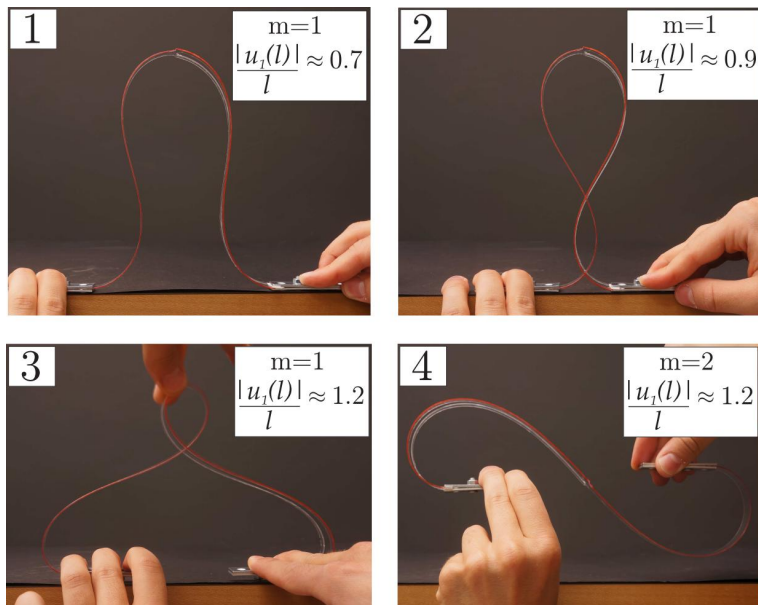
Figure 2.13: Experiment documenting the analytical results obtained for the doubly clamped elastica: (1) and (2) confirm the stability of the first mode; (3) shows the instability (note that this configuration must be held in this position with one hand, otherwise it slips into configuration (4)) of the first symmetric mode after secondary bifurcation point, when the two edges of the rod are overlapped; and (4) certifies the stability of the second 'S-shaped' antisymmetric mode when $|u_1(l)|/l > 1$.

Chapter 3

The existence of Eshelby-like force in elastic structures

> The Eshelbian (or configurational) force is the main concept of a celebrated theoretical framework associated with the motion of dislocations and, more in general, defects in solids. In a similar vein, in an elastic structure where a (smooth and bilateral) constraint can move and release energy, a force driving the configuration is generated, which therefore is called by analogy 'Eshelby-like' or 'configurational'. This force (generated by a specific movable constraint) is derived both via variational calculus and, independently, through an asymptotic approach. Its action on the elastic structure is counterintuitive, but is fully substantiated and experimentally measured on a model structure that has been designed, realized and tested.

Configurational (or: 'material', 'driving', 'non-Newtonian') forces have been introduced by Eshelby [1–4] to describe the fact that massless (for instance: voids, microcracks, vacancies, or dislocations) or heavy (for instance inclusions) defects may move within a solid body as a result of mechanical or thermal loading. The Eshelbian force is defined as the negative gradient of the total potential energy $\mathcal{V}$ of a body with respect to the parameter κ determining the configuration of the defect, namely,

$$-\frac{\partial \mathcal{V}(\kappa)}{\partial \kappa}. \tag{3.1}$$

Examples are the crack-extension force of fracture mechanics, the Peach–Koehler force of dislocations, or the material force developing on a phase boundary in a solid under loading. Nowadays configurational forces are the cornerstone of a well-developed theory (see for instance the monographs by Gurtin [5], Kienzler and Herrmann [6], and Maugin [7, 8], and the journal special issues by Dascalu et al. [38], and Bigoni and Deseri [39]).

Let us consider an elastic structure in equilibrium upon load and assume that a (frictionless and bilateral) constraint can move – a feature which may
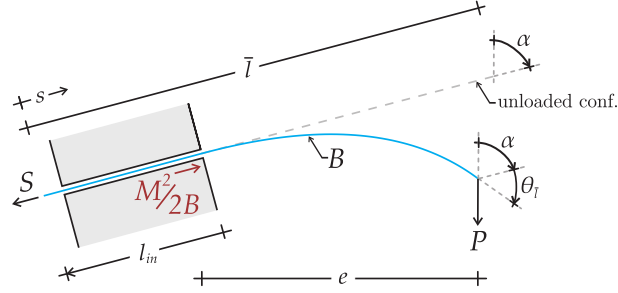
Figure 3.1: Structural scheme of the elastic system employed to disclose a Eshelby-like force. The elastic rod of total length $\bar{l}$ is subject to a dead vertical load P on its right end, is constrained with a sliding sleeve inclined at an angle α (with respect to the vertical) and has a axial dead force S applied at its left end. The presence of the Eshelby-like force $M^2/(2B)$ influences the force S at equilibrium, which results different from $P\cos\alpha$. The other reactions at the end of the sliding sleeve are the force $P\sin\alpha$ perpendicular to the axis of the sleeve and the counterclockwise reaction moment Pe.

be considered as a 'defect' – in a way to allow the system to reconfigure through a release of elastic energy, then a force is generated, similar to an Eshelbian or configurational one.

To reveal this force in an indisputable way, and directly measure it, the simple elastic structure sketched in Fig. 3.1 has been designed, which inflectionlength can change through sliding along a sleeve and therefore discloses (in two different and independent ways, namely, using variational and asymptotic approaches) the presence of an Eshelby-like force. The structure has been subsequently realized and instrumented (see Fig. 3.2, reporting a series of photos demonstrating the action of the Eshelby-like force), so that the configurational force has been measured at equilibrium and it is shown to perfectly match the theoretical predictions.

In this example configurational forces are non-zero, but small for small deflections[1] and become progressively important when displacements grow. Their effects are counterintuitive and unexpected, so that for instance, the structure shown in Fig. 3.2, which can wrongly be thought to be unable to provide any axial action, is instead subject to an axial Eshelby-like force transmitted by the sliding sleeve. In particular, at the end of the sliding sleeve, the axial force S at equilibrium with a load P (inclined of α with respect to the rod's axis) is not simply equal to $-P\cos\alpha$, as when the sliding sleeve is replaced by a clamp, but will be determined (Section 3.1.3) to be a

---

[1] The fact that these forces are small for small displacement does not mean that they are always negligible, since their action is in a particular direction, which may be 'unexpected'. For instance, in the case of null axial dead load, $S = 0$, and sliding sleeve orthogonal to the vertical dead load P, $\alpha = \pi/2$ (Fig. 3.1), the Eshelby-like force is the only axial action, so that equilibrium becomes impossible.
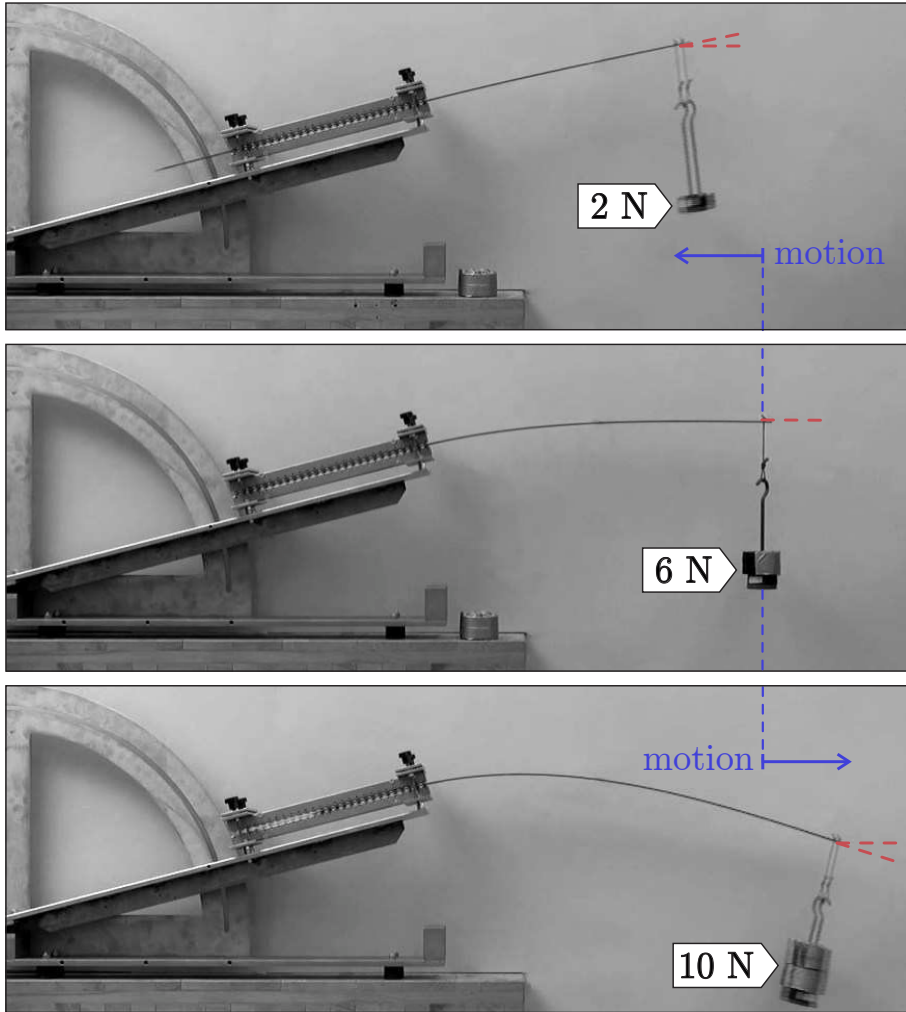
Figure 3.2: The practical realization of the elastic structure shown in Fig. 3.1 reveals an axial Eshelby-like force, so that, while at low vertical force (2 N) the elastic rod tends, as expected, to slip inside the sliding sleeve (upper photo), at 6 N the equilibrium is surprisingly possible (note that the tangent at the loaded end of the elastic rod is horizontal, see the photo in the centre) and at 10 N the elastic rod is expelled from the sliding sleeve (lower photo), even if the system is inclined at 15° with respect to the horizontal ($\alpha = 75°$).

function of the rotation of the rod at its end, $\theta_{\bar{l}}$, as

$$S = -P\cos\left(\alpha + \theta_{\bar{l}}\right) = -P\cos\alpha + \underbrace{2P\left(\sin^2\frac{\theta_{\bar{l}} + \alpha}{2} - \sin^2\frac{\alpha}{2}\right)}_{\text{Eshelby-like force}}, \qquad (3.2)$$

which for for small deflections ($\sin\theta_{\bar{l}} \approx \theta_{\bar{l}}$) becomes

$$S = -P\cos\alpha + \underbrace{P\frac{3\,v_{\bar{l}}}{2(\bar{l} - l_{in})}\sin\alpha}_{\text{Eshelby-like force}}, \qquad (3.3)$$

where $v_{\bar{l}}$ is the transversal displacement at the loaded end of the rod of length $\bar{l} - l_{in}$ (external to the sliding sleeve). Equations (3.2) and (3.3) show that there is an 'unexpected' term (null if the elastic rod is constrained by a clamp instead of a sliding sleeve), defined as the 'Eshelby-like force'. Although there is a little abuse of notation[2], this definition is motivated by the fact that the Eshelby-like force is null, would the total potential energy of the system be independent of a configurational parameter.

3.1 Eshelby-like force produced by a sliding sleeve

An inextensible elastic rod (straight in its unloaded configuration, with bending stiffness B and total length $\bar{l}$) has one end constrained with a sliding sleeve, is subject to an edge axial (dead) force S, and has the other end subject to a dead transversal load P (inclined at an angle α, see Fig. 3.1). Introducing the curvilinear coordinate $s \in [0, \bar{l}]$, the length l_{in} of the segment of the rod internal to a (frictionless, perfectly smooth and bilateral) sliding sleeve, and the rotation $\theta(s)$ of the rod's axis, it follows that $\theta(s) = 0$ for $s \in [0, l_{in}]$. Denoting by a prime the derivative with respect to s, the bending moment along the elastic rod is $M(s) = B\theta'(s)$, so that at the loaded edge of the rod, we have the zero-moment boundary condition $\theta'(\bar{l}) = 0$.

The total potential energy of the system is

$$\mathcal{V}(\theta(s), l_{in}) = B \int_{l_{in}}^{\bar{l}} \frac{\left[\theta'(s)\right]^2}{2} \mathrm{d}s - P\left[\bar{l}\cos\alpha - \cos\alpha \int_{l_{in}}^{\bar{l}} \cos\theta(s)\mathrm{d}s \right.$$

$$\left. + \sin\alpha \int_{l_{in}}^{\bar{l}} \sin\theta(s)\mathrm{d}s\right] - S\,l_{in}, \qquad (3.4)$$

---

[2] The introduction of the nomenclature 'Eshelby-like force' allows to distinguish terms generated by the possibility of configurational changes of the system, while 'Eshelby forces' must always vanish at equilibrium.

which at equilibrium becomes

$$\mathcal{V}(\theta_{eq}(s, l_{eq}), l_{eq}) = B \int\limits_{l_{eq}}^{\bar{l}} \frac{\left[\theta'_{eq}\left(s, l_{eq}\right)\right]^2}{2} \mathrm{d}s - P \Bigg[\bar{l} \cos \alpha$$

$$- \cos \alpha \int\limits_{l_{eq}}^{\bar{l}} \cos \theta_{eq}(s, l_{eq}) \mathrm{d}s + \sin \alpha \int\limits_{l_{eq}}^{\bar{l}} \sin \theta_{eq}(s, l_{eq}) \mathrm{d}s \Bigg]$$

$$- S\, l_{eq},$$

(3.5)

where l_{eq} is the length of the elastic rod inside the sliding sleeve and θ_{eq} the rotation of the rod's axis at the equilibrium configuration.

Before proceeding, we remember the that, for an integral defined as

$$I(\zeta) = \int\limits_{\alpha(\zeta)}^{\beta(\zeta)} f(x, \zeta) \mathrm{d}x$$

(3.6)

the Leibniz rule of differentation is

$$\frac{\mathrm{d}I(\zeta)}{\mathrm{d}\zeta} = f(\beta, \zeta) \frac{\mathrm{d}\beta}{\mathrm{d}\zeta} - f(\alpha, \zeta) \frac{\mathrm{d}\alpha}{\mathrm{d}\zeta} + \int\limits_{\alpha(\zeta)}^{\beta(\zeta)} \frac{\partial f(x, \zeta)}{\partial \zeta} \mathrm{d}x.$$

(3.7)

The Eshelbian force related to the sliding in the sleeve can be calculated by taking the derivative with respect to l_{eq} of the total potential energy at equilibrium, equation (3.5), which becomes, considering the Leibniz's rule (3.7)

$$\frac{\partial \mathcal{V}(l_{eq})}{\partial l_{eq}} = B \int\limits_{l_{eq}}^{\bar{l}} \theta'_{eq}(s) \frac{\partial \theta'_{eq}(s)}{\partial l_{eq}} \mathrm{d}s + P \Bigg[\cos \alpha \int\limits_{l_{eq}}^{\bar{l}} \sin \theta_{eq}(s) \frac{\partial \theta_{eq}(s)}{\partial l_{eq}} \mathrm{d}s$$

$$- \sin \alpha \int\limits_{l_{eq}}^{\bar{l}} \cos \theta_{eq}(s) \frac{\partial \theta_{eq}(s)}{\partial l_{eq}} \mathrm{d}s \Bigg] - P \cos \alpha - B \frac{[\theta'_{eq}(l_{eq})]^2}{2} - S.$$

(3.8)

In particular, keeping into account integration by parts

$$\theta'_{eq} \frac{\partial \theta'_{eq}}{\partial l_{eq}} = \left(\theta'_{eq} \frac{\partial \theta_{eq}}{\partial l_{eq}} \right)' - \theta''_{eq} \frac{\partial \theta_{eq}}{\partial l_{eq}},$$

(3.9)

the equilibrium of the elastica

$$B\theta''_{eq}(s) + P\left[\cos\alpha\sin\theta_{eq}(s) + \sin\alpha\cos\theta_{eq}(s)\right] = 0, \qquad s \in [l_{eq}, \bar{l}] \quad (3.10)$$

and the boundary condition $\theta'_{eq}(\bar{l}) = 0$, we arrive at the following expression for the Eshelby force

$$-\frac{\partial\mathcal{V}(l_{eq})}{\partial l_{eq}} = B\frac{[\theta'_{eq}(l_{eq})]^2}{2} + B\theta'_{eq}(l_{eq})\left.\frac{\partial\theta_{eq}}{\partial l_{eq}}\right|_{s=l_{eq}} + P\cos\alpha + S. \quad (3.11)$$

The fact that θ_{eq} is a function of $s - l_{eq}$ and of the angle of rotation of the beam at the loaded end $\theta_{\bar{l}}$ (function itself of l_{eq}) yields

$$\left.\frac{\partial\theta_{eq}}{\partial l_{eq}}\right|_{s=l_{eq}} = -\left.\frac{\partial\theta_{eq}}{\partial s}\right|_{s=l_{eq}} + \left.\frac{\partial\theta_{eq}}{\partial\theta_{\bar{l}}}\frac{\partial\theta_{\bar{l}}}{\partial l_{eq}}\right|_{s=l_{eq}}. \quad (3.12)$$

Since θ_{eq} is always zero at $s = l_{eq}$ for all $\theta_{\bar{l}}$, the second term in the right-hand side of equation (3.12) is null and that equation becomes

$$\left.\frac{\partial\theta_{eq}}{\partial l_{eq}}\right|_{s=l_{eq}} = -\theta'_{eq}(l_{eq}), \quad (3.13)$$

so that the vanishing of the derivative with respect to l_{eq} of the total potential energy, equation (3.11), represents the axial equilibrium

$$\underbrace{\frac{M^2}{2B}}_{\text{Eshelby-like force}} = S + P\cos\alpha, \quad (3.14)$$

where $M = B\theta'_{eq}(l_{eq})$ is the reaction moment, equal to Pe, where e is the load eccentricity (to the sliding sleeve).

Note that the presence of the Eshelby-like force can be obtained in a simpler but indisputable way also starting from the total potential energy of the same system with $\alpha = 90°$, assuming a linear behaviour, so that at equilibrium is written as

$$\mathcal{V}_{lin}(l_{eq}) = -\frac{P^2(\bar{l} - l_{eq})^3}{6B} - Sl_{eq}, \quad (3.15)$$

and the negative derivative respect to the free parameter l_{eq} brings to

$$-\frac{\partial\mathcal{V}_{lin}(l_{eq})}{\partial l_{eq}} = -\frac{P^2(\bar{l} - l_{eq})^2}{2B} + S, \quad (3.16)$$

which must be set equal to zero at equilibrium, so that the Eshelby-like force in small displacement is exactly the same as equation (3.14), since $P\cos\alpha = 0$,

$$\underbrace{\frac{M^2}{2B}}_{\text{Eshelby-like force}} = S, \quad (3.17)$$

48

where M is the reaction moment at the constraint, namely $P(\bar{l} - l_{eq})$.

Although the Eshelby force must vanish at equilibrium, the contribution $M^2/(2B)$ is a 'counterintuitive term' which depends on the configurational parameter l_{eq} (and would be absent if the elastic rod would be constrained with a movable clamp instead than a sliding sleeve) and is for this reason indicated as the 'Eshelby-like force'.

This term has wrongly been neglected by a number of authors who have considered sliding sleeve constraints, while a term $M^2/(2B)$ correctly enters in calculations referred in a different context, namely, adhesion mechanics, in which it is equated to an 'adhesion energy' (Majidi [40]; Majidi et al. [41] and He et al. [42]).

Since equilibrium is only possible when equation (3.14) is satisfied, the presence of the Eshelby-like force (parallel to the direction of sliding) explains the reason why the equilibrium is possible for the configuration shown in the central photo in Fig. 3.2 and why the rod is 'expelled' from the sliding sleeve in the lower photo.

In the next sections the existence of the Eshelby-like force (3.14) will be demonstrated via two different and independent approaches (an asymptotic method and a variational technique).

3.1.1 Asymptotic approach

The Eshelbian force (3.14) can be obtained via an asymptotic approach. This has been found in a forgotten article published in Russian by Balabukh et al. [43]. The main idea is to consider an imperfect sliding sleeve (Fig. 3.3 having a small gap Δ (the distance between the two rigid, frictionless and parallel surfaces realizing the sliding device), so that the perfect sliding sleeve case is recovered when the gap is null, $\Delta = 0$. Within this space, the elastic rod is deflected, so that $\vartheta(\Delta)$ denotes the angle at its right contact point, where the forces H, V, M are applied. The length of the rod detached from the two surfaces representing the imperfect sliding sleeve is denoted with $a(\Delta)$. The frictionless contact generates the reaction forces R and Q, in equilibrium with the axial dead force S at the other end. For small Δ, the equilibrium is given by

$$Q = \frac{M}{a(\Delta)}, \qquad R = V + \frac{M}{a(\Delta)}, \qquad S = \left(V + \frac{M}{a(\Delta)}\right)\vartheta(\Delta) - H. \quad (3.18)$$

On application of the virtual work for a linear elastic inextensible rod yields the geometric quantities $a(\Delta)$ and $\vartheta(\Delta)$

$$a(\Delta) = \sqrt{\frac{6B\Delta}{M}}, \qquad \vartheta(\Delta) = \frac{1}{2}\sqrt{\frac{6M\Delta}{B}}, \qquad (3.19)$$
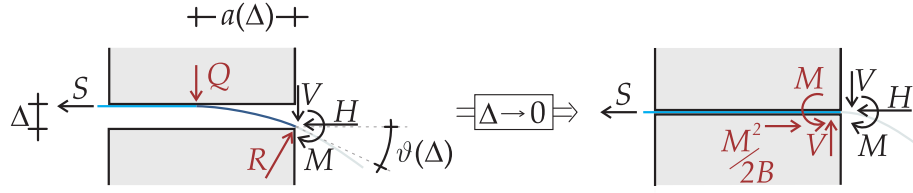
Figure 3.3: Deformed configuration of an elastic rod within an imperfect sliding sleeve made up of two smooth, rigid and frictionless planes placed at a distance Δ. Applied and reaction forces (left) and values obtained in the limit $\Delta \to 0$, revealing the Eshelbian force (right).

so that forces Q, R and S can be written as

$$Q = M\sqrt{\frac{M}{6B\Delta}}, \qquad R = V + M\sqrt{\frac{M}{6B\Delta}}, \qquad S = \frac{M^2}{2B} + \frac{V}{2}\sqrt{\frac{6M\Delta}{B}} - H. \tag{3.20}$$

In the limit of perfect (zero-thickness) sliding sleeve, $\Delta \to 0$, the horizontal component of the reaction R *does not vanish*, but becomes the Eshelbian force (3.14)

$$\lim_{\Delta \to 0} R(\Delta)\vartheta(\Delta) = \frac{M^2}{2B}. \tag{3.21}$$

3.1.2   Variational approach

The total potential energy (3.4) has a movable boundary l_{in}, so that it is expedient (Courant and Hilbert [44], see also Majidi et al. [41]) to introduce a small parameter ϵ and take variations (subscript 'var') of an equilibrium configuration (subscript 'eq') in the form

$$\theta(s, \epsilon) = \theta_{eq}(s) + \epsilon\theta_{var}(s), \qquad l_{in}(\epsilon) = l_{eq} + \epsilon l_{var}, \tag{3.22}$$

with the boundary conditions

$$\theta_{eq}(l_{eq}) = 0, \quad \theta(l_{eq} + \epsilon l_{var}) = 0, \quad \theta'_{eq}(\bar{l}) = 0. \tag{3.23}$$

A Taylor series expansion of $\theta(l_{in})$ for small ϵ yields

$$\begin{aligned} \theta(l_{eq} + \epsilon l_{var}, \epsilon) = \theta_{eq}(l_{eq}) + \epsilon\left(\theta_{var}(l_{eq}) + \theta'_{eq}(l_{eq})l_{var}\right) \\ + \frac{\epsilon^2}{2}l_{var}\left(2\theta'_{var}(l_{eq}) + \theta''_{eq}(l_{eq})l_{var}\right) + \mathcal{O}\left(\epsilon^3\right), \end{aligned} \tag{3.24}$$

so that the boundary conditions (3.23) lead to the following compatibility equations

$$\theta_{var}(l_{eq}) + \theta'_{eq}(l_{eq})l_{var} = 0, \quad 2\theta'_{var}(l_{eq}) + \theta''_{eq}(l_{eq})l_{var} = 0. \tag{3.25}$$

Taking into account the Leibniz rule of differentiation and the boundary (3.23) and compatibility (3.25) conditions, through integration by parts, the first variation of the functional $\mathcal{V}$ is

$$
\delta_\epsilon \mathcal{V} = -\int_{l_{eq}}^{\bar{l}} \left[B\theta_{eq}''(s) + P\left(\cos\alpha\sin\theta_{eq}(s) + \sin\alpha\cos\theta_{eq}(s)\right) \right] \theta_{var}(s)\mathrm{d}s
$$
$$
+ \left[B\frac{\theta_{eq}'(l_{eq})^2}{2} - P\cos\alpha - S \right] l_{var},
$$

(3.26)

so that the equilibrium equations (3.10) and (3.14) are obtained, the latter of which, representing the so-called 'transversality condition' of Courant and Hilbert [44], provides the Eshelby-like force.

3.1.3 The Eshelby-like force expressed as a function of the transversal load

The equilibrium configuration of the elastic rod satisfies the elastica equation (3.10) (see Love [15], and Bigoni [13]), that introducing the auxiliary angle $\varphi(s) = \theta_{eq}(s) + \alpha$ and the normalized load $\lambda^2 = P/B$ writes as

$$
\varphi''(s) + \lambda^2 \sin\varphi(s) = 0, \qquad s \in [l_{eq}, \bar{l}] \tag{3.27}
$$

subject to the boundary conditions $\varphi(l_{eq}) = \alpha$ and $\varphi'(\bar{l}) = 0$. Integration of equation (3.27) yields

$$
\varphi'(s) = \pm\lambda\sqrt{2\left[\cos\varphi(s) - \cos(\theta_{\bar{l}} + \alpha)\right]}, \tag{3.28}
$$

taken in the following with the '+' sign, so that introducing the change of variable

$$
\eta = \sin\frac{\theta_{\bar{l}} + \alpha}{2}, \qquad \eta\sin\phi(s) = \sin\frac{\varphi(s)}{2}, \tag{3.29}
$$

where $\theta_{\bar{l}} = \theta_{eq}(\bar{l})$ representing the rotation measured at the free end of the rod, we end up with the following differential problem

$$
\phi'(s) = \lambda\sqrt{1 - \eta^2 \sin^2\phi(s)} \tag{3.30}
$$

subject to $\phi(l_{eq}) = m = \arcsin\left[\sin(\alpha/2)/\eta\right]$ and $\phi(\bar{l}) = \pi/2$.

Restricting the attention only to the first (stable) mode of deformation, the integration of (3.30) leads to the relation between the rotation measured at the free end of the rod $\theta_{\bar{l}}$ and the applied vertical load

$$
P = \frac{B}{(\bar{l} - l_{eq})^2}\left[\mathcal{K}(\eta) - \mathcal{K}(m, \eta)\right]^2, \tag{3.31}
$$

where $\mathcal{K}(\eta)$ is complete elliptic integral of the first kind, whereas $\mathcal{K}(m, \eta)$ is the incomplete elliptic integral of the first kind. Moreover, through the integration of (3.30) and the implemented change of variable, the rotation field (for the first mode) can be obtained as

$$\theta_{eq}(s) = 2 \arcsin \left[\eta \operatorname{sn} \left((s - l_{eq}) \sqrt{\frac{P}{B}} + \mathcal{K}(m, \eta), \eta \right) \right] - \alpha, \qquad (3.32)$$

where sn is the Jacobi sine amplitude function.

The Eshelby-like force (3.14) can be expressed, taking into account equation (3.28), as

$$\frac{M^2}{2B} = 2P \left(\eta^2 - \sin^2 \frac{\alpha}{2} \right), \qquad (3.33)$$

so that the axial force S at the end of the sliding sleeve, which will be measured through a load cell in the experiments, is given by equation (3.2). It can be noted from equation (3.2) that the measured load S is (in modulus) bounded by P and that S tends to P only in the 'membrane limit', when B tends to zero and $\theta_{\bar{l}} + \alpha$ to π.

The following three different cases may arise, explaining the experiments shown in Fig. 3.2.

(i.) the elastic rod within the sliding sleeve is in compression, or 'pushed in', if $\theta_{\bar{l}} + \alpha < \pi/2$;

(ii.) the elastic rod within the sliding sleeve is unloaded if $\theta_{\bar{l}} + \alpha = \pi/2$;

(iii.) the elastic rod within the sliding sleeve is in tension, or 'pulled out', if $\theta_{\bar{l}} + \alpha > \pi/2$.

The case of null axial force, $S = 0$, occurs when $M^2/(2B)$ is equal to the axial component of the dead load, $P \cos \alpha$, and corresponds to deformed configurations which have the tangent at the free end orthogonal to the direction of the dead load P, as in Fig. 3.2 (center).

Finally, it can be noted that the Eshelby-like force $M^2/(2B)$ is greater than the applied load P when

$$\cos \alpha - 2 \cos^2 \left(\frac{\theta_{\bar{l}} + \alpha}{2} \right) > 0. \qquad (3.34)$$

Regions in the $\theta_{\bar{l}} - \alpha$ plane where the axial force S is positive/negative and where $M^2/(2B) > P$ are shown in Fig. 3.4. From the figure it can be concluded that $M^2/(2B) > P$ is possible only for positive axial load, $S > 0$, and high deflections of the rod (at least for rotation at the free end $\theta_{\bar{l}}$ greater than $\pi/3$ and depending on α).
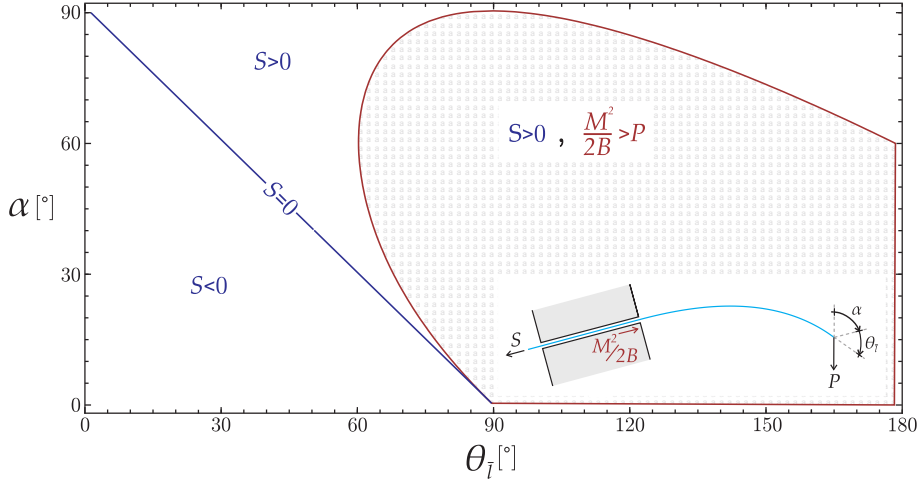
Figure 3.4: Regions in the plane $\theta_{\bar{l}} - \alpha$ where $S > 0$, $S < 0$ and $M^2/(2B) > P$.

3.2 The experimental evidence of configurational force

The structure shown in Fig. 3.1 has been realized using for the elastic rod two C62 carbon-steel strips (25 mm × 2 mm cross section), one 585 mm in length and the other 800 mm. For these rods the bending stiffness B has been determined with flexure experiments to be equal to 2.70 Nm².

The sliding sleeve is 384 mm in length and has been realized with 32 pairs of rollers (made up of 10 mm diameter and 15 mm length teflon cylinders, each containing two roller bearings). The tolerance between the metal strip and the rollers is calibrated with four micrometrical screws.

The axial force S has been measured using a MT1041 load cell (R.C. 300N), while dead loading, measured through a Leane XFTC301 (R.C. 500N) loading cell, has been provided with a simple hydraulic device in which water is poured at constant rate of 10 gr/s into a container. Data have been acquired with a NI CompactDAQ system, interfaced with Labview 8.5.1 (National Instruments). The whole apparatus has been mounted on an optical table (1HT-NM from Standa) to prevent spurious vibrations, which have been checked to remain negligible (accelerations have been found inferior to 2×10^{-3} g) with four IEPE accelerometer (PCB Piezotronics Inc., model 333B50) attached at different positions. The tests have been performed in a controlled temperature (20±0.2 °C) and humidity (48±0.5%) room. The testing set-up is shown in Fig. 3.5.
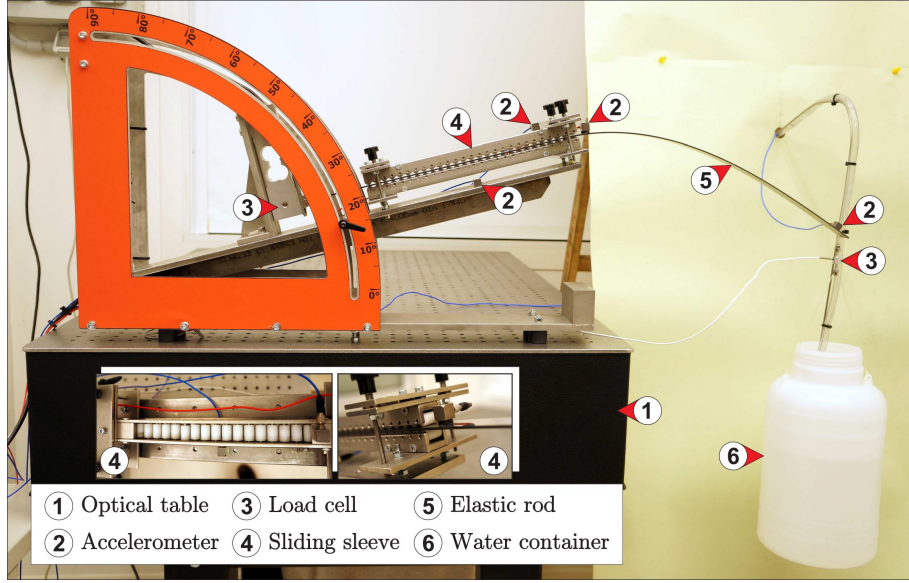
Figure 3.5: The test setup for the measure of the axial Eshelby-like force transmitted by a sliding sleeve, a realization of the scheme reported in Fig. 3.1.

3.2.1   Eshelbian force provided by a roller device

Rollers have been employed in the practical realization of the sliding sleeve, so that the question may arise how this set-up is tight to our idealization and can effectively measure the Eshelby-like force. To quantify the effects introduced by the rollers, an asymptotic approach similar to that presented in Section 3.1.1 is developed here by considering the statically determined system given by two rollers with finite radius r and which centers are distant $\Delta_H + 2r$ and $\Delta_V + 2r$ in the axial and transversal directions, so that the model of a perfect sliding sleeve is achieved in the limit of null value for these three parameters (r, Δ_H and Δ_V), Fig. 3.6. In the limit $\Delta_V/\Delta_H \to 0$, the roller reactions X and Y are obtained from rotational and translational (in the transversal direction) equilibrium as

$$X = \frac{M}{\cos \xi \left[\Delta_H + r \left(2 + \sin \psi + \sin \xi\right)\right]},$$
$$Y = \frac{1}{\cos \psi} \left[V + \frac{M}{\Delta_H + r \left(2 + \sin \psi + \sin \xi\right)}\right], \quad (3.35)$$

where ξ and ψ are the rotations of the rod at the contact points with the rollers, so that the translational (in the axial direction) equilibrium leads to

$$S = V \tan \psi - \frac{M \left(\tan \xi - \tan \psi\right)}{\Delta_H + r \left(2 + \sin \psi + \sin \xi\right)} - H. \quad (3.36)$$

Restricting attention to small deflections between the rollers, the Euler-Bernoulli beam theory describes the relationship between the beam's curvature
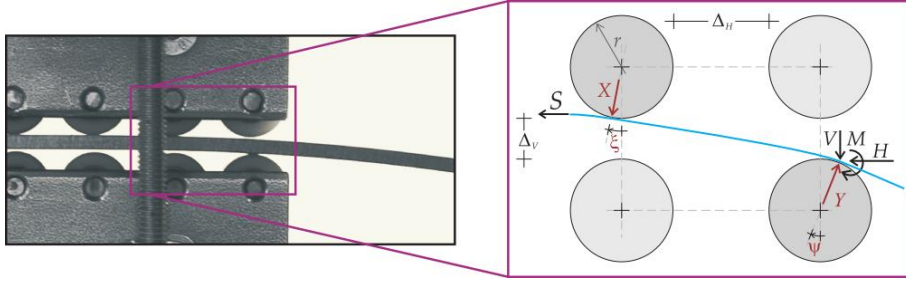
Figure 3.6: Left: the practical realization of the sliding sleeve constraint realized through pairs of rollers and (right) its scheme where only the first two pairs of rollers are considered because after those the rod is in the rectilinear configuration (see the left image).

$v''(z)$ and the applied moment $M(z)$ as

$$Bv''(z) = Xz \cos\xi, \tag{3.37}$$

where z is the longitudinal coordinate of the beam axis. The angles ξ and ψ can be obtained through double integration of the elastica (3.37), subject to the boundary conditions

$$v(0) = 0, \qquad v(\Delta_H + 2r + r\sin\psi + r\sin\xi)) = \Delta_V + r(2 - \cos\psi + \cos\xi),$$

$$v'(0) = \xi, \qquad v'(\Delta_H + 2r + r\sin\psi + r\sin\xi)) = \psi, \tag{3.38}$$

as

$$\xi = -\frac{M(\Delta_H + 2r)^2(2B + Mr) + 6B(-2B + Mr)\Delta_V}{2B(\Delta_H + 2r)(6B + Mr)},$$

$$\psi = \frac{M(\Delta_H + 2r)^2(4B + Mr) + 6B(2B + Mr)\Delta_V}{2B(\Delta_H + 2r)(6B + Mr)}. \tag{3.39}$$

In the limit of $\Delta_V/r \to 0$, equation (3.39) simplifies to

$$\xi = -\frac{M(\Delta_H + 2r)(Mr + 4B)}{2B(Mr + 6B)}, \quad \psi = -\xi, \tag{3.40}$$

and the translational equilibrium, equation (3.36), reads

$$\underbrace{\frac{M}{6B + Mr}\left[\frac{6M(3B + Mr)}{6B + Mr} + \frac{V(\Delta_H + 2r)(4B + Mr)}{2B}\right]}_{\text{Eshelby-like force}} = S + H, \tag{3.41}$$

an equation which introduces the concept of Eshelby-like force provided by a roller device, and reducing in the limits $r \to 0$ and $\Delta_H \to 0$ to the value of the Eshelby-like force 3.14 arising from a sliding sleeve.

It can be noted that the lowest value of the configurational force realized by the roller device occurs in the limit of the sliding sleeve.

3.2.2 Experiments

Results of experiments are reported in Fig. 3.7 and compared with the theoretical predictions obtained with the 'perfect model' of sliding sleeve, equation 3.14, and with the 'roller-version' of it, equation (3.41), the latter used with parameters tailored on the experimental set up ($r = 5$ mm, $\Delta_H = 1$ mm).

First of all, we can note that the theoretical values are close to each other, which is a proof that the rollers have a negligible effect on the determination of the Eshelby-like force. Moreover, we see that there is an excellent agreement between the theoretical predictions and the experimental results, which is an indisputable proof that Eshelby-like forces acting on elastic structures are a reality.

At http://ssmg.unitn.it/eshelbylikeforce.html can be found movies of the experiments.

The findings presented in this chapter demonstrate that movable constraints applied to elastic structures can generate configurational forces and that these become dominant when deformations are sufficiently large. Configurational forces can be employed in the design of new deformable systems with challenging characteristics, which may find applications even at the micro- and nano-scale, for instance, to control growth of a structural element.
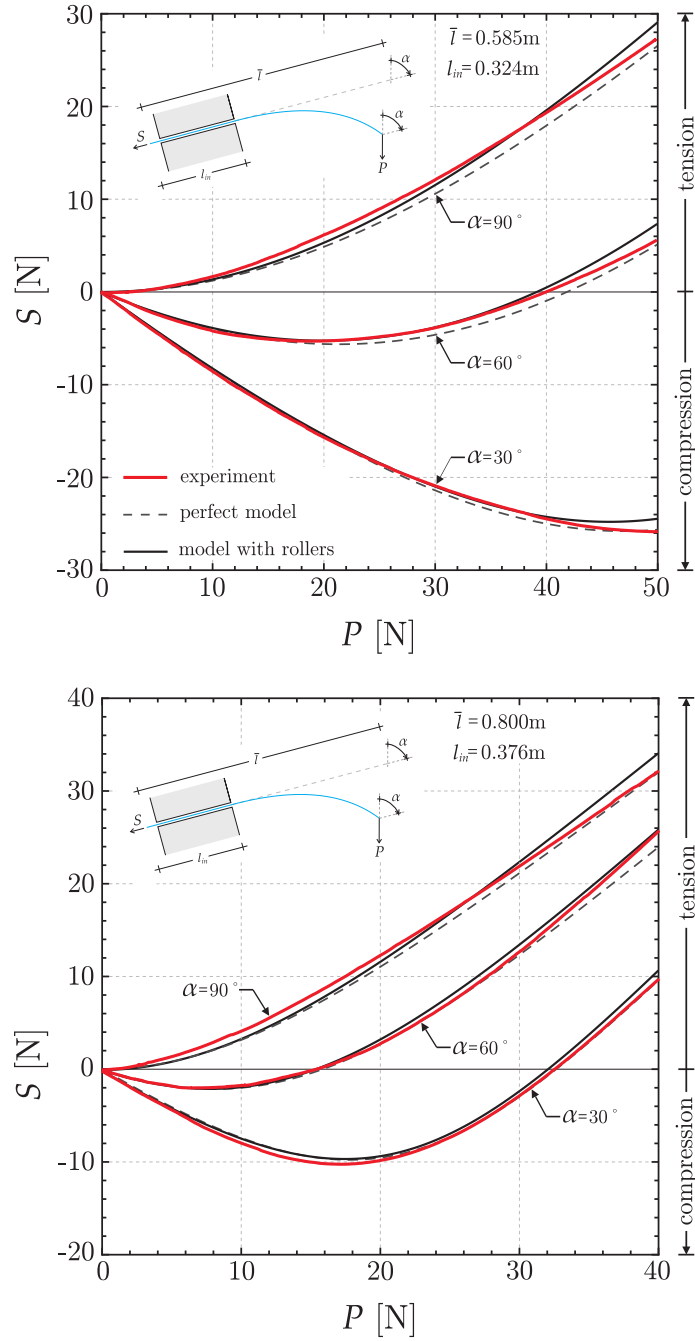
Figure 3.7: Comparison between experimental results (red curve) and the theoretical predictions. These have been reported for a perfect sliding sleeve (dashed curve) and for a sliding sleeve realized with rollers mimicking the experimental conditions (solid curve). Two rods have been used of external lengths 261 mm (upper) and 424 mm (lower) for different inclinations (90°, 60° and 30°).

Chapter 4

The influence of Eshelby-like force on structures with variable length

The fact that an elastic rod may change its length during deformation introduces the possibility that configurational forces develop and influence the mechanical response. This is indeed the case of two structures analyzed in the present chapter, where configurational forces are of chief importance and introduce a reversal in the load/deflection diagram. These structures are important for several applications, including for instance artery insertion of a guide wire, or wellbore insertion of a steel pipe. Experiments on model structures specifically designed, manufactured and tested, fully confirm the strong effect of the configurational forces.

The buckling of a piece of paper hitting an obstacle during ejection from a printer, the insertion of a catheter (or a steel piping) in an artery (in a wellbore), and the so-called 'inverse spaghetti problem' are all but examples of mechanical settings where an elastic rod of variable length is involved. Usually, the rod is ejected through a sliding sleeve and this produces a configurational or Eshelby-like force (see Chapter 3 or [9]), which has been until now neglected [45–48]. The aim of this chapter is to provide direct theoretical and experimental evidence that the effect of configurational forces is dominant and cannot be neglected. In particular, it leads to force reversals that otherwise would not exist.

The setup considered here is an elastic rod of bending stiffness B, clamped on the left edge and inserted into a frictionless and bilateral sliding sleeve on the right end, at a distance L. Two loading conditions are investigated: (i.) the elastic rod is loaded axially, so that it has to buckle to deflect, and (ii.) transversely with a bi-lateral roller acting at the mid-span of the rod (along a symmetry axis), see Fig. 4.1. These problems have been already considered in [45–48], but neglecting configurational forces and without
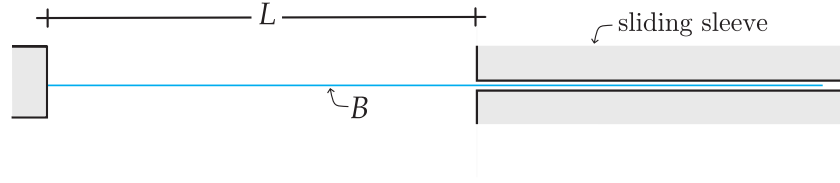
Figure 4.1: An elastic planar rod of bending stiffness B is restrained by a clamp in its left-hand side, while, at a distance L, a frictionless sleeve is attached. This constraint allows the sliding of the rod, so that it may change its length once loaded.

experimental validation (which would have revealed a strong discrepancy between theoretical predictions and experiments).

The elastic systems (i.) and (ii.) are analytically solved through integration of the elastica ([13, 15]). It is shown that in both systems 'Eshelby-like' forces strongly influence the loading paths and yield surprising force reversals, so that certain equilibrium configurations are possible if and only if the applied force changes its sign.

4.1 Structure with an end thrust

With reference to the structural system reported in Fig. 4.2 (left), introducing the curvilinear coordinate $s \in [0, l_{\text{out}}]$, where $l_{\text{out}} > L$ is the length of the deformed elastic planar rod between the two constraints (clamp and sliding sleeve), and the rotational field $\theta(s)$ of the rod's axis and denoting by a prime the derivative with respect to s, the governing equation of the elastica, together with its boundary conditions, is [1]

$$\theta''(s) + \rho^2 \sin\theta(s) = 0, \qquad s \in [0, l_{\text{out}}]$$

$$\theta(0) = \theta(l_{\text{out}}) = 0,$$

$$\int_0^{l_{\text{out}}} \sin\theta(s)\mathrm{d}s = 0, \qquad \int_0^{l_{\text{out}}} \cos\theta(s)\mathrm{d}s = L, \tag{4.2}$$

---

[1] Equilibrium equations and the existence of the Eshelby-like force can be obtained starting from the total potential energy, as done in Section 3.1, introducing the small parameter ϵ and taking the variation of $\theta(s, \epsilon)$ and $l_{\text{out}}(\epsilon)$, since it is a movable boundary. For conciseness only the expression of the total potential energy is reported here as

$$\mathcal{V}(\theta(s), l_{\text{out}}) = B \int_0^{l_{\text{out}}} \frac{[\theta'(s)]^2}{2}\mathrm{d}s + P \int_0^{\tilde{L}} \cos\theta(s)\mathrm{d}s + Z \left[L - \int_0^{l_{\text{out}}} \cos\theta(s)\mathrm{d}s \right], \tag{4.1}$$

where $\tilde{L}$ is the total length of the rod where the thrust is applied, and Z is a Lagrangian multiplier.

where $\rho^2 = \bar{P}/B$ and $\bar{P}$ is the sum of the load P and the Eshelby-like force acting in the same direction of the thrust, generated by the release mechanism of flexural energy through the sliding sleeve. The configurational force can be determined in different ways through derivative, variational or asymptotic approach (see Section 3.1), as

$$\frac{M^2(l_{\text{out}})}{2B} = B\frac{\theta'(l_{\text{out}})^2}{2}. \tag{4.3}$$
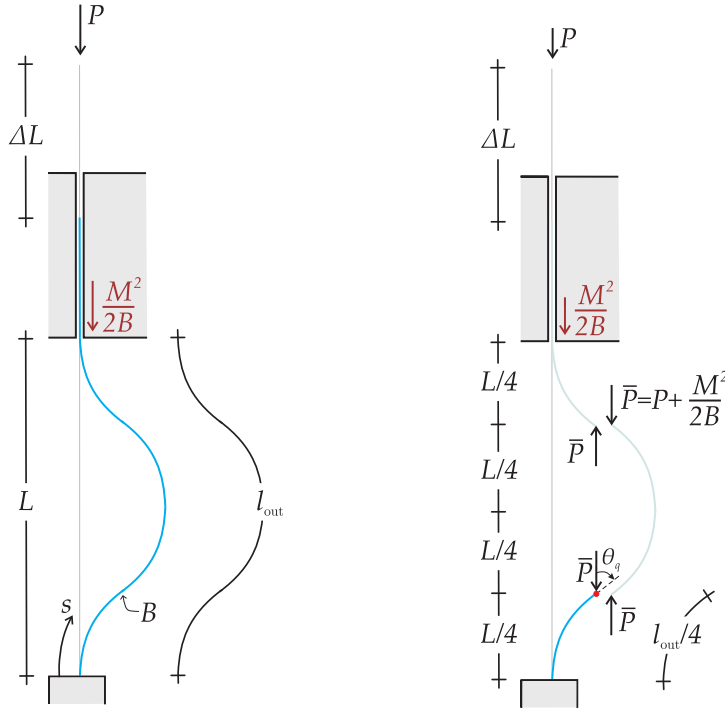
Figure 4.2: Left: the design scheme employed to realize the structure shown in Fig. 4.1 loaded with an end thrust and right: the structure as it will be analyzed through symmetry properties, dividing it into four equal cantilever beams of length l_{out}; the first cantilever has its end points that lies at a vertical coordinate of $L/4$ with respect to the clamp and it is loaded with a dead load $\bar{P} = P + M^2/2B$. Note that the structure has been rotated of $90°$ in order to simplify its experimental design, Fig. 4.4.

Since only the first mode of bifurcation will be taken into account, thanks to the symmetry properties, the Eshelby-like force may be written also as

$$\frac{M^2(0)}{2B} = B\frac{\theta'(0)^2}{2}, \tag{4.4}$$

so that the load parameter ρ becomes

$$\rho = \sqrt{\frac{\bar{P}}{B}} = \sqrt{\frac{P}{B} + \frac{\theta'(0)^2}{2}}. \tag{4.5}$$

61

In order to facilitate the analytical description, the symmetry properties can be exploited, so that the investigation of the system is simplified in the analysis of one of the four clamped rod of equal length $l_{\text{out}}/4$ subjected to an end thrust, Fig. 4.2 (right), equation (4.4). Similarly to the analysis of symmetric buckling modes for the doubly clamped elstica, Section 2.2.3, the relation between the load parameter ρ and the rotation measured at the free end of the cantilever $\theta\left(s = l_{\text{out}}/4\right) = \theta_q$ (a quarter of the total deformed length of the elastic beam) is [2]

$$\rho\, l_{\text{out}} = 4\mathcal{K}\left(\upsilon\right), \tag{4.7}$$

where the kinematic parameter θ_q has been inserted in the change of variable necessary for the solution of the differential problem (4.2)

$$\upsilon = \sin\frac{\theta_q}{2}. \tag{4.8}$$

The configurational force, included in ρ, is a function of the curvature at the clamped end of the rod $\theta'(0)$ $(\theta'(l_{out}))$ which can be obtained, through a multiplication of equation $(4.2)_1$ by θ' and its integration, together with the boundary condition $\theta\left(s = l_{\text{out}/4}\right) = \theta_q$ as

$$\theta'(0) = \sqrt{2\rho^2(1 - \cos\theta_q)} = 2\rho\upsilon, \tag{4.9}$$

so that equation (4.5) may be rewritten as

$$\rho = \sqrt{\frac{P}{B} + 2\rho^2\upsilon^2} \qquad \Leftrightarrow \qquad \frac{P}{B} = \rho^2\left(1 - 2\upsilon^2\right). \tag{4.10}$$

Similarly to Section 3.1.3, it is possible to write the rotational field $\theta(s)$ for the cantilever $s \in [0; l_{\text{out}}/4]$

$$\theta(s) = 2\arcsin\left(\upsilon\,\text{sn}\left(s\rho, \upsilon\right)\right), \tag{4.11}$$

as weel as the axial and transverse equations describing the shape of the elastica [3]

$$x_1(s) = -s + \frac{2}{\rho}\left\{E\left[\text{am}\left(s\rho, \upsilon\right), \upsilon\right]\right\},$$

$$x_2(s) = \frac{2\upsilon}{\rho}\left[1 - \text{cn}(s\rho)\right], \tag{4.12}$$

---

[2]The incorrect solution in which the Eshelby-like force is neglected ican be written as

$$\sqrt{\frac{P}{B}}\, l_{\text{out}} = 4\mathcal{K}\left(\upsilon\right). \tag{4.6}$$

yielding the curve reported in Fig. 4.3 together with the correct presented solution.

[3]Equations (4.11) and (4.12) are valid for the entire structure $s \in [0; l_{\text{out}}]$

where the functions am, cn and sn denote respectively the Jacobi amplitude, Jacobi cosine amplitude and Jacobi sine amplitude functions, while $E(x, v)$ is the incomplete elliptic integral of the second kind of modulus v.

Although the problem under consideration seems to be fully determined by equations (4.7), (4.11) and (4.12), the length $l_{\text{out}}/4$ of the cantilever's reference configuration (and therefore the length l_{out} of the entire rod) is still unknown because it is changing since the elastic rod can slide out from the sliding sleeve due to the applied thrust. This difficulty can be overcome taking advantage of symmetry properties of the system, because the axial displacement of the cantilever, for every unknown length $l_{\text{out}}/4$ of it, is $x_1(s = l_{\text{out}}/4) = L/4$, so that, equation (4.12)$_1$ gives

$$-\frac{l_{\text{out}}}{4} + \frac{2}{\rho}\left\{E\left[\text{am}\left(\frac{l_{\text{out}}}{4}\rho, v\right), v\right]\right\} = \frac{L}{4}, \tag{4.13}$$

and therefore, inserting equation (4.7) in (4.13) it is possible to arrive at the relation between the load parameter ρ and the angle of rotation at the free edge of the cantilever (or at a quarter of the entire structure) θ_q

$$\rho = \frac{4}{L}\left\{2E\left[\text{am}\left(\mathcal{K}(v), v\right), v\right] - \mathcal{K}(v)\right\}. \tag{4.14}$$

The applied thrust P divided by the Eulerian critical load for the structure $P_{cr} = 4\pi^2 B/L^2$ is calculated from equation (4.10) as a function of the kinematic parameter θ_q through equation (4.8) as

$$\frac{P}{P_{cr}} = \frac{4}{\pi^2}\left\{2E\left[\text{am}\left(\mathcal{K}(v), v\right), v\right] - \mathcal{K}(v)\right\}^2(1 - 2v^2), \tag{4.15}$$

and it is reported in Fig. 4.3 together with the incorrect solution in which the configurational force is neglected, equation (4.6). Even though the critical load does not change between the incorrect and correct solutions, because it is not affected by the curvature at the constraint, it can be noted that the correct solution is considerably different from the other, especially because the unstable postcritical path exhibits a *force reversal* when $\theta_q > 90°$ (see also experiments in Section 4.1.1), which is not predicted by the incorrect solution. Moreover, two different deformed equilibrium configurations exist without any applied load when $\theta_q = 90°$ and $\theta_q \approx 130.71°$.

The dimensionless amount of rod pushed out from the sliding sleeve

$$\frac{\Delta L}{L} = \frac{l_{\text{out}}}{L} - 1 \tag{4.16}$$

can be easily computed from equations (4.7) and (4.14) as a function of the rotation angle θ_q as

$$\frac{\Delta L}{L} = \frac{\mathcal{K}(v)}{2E\left[\text{am}\left(\mathcal{K}(v), v\right), v\right] - \mathcal{K}(v)} - 1, \tag{4.17}$$
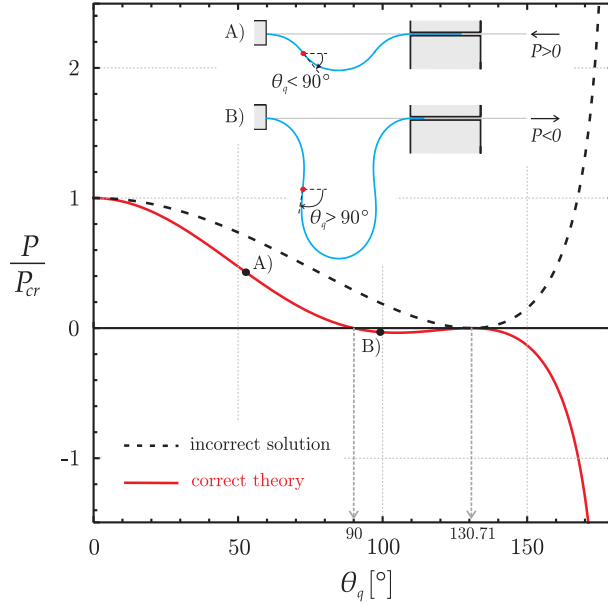
Figure 4.3: Deformation paths of the structure sketched in Fig. 4.2, expressed as the dimensionless applied dead load P/P_{cr} versus the angle of rotation θ_q at the rod's quarter reference length. Correct solution (red curve), equation (4.10), is reported together with the incorrect solution (dashed black curve) in which the Eshelby-like force is neglected, equation (4.6). Two deformed (unstable) equilibrium configurations have been sketched in the inset showing that a compressive thrust (A) or tensile load (B) are necessary to guarantee equilibrium for $\theta_q < 90°$ and $\theta_q > 90°$ respectively.

whereas the analytical expression of Eshelby-like force (divided by P_{cr}), obtained from equation (4.9), becomes

$$\frac{M^2}{2BP_{cr}} = \frac{8v^2}{\pi^2} \left\{ 2\, E\left[\text{am}\left(\mathcal{K}(v), v\right), v\right] - \mathcal{K}(v) \right\}^2 . \tag{4.18}$$

4.1.1 Experimental

With the purpose of verify theoretical findings, experiments have been realized on the model structure reported in Fig. 4.4, designed and realized at the Instabilities Lab of University of Trento (http://ssmg.unitn.it/). The displacement has been imposed on the system with loading machine MIDI 10 (Messphysik). During the test the applied axial force P has been recorded using a MT1041 load cell (R.C. 500N) and the displacement ΔL has been registered with the displacement transducer mounted on the testing machine. Data have been acquired with a NI compactRIO system interfaced with Labview 2013 (National Instruments). The elastic rods has been realized in solid polycarbonate strips (white 2099 Makrolon UV from Bayer, elastic
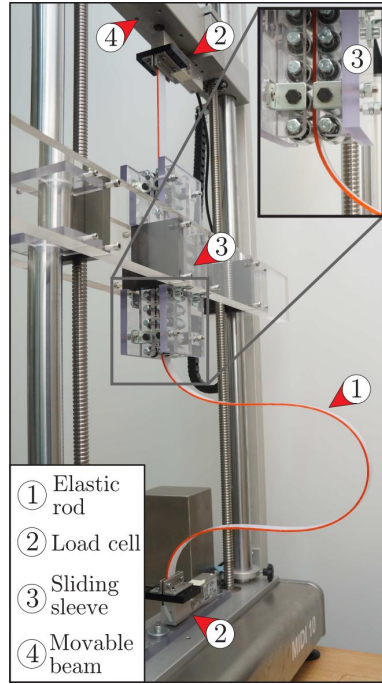
Figure 4.4: The experimental set up realizes the structural scheme reported in Fig. 4.2.

modulus 2350 MPa), with dimensions 650 mm × 24 mm × 2.9 mm The sliding sleeve, 285 mm in length, has been realized by employing 14 pairs of rollers from Misumi Europe (Press-Fit Straight Type, 20 mm in diameter and 25 mm in length), modified to reduce friction. The tolerance between the polycarbonate blades and the rollers is calibrated with four micrometrical screws. This constraint has been fixed to the two columns of the load frame as it is clearly visible in Fig. 4.4. Temperature near the testing machine has been monitored with a thermocouple connected to NI compaqRIO and has been found to lie around 22°C without sensible oscillations during tests.

Experiments are reported in Fig. 4.5 and compared with the theoretical predictions with and without the configurational force. The former prediction in an excellent agreement with experimental results performed for two different distances between the two supports ($L = 360$ mm and $L = 410$ mm), whereas the latter is substantially different, revealing that neglecting the configurational force introduces an important error. The dimensionless applied load P/P_{cr} versus dimensionless additional length $\Delta L/L$ being pushed in through the sliding sleeve shows a force reversal (not present in the incorrect model) when $\Delta L/L \approx 1.19$. Finally, the dimensionless configurational force $M^2/2BP_{cr}$ is measured as a function of $\Delta L/L$, its strong influence on postcritical behaviour, because it may reach more than one-third of the rod's critical load.
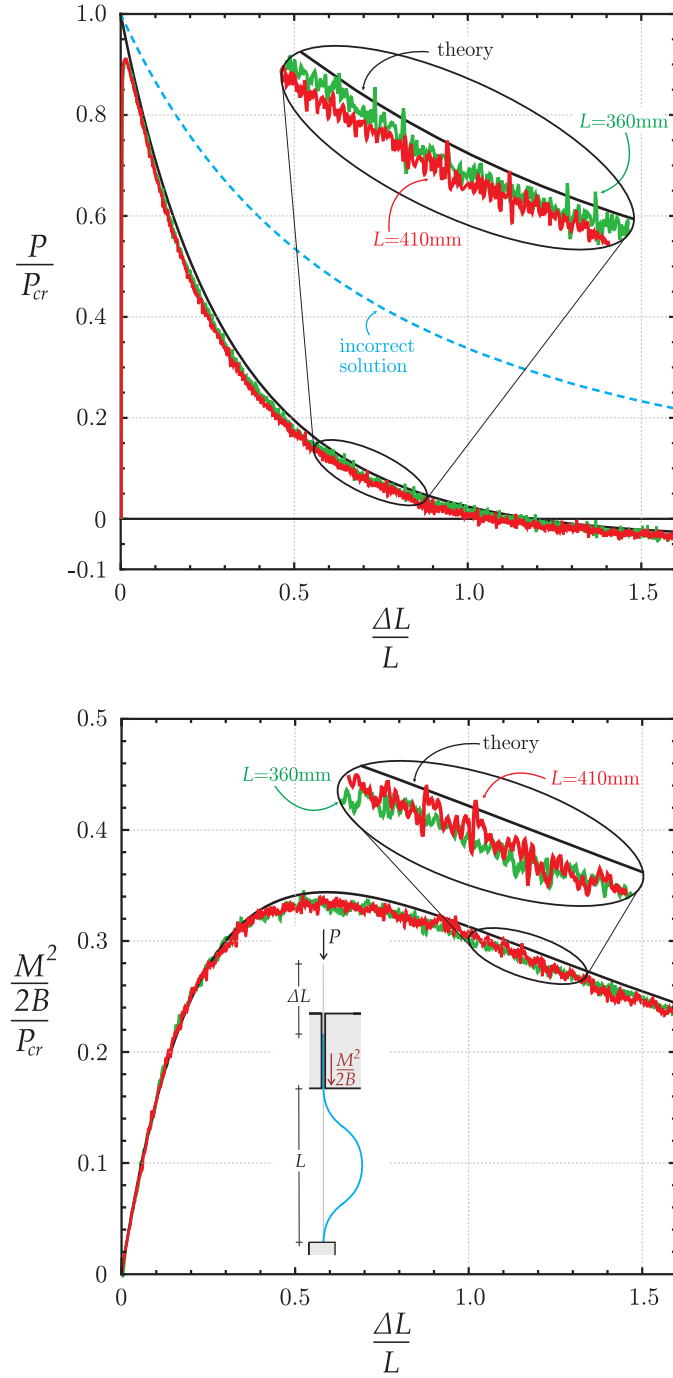
Figure 4.5: Comparison between theoretical predictions (black curve) and experimental results for two different distances $L = 360$ mm (green curve) and $L = 410$ mm (red curve) between the two constraints. Applied dimensionless thrust P/P_{cr} (upper) and dimensionless 'Eshelby-like' force $M^2/2BP_{cr}$ (lower) versus dimensionless additional length $\Delta L/L$ that is pushed out from the sleeve. The postcritical incorrect path obtained without considering the effect of configurational force is reported with a blue dashed curve in the upper graph.
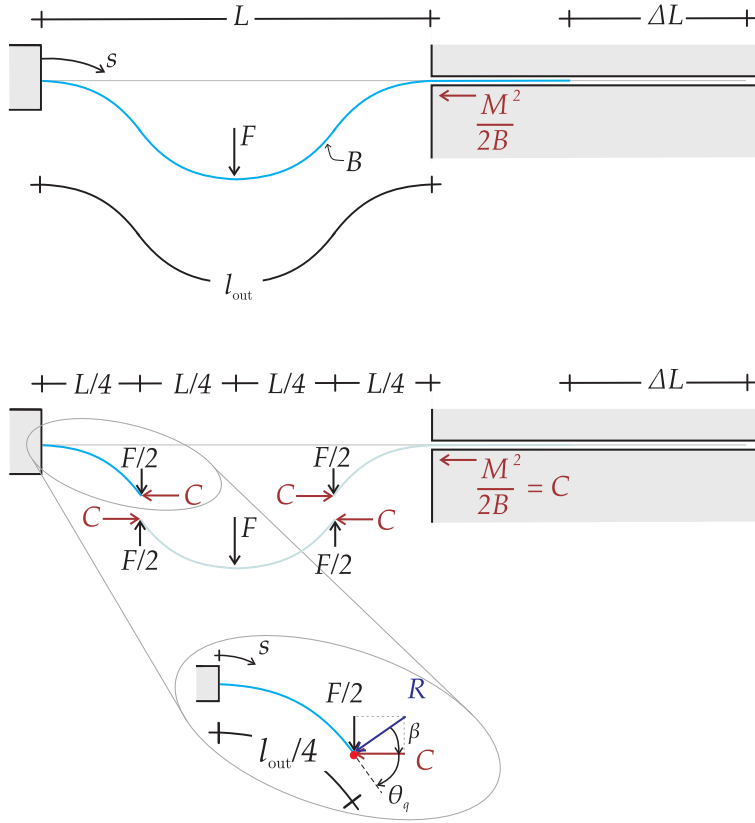
Figure 4.6: Upper: the elastic system loaded with a concentrated transverse force F that generates, during inflection, the Eshelby-like C force acting in the axial direction. Center: the structure, thanks to symmetry properties, will be divided into four equal rods of length $l_{out}/4$ and only one of them (lower), subjected to a transverse load $F/2$ and to the axial load C, will be considered.

4.2 Structure with transverse force

The structure with variable length, reported in Fig. 4.1, subjected to a transverse load at the mid-span, has been analyzed by Humer [45], who did not consider the Eshelby-like force arising from the sliding sleeve and representing an axial variable (because it depends on the bending moment at the two supports) load for the elastic rod. In the following, the solution reported in [45] will be re-analyzed considering the effect of configurational force, which is expressed by equations (4.3) and (4.4).

In particular, with reference to an elastic inextensible planar rod of curvilinear coordinate $s \in [0; l_{out}]$ (with $l_{out} > L$) and rotational field $\theta(s)$, reported in Fig. 4.6 (upper part), symmetric properties allow us to reduce the analysis of the entire structure to the investigation of a quarter cantilever rod of reference length $s = l_{out}/4$, subjected to a tip force, which is one half of the

concentrated force F of the original problem, and an axial thrust, which is exactly the Eshelby-like force $M^2/2B = C$, Fig. 4.6 (lower part). Therefore, the equilibrium configuration of the elastic rod satisfies the elastica and its boundary condition

$$
\begin{aligned}
&B\theta''(s) + \frac{F}{2}\cos\theta(s) + C\sin\theta(s) = 0, \qquad s \in \left[0, \frac{l_{\text{out}}}{4}\right], \\
&\theta(0) = 0, \\
&\theta'\left(\frac{l_{\text{out}}}{4}\right) = 0,
\end{aligned}
\tag{4.19}
$$

Introducing the load parameter

$$
\gamma^2 = \frac{R}{B} = \frac{1}{B}\sqrt{\left(\frac{F}{2}\right)^2 + C^2}
\tag{4.20}
$$

and the auxiliary angle $\psi(s) = \theta(s) + \beta$, where β is the inclination, with respect to the horizontal direction, of the resultant R between $F/2$ and C, the differential problem (4.19) can be rewritten as

$$
\begin{aligned}
&\psi''(s) + \gamma^2\sin\psi(s) = 0, \qquad s \in \left[0, \frac{l_{\text{out}}}{4}\right] \\
&\psi(0) = \beta, \\
&\psi'\left(\frac{l_{\text{out}}}{4}\right) = 0.
\end{aligned}
\tag{4.21}
$$

Since the rotation at the free end of the cantilever has been defined as θ_q (with $\theta_q \in [0; \pi]$), it follows that $\psi(s = l_{\text{out}}/4) = \psi_q = \theta_q + \beta$, so that an integration of $(4.21)_1$ yields

$$
\psi'(s) = \pm\gamma\sqrt{2(\cos\psi(s) - \cos\psi_q)},
\tag{4.22}
$$

taken in the following with the '+' sign. Considering the following change of variables

$$
\eta = \sin\frac{\psi_q}{2}, \qquad \eta\sin\omega(s) = \sin\frac{\psi(s)}{2},
\tag{4.23}
$$

the differential equation (4.22) can be integrated to obtain the relation between the load parameter γ and the angles θ_q and β in the form

$$
\gamma l_{\text{out}} = 4\left[\mathcal{K}(\eta) - \mathcal{K}(\omega_\beta, \eta)\right]
\tag{4.24}
$$

where $\omega_\beta = \arcsin\left(\frac{1}{\eta}\sin\left(\frac{\beta}{2}\right)\right)$ and $\mathcal{K}(\omega_\beta, \eta)$ is the incomplete elliptic integral of the first kind. Equation (4.24) contains the unknown value of

the configurational force C (included in γ) and the length of the rod in its reference configuration $l_{\text{out}}/4$. The former can be calculated through the implemented change of variables as

$$C = B\frac{\theta'(0)^2}{2} = B\frac{\psi'(0)^2}{2} = 2B\gamma^2\left(\eta^2 - \sin^2\frac{\beta}{2}\right), \qquad (4.25)$$

so that equation (4.20) becomes

$$B\gamma^2 = \sqrt{\left(\frac{F}{2}\right)^2 + \left(2B\gamma^2\left(\eta^2 - \sin^2\frac{\beta}{2}\right)\right)^2}, \qquad (4.26)$$

and consequently

$$\frac{F}{B} = \pm 2\gamma^2\sqrt{1 - 4\left(\eta^2 - \sin^2\frac{\beta}{2}\right)^2}. \qquad (4.27)$$

The latter may be solved once the equations describing the shape of the elastica are obtained. In particular, from equation $(4.23)_2$ the rotational field for the cantilever is [4]

$$\theta(s) = 2\arcsin\left[\eta\,\text{sn}\left(\gamma s + \mathcal{K}\left(\omega_\beta, \eta\right), \eta\right)\right] - \beta, \qquad (4.28)$$

while the analytical form for the axial and transverse equations describing the shape of the elastica are calculated from integration of kinematic fields (Section 2.1, see also equation (2.95)) as

$$\begin{aligned}
x_1(s) = {} & +\sin\beta\left[-\frac{2\eta}{\gamma}\text{cn}\left(\gamma s + \mathcal{K}(\omega_\beta, \eta), \eta\right) + \frac{2\eta}{\gamma}\text{cn}\left(\mathcal{K}(\omega_\beta, \eta), \eta\right)\right] \\
& \cos\beta\left\{-s + \frac{2}{\gamma}\left[E\left[\text{am}\left(\gamma s + \mathcal{K}(\omega_\beta, \eta), \eta\right), \eta\right]\right.\right. \\
& \left.\left. - E\left[\text{am}\left(\mathcal{K}(\omega_\beta, \eta), \eta\right), \eta\right]\right]\right\}, \\[6pt]
x_2(s) = {} & \cos\beta\left[-\frac{2\eta}{\gamma}\text{cn}\left(\gamma s + \mathcal{K}(\omega_\beta, \eta), \eta\right) + \frac{2\eta}{\gamma}\text{cn}\left(\mathcal{K}(\omega_\beta, \eta), \eta\right)\right] \\
& -\sin\beta\left\{-s + \frac{2}{\gamma}\left[E\left[\text{am}\left(\gamma s + \mathcal{K}(\omega_\beta, \eta), \eta\right), \eta\right]\right.\right. \\
& \left.\left. - E\left[\text{am}\left(\mathcal{K}(\omega_\beta, \eta), \eta\right), \eta\right]\right]\right\}.
\end{aligned} \qquad (4.29)$$

Employing the same symmetric property described for the system loaded with an end thrust and shown also in Fig. 4.6 (lower part), so that $x_1(l_{\text{out}}/4) = L/4$

---

[4]This equation, together with relation (4.29) holds for the entire rod.

can be written considering equation (4.24) in the form

$$\gamma = \frac{4}{L}\Big\{\cos\beta\Big[\mathcal{K}(\omega_\beta,\eta) - \mathcal{K}(\eta) + 2\big[E\left[\text{am}\left(\mathcal{K}(\eta),\eta\right),\eta\right]$$
$$- E\left[\text{am}\left(\mathcal{K}(\omega_\beta,\eta),\eta\right),\eta\right]\big]\Big] - 2\eta\sin\beta\left[\text{cn}\big(\mathcal{K}(\eta),\eta\big) - \text{cn}\big(\mathcal{K}(\omega_\beta,\eta),\eta\big)\right]\Big\},$$

$$(4.30)$$

so that the relation between the dimensionless applied transverse force $f = FL^2/B$ and the parameters η (which contains θ_q) and β is obtained from equation (4.26) as

$$f = \pm 32\Big\{\cos\beta\Big[\mathcal{K}(\omega_\beta,\eta) - \mathcal{K}(\eta) + 2\big[E\left[\text{am}\left(\mathcal{K}(\eta),\eta\right),\eta\right]$$
$$- E\left[\text{am}\left(\mathcal{K}(\omega_\beta,\eta),\eta\right),\eta\right]\big]\Big] - 2\eta\sin\beta\left[\text{cn}\big(\mathcal{K}(\eta),\eta\big) - \text{cn}\big(\mathcal{K}(\omega_\beta,\eta),\eta\big)\right]\Big\}^2$$
$$\times\sqrt{1 - 4\left(\eta^2 - \sin^2\frac{\beta}{2}\right)^2},$$

$$(4.31)$$

while the dimensionless Eshelby-like force, considering expression (4.25), becomes

$$\frac{CL^2}{B} = 32\left(\eta^2 - \sin^2\frac{\beta}{2}\right)\Big\{\cos\beta\Big[\mathcal{K}(\omega_\beta,\eta) - \mathcal{K}(\eta) + 2\big[E\left[\text{am}\left(\mathcal{K}(\eta),\eta\right),\eta\right]$$
$$- E\left[\text{am}\left(\mathcal{K}(\omega_\beta,\eta),\eta\right),\eta\right]\big]\Big] - 2\eta\sin\beta\big[\text{cn}\big(\mathcal{K}(\eta),\eta\big)$$
$$- \text{cn}\big(\mathcal{K}(\omega_\beta,\eta),\eta\big)\big]\Big\}^2,$$

$$(4.32)$$

where the distance between the two supports is introduced as a characteristic length of the problem. Furthermore, the dimensionless additional length $\Delta L/L$ being pushed in through the sliding sleeve is, according to equations (4.16), (4.24) and (4.30)

$$\frac{\Delta L}{L} = \frac{\mathcal{K}(\eta) - \mathcal{K}(\omega_\beta,\eta)}{\gamma L} - 1. \qquad (4.33)$$

Finally, due to symmetry, the mid-span deflection of the structure is twice the vertical displacement of the free edge of the cantilever $w = x_2(s = l_{\text{out}}/2) = 2x_2(s = l_{\text{out}}/4)$ so that it can be written in the following form

$$w = \frac{1}{\gamma}\Big\{2\eta\cos\beta\cos(\omega_\beta) + \sin\beta\left[2E\left(\omega_\beta,\eta\right) - 2E\left(\eta\right) + \mathcal{K}(\eta) - \mathcal{K}(\omega_\beta,\eta)\right]\Big\},$$

$$(4.34)$$

where γ is defined by (4.30). Equations (4.31), (4.32), (4.33) and (4.34) are all functions of the two parameters η and β, so they cannot be solved until

a relation between them is established from either relations $\sin\beta = F/2R$ or $\cos\beta = C/R$. Considering the former expression and substituting the definition of F, equation (4.26), we obtain

$$\sin\beta = \sqrt{1 - 4\left(\eta^2 - \sin^2\frac{\beta}{2}\right)^2} \qquad (4.35)$$

and therefore, using the double-angle formulas and the change of variable (4.23)$_1$ we finally arrive at two relations between θ_q and β

$$\sin^2\left(\frac{\theta_q + \beta}{2}\right) = \frac{1}{2} \qquad \text{and} \qquad \sin^2\left(\frac{\theta_q + \beta}{2}\right) = 2\sin^2\left(\frac{\beta}{2}\right) - \frac{1}{2}, \quad (4.36)$$

where the latter has no physical meaning since requires $\theta_q < 0$, whereas the former is the equation we are looking for, which is symplified in

$$\theta_q + \beta = \frac{\pi}{2}, \qquad (4.37)$$

showing that at any load step, the resultant R is always perpendicular to the tangent of cantilever's free edge.

The loading paths of the elastic rod are reported in Fig. 4.7 in terms of dimensionless applied transverse force f as a function of the dimensionless additional length $\Delta L/L$ that is pushed out from the sleeve and the mid-span dimensionless deflection w/L, in order to compare them with the solution proposed by Humer [45], who did not take into account the effect of configurational force [5].

The strong difference between the proposed solution (red curve, that will be validate by experimental observations, see next section) and the incorrect

---

[5]Relation between the dimensionless applied force f and the kinematic parameter θ_q reported in [45] (in the following with superscript 'H') is

$$f^H = 128\iota^2\left\{\text{cn}\big(\mathcal{K}(\iota),\iota\big) - \text{cn}\left(\mathcal{K}\left(\arcsin\frac{\sqrt{2}}{2\iota},\iota\right),\iota\right)\right\}^2, \qquad (4.38)$$

where $\iota = \sqrt{\dfrac{1 + \sin\theta_q}{2}}$, while the dimensionless additional length is written as

$$\frac{\Delta L}{L}^H = \frac{\mathcal{K}(\iota) - \mathcal{K}\left(\arcsin\dfrac{\sqrt{2}}{2\iota},\iota\right)}{2\iota\left[\text{cn}\left(\mathcal{K}\left(\arcsin\dfrac{\sqrt{2}}{2\iota},\iota\right),\iota\right) - \text{cn}\big(\mathcal{K}(\iota),\iota\big)\right]} - 1, \qquad (4.39)$$

and the dimensionless mid-span deflection is

$$\frac{w}{L}^H = \frac{2E\left(\arcsin\dfrac{\sqrt{2}}{2\iota},\iota\right) - 2E(\iota) + \mathcal{K}(\iota) - \mathcal{K}\left(\arcsin\dfrac{\sqrt{2}}{2\iota},\iota\right)}{4\left[\text{cn}\left(\mathcal{K}\left(\arcsin\dfrac{\sqrt{2}}{2\iota},\iota\right),\iota\right) - \text{cn}\big(\mathcal{K}(\iota),\iota\big)\right]} \qquad (4.40)$$
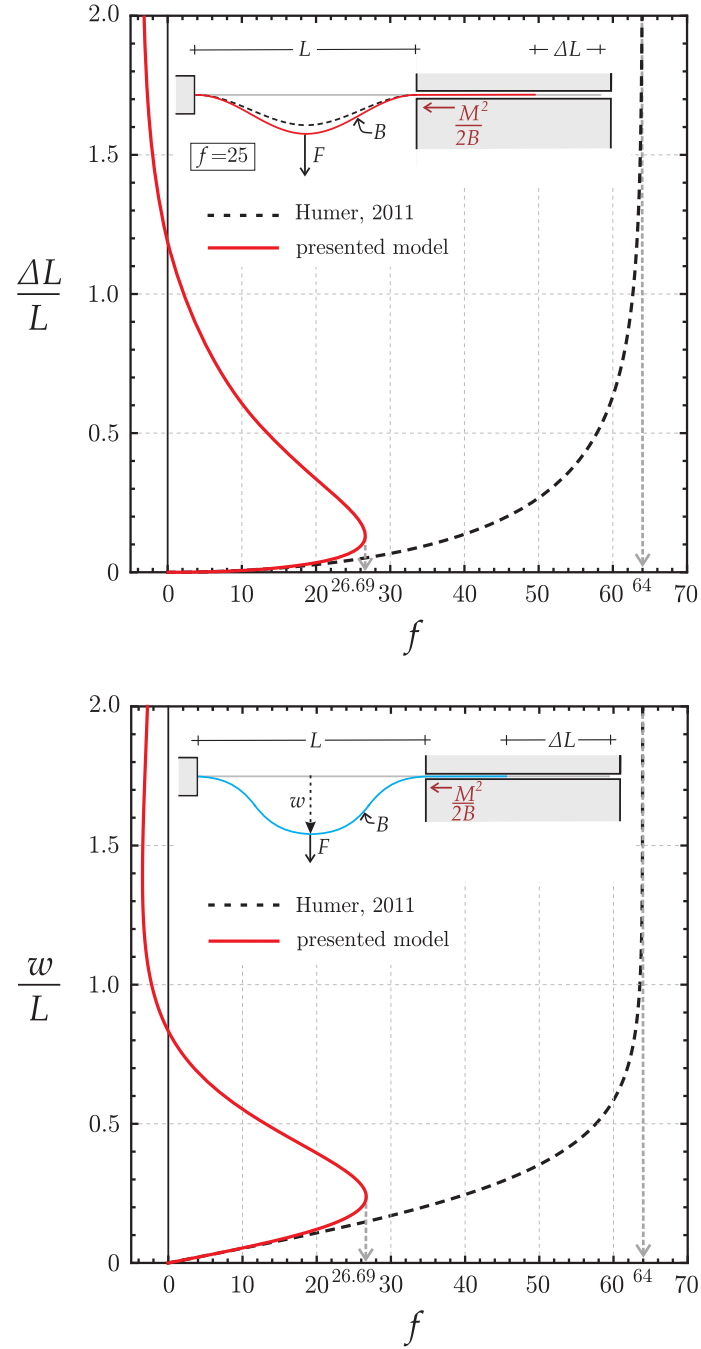
Figure 4.7: Equilibrium paths of the structure sketched in the inset subjected to a concentrated transverse load F. Proposed model considering the effect of configurational force (red curve) is compared with the incorrect solution in which the Eshelby-like force is neglected (dashed black curve). Dimensionless additional length $\Delta L/L$ (upper) and dimensionless mid-span deflection (lower) versus dimensionless applied load f.
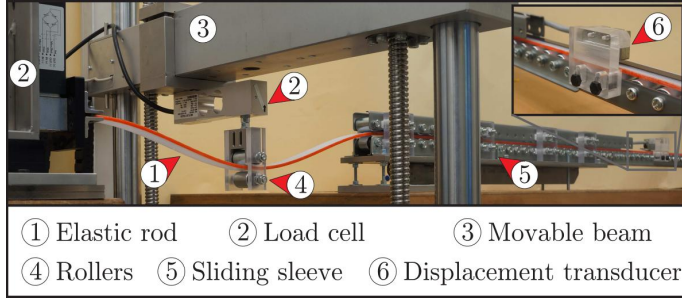
Figure 4.8: The experimental set up that realizes the structural scheme reported in Fig. 4.6.

in which the Eshelby-like force is neglected (black dashed curve) can be noted from Fig. 4.7. In particular, the maximum admissible dimensionless applied load f_{cr}, after which no equilibrium configurations exist and the rod slides indefinitely out of the sleeve, in the present model, is

$$f_{\text{cr}} \approx 26.69, \tag{4.41}$$

whereas $f_{\text{cr}}^H = 64$ is found in the incorrect solution, which is ≈ 2.4 higher than the correct value and therefore may represent a dangerous underestimation of the 'peak' load for this structural system. Furthermore, the loading paths are completely different, because in [45] the applied load F increases with an increase of the additional length ΔL, while in the proposed solution, after the 'critical' load f_{cr} is reached, a softening path is present in which the rod is in an unstable equilibrium configuration (or stable configuration under displacement control, as realized in the experiments) and an increase of the additional length ΔL implies a decrease of the transverse load F. This unstable path exhibits also a *force reversal* when $\Delta L \approx 1.19\,L$ or, equivalently either $w \approx 0.83\,L$ or $\theta_q = 90°$.

The effect of the Eshelby-like force is clearly visible in the inset of Fig. 4.7 (left), where the deformed configuration for a dimensionless load $f = 25$ obtained with our solution is reported together with the one calculated through the incorrect model, which shows less inflection.

4.2.1 Experimental

The system sketched in Fig. 4.6 has been realized to provide a direct experimental evidence of the theoretical predictions. In particular, the structural apparatus (Fig. 4.8) has been designed and manufactured at the Instabilities Lab (http://ssmg.unitn.it/) of the University of Trento.

The transverse load at the mid span of the system has been provided by using two rollers from Misumi Europe (Press-Fit Straight Type, 20 mm in diameter and 25 mm in length) acting on both the upper and lower side of

the elastic blade. This constraint has been fixed on the movable crosshead of a MIDI 10 load frame (from Messphysik) and leaves the blade free to move in the horizontal direction. The upper roller works when $F > 0$, whereas the lower roller is foundamental to register negative value of F. Three rods of same length (1600 mm) and width ($b = 24.9$ mm), but different height of the cross section ($h = \{1.9; 2.85; 3.85\}$ mm), have been employed during tests. The elastic rod are realized in solid polycarbonate (white 2099 Makrolon UV from Bayer, elastic modulus 2350 MPa). Two load cells and two displacement transducers have been mounted on the system (see Fig. 4.6) to monitor: (i.) the applied transverse load F using MT1041-R.C. 500N load cell (from Mettler S.p.A.), (ii.) the axial reaction at the clamp (equal to the Eshelby-like force C) using OC-K5U-C3-R.C. 50N load cell (from Gefran S.p.A), (iii.) the mid span deflection using a displacement transducer mounted into the load frame, and (iv.) the additional length that slide out of the sleeve employing a magnetic non-contact displacement transducer GC-MK5 (from Gemac). Data have been acquired with NI compactRIO system interfaced with Labview 2013 (National Instruments). The sliding sleeve in which the polycarbonate rod is free to slide consists of two parts of different length: the lower part (1250 mm) works as a support for the all strip, while the upper (500 mm), required only in the last part, is shorter in order to fix the device to measure the additional length through the magnetic displacement transducer. The lower and the upper sides of the sliding sleeve have been realized by employing respectively 82 and 32 rollers from Misumi Europe (Press-Fit Straight Type, 20 mm in diameter and 25 mm in length), modified to reduce friction. The tolerance between the polycarbonate rod and the rollers is calibrated with four micrometrical screws. Temperature near the testing machine has been monitored with a thermocouple connected to NI compaqRIO and has been found to lie around 22° C, without sensible oscillations during tests.

Experimental results, presented in Figs. 4.9, 4.10 and 4.11 for different thickness of the cross sections ($h = \{1.9; 2.85, 3.85\}$ mm), fully confirm the present model (and therefore prove the inaccuracy of the solution presented in [45]). In particular, Figs. 4.9 and 4.10 show an unstable (in load control) region after the maximum admissible load is reached and confirm the force reversal, for which an upward concentrated force is needed to guarantee equilibrium when $\Delta L/L \geq\sim 1.19$ or $w/L \geq\sim 0.83$. Moreover, the behaviour of the dimensionless Eshelby-like force as a function of the dimensionless concentrated load is reported in Fig. 4.11, showing that its magnitude is comparable to the applied force, and therefore has a noteworthy effect on this elastic system. In all cases the theoretical predictions have been found to be extremely tight to experimental results.
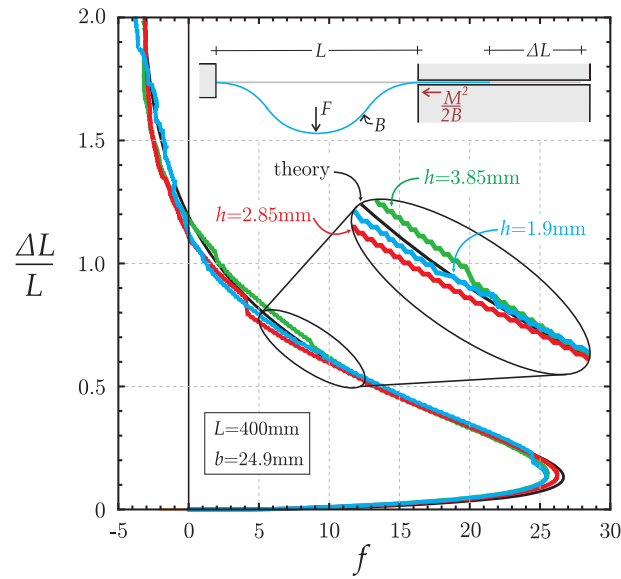
Figure 4.9: Comparison between theoretical (black curve) and experimental results performed on three rods with width $b = 24.9$ mm, but different thickness of $h = 1.9$ mm (blue curve), $h = 2.85$ mm (red curve) and $h = 3.85$ mm (green curve). Dimensionless additional length $\Delta L/L$ is reported as a function of the dimensionless transverse load f.
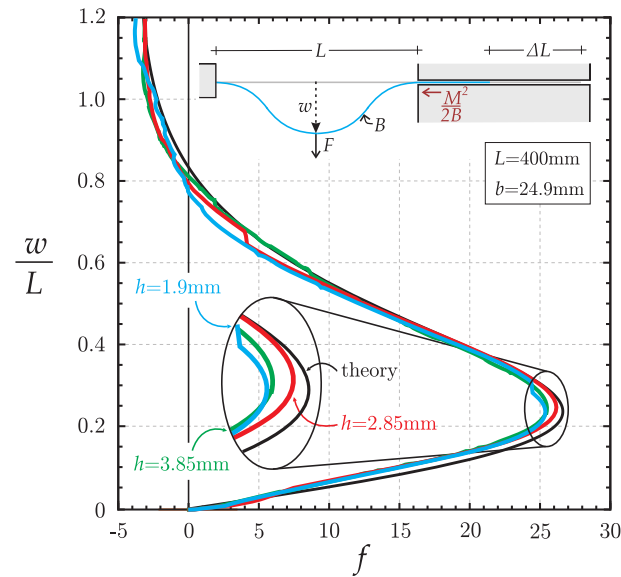
Figure 4.10: Comparison of theoretical (black curve) and experimental results for rods with different thickness of $h = 1.9$ mm (blue curve), $h = 2.85$ mm (red curve) and $h = 3.85$ mm (green curve). Dimensionless mid-span deflection w/L is reported as a function of the dimensionless transverse load f.

Figure 4.11: Comparison between theoretical prediction (black curve) and experimental results performed on rods with different cross sections: width $b = 24.9$ mm, $h = 1.9$ mm (blue curve), $h = 2.85$ mm (red curve) and $h = 3.85$ mm (green curve). Dimensionless 'Eshelby-like' force CL^2/B is reported versus dimensionless transverse load f.
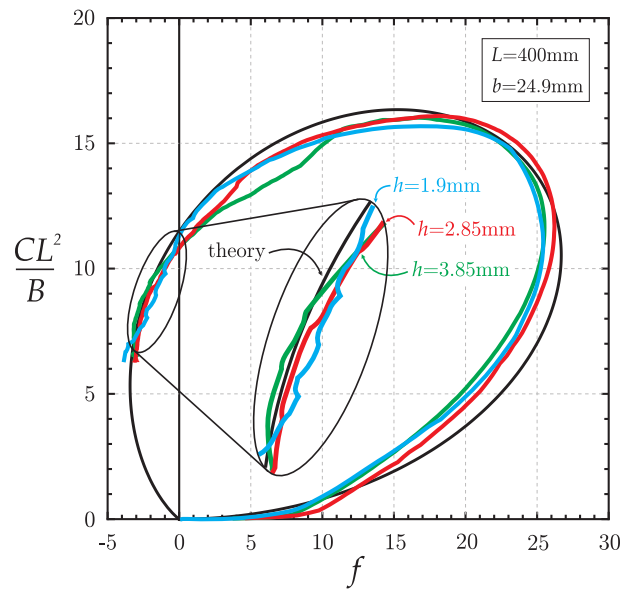
Chapter 5

Instability and restabilization of a penetrating blade

Application of a dead compressive load at the free end of an elastic rod (the 'blade') induces its penetration into a sliding sleeve ending with a linear elastic spring. Bifurcation and stability analysis of this simple elastic system shows a variety of unexpected behaviours: (i.) an increase of buckling load at decreasing of elastic stiffness; (ii.) a *finite* number of buckling loads for a system with infinite degrees of freedom (leading to a non-standard Sturm-Liouville problem); (iii.) more than one bifurcation loads associated to each bifurcation mode; (iv.) a restabilization of the straight configuration after the second bifurcation load associated to the first instability mode; (v.) the presence of an Eshelby-like (or configurational) force, deeply influencing stability; (vi.) a self-restabilization of the straight configuration is possible for compliant blades with imperfection of tilt angle or initial curvature.

Despite the common belief that structural instability is a fully mature field of mechanics, it has recently been shown that it is still possible to discover new and 'unexpected' phenomena in the critical and postcritical behaviour of simple structures, such as tensile buckling (Zaccaria et al. [49]), buckling inducing shrinking of a structure (Shim et al. [50]), multiple bifurcations in single degree of freedom structures (Bigoni et al. [51]), frictional flutter instability (Bigoni and Noselli [52]), and that buckling can be exploited to facilitate adhesion (Chan et al. [53]), or to create flexible electronics (Rogers et al. [54]), or to switch a phononic band gap (Bertoldi and Boyce [55]), or to induce a pattern transformation (Li et al. [56]).

The aim of the present chapter is to explore the critical and postcritical behaviour of a simple elastic structure, displaying several unexpected effects, some of which were previously known but received only marginal attention (Feodosyev [57]; Tarnai [58]), while others were simply unknown. The importance of the mechanical features highlighted and discovered here lies in the fact that they disprove common believes (for instance, engineers
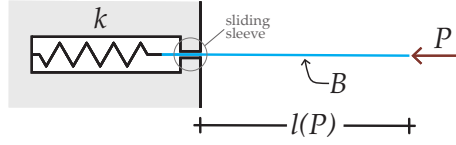
Figure 5.1: The penetrating blade is an elastic planar rod whose free length l is a function of the amount of the applied axial load P. The blade has a free end subject to the dead load P, while at the other edge the blade slides into a frictionless sleeve and is restrained by an axial linear spring.
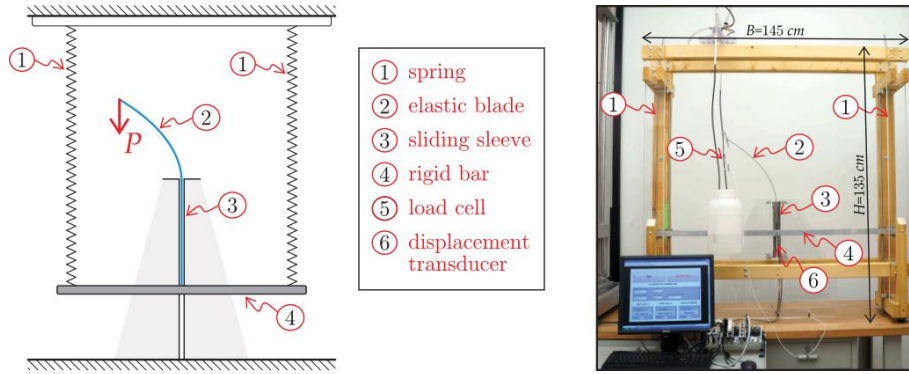
Figure 5.2: Left: the design scheme employed to realize the structure shown in Fig. 5.1 and right: its practical realization (prototype 1). Note that the sliding sleeve is borne by a transparent plexiglass support (represented grey on the left). Details of the experimental setup are given in Section 5.5.

believe that critical loads always increase with the stiffness of a structure, and mathematicians that a bifurcation problem of an elastic rod is always a Sturm-Liouville problem), correct errors in several published works (where the so-called 'Eshelby-like force' is wrongly omitted in the calculations, see references in Chapter 2 and Chapter 3), provide a new understanding of the adhesion energy between a structure and a substrate (Majidi [40]; Majidi et al. [41]), and open the way to unconventional mechanical applications, as for instance to continuous self-restabilizing systems (a simple example of this behaviour is reported by Potier-Ferry [59]). The considered mechanical problem is the following.

A blade (an elastic planar rod) is forced to penetrate an elastic movable clamp (a frictionless sliding sleeve with a final linear spring) through the application of a dead compressive load at the other edge, Fig. 5.1.

This system is shown to exhibit several surprising and counterintuitive mechanical behaviours, theoretically predicted by elastic analysis and experimentally confirmed through a physical model (Fig. 5.2, for details of the experimental setup see Section 5.5).

The sliding sleeve, which constrains one edge of an elastic rod, is shown in the previous chapter to induce Eshelby-like force in the structure, generated
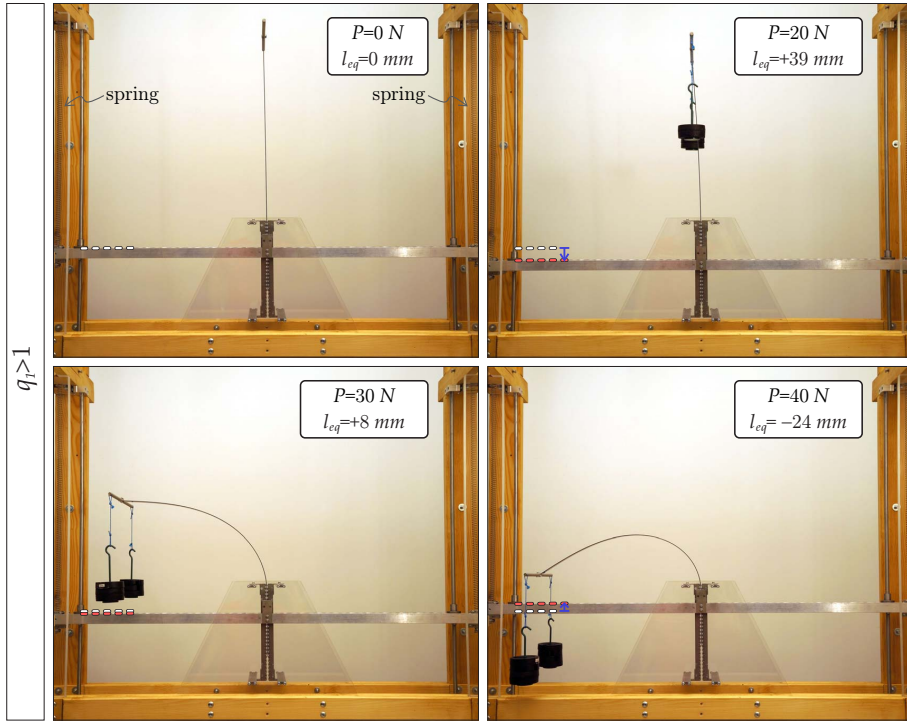
Figure 5.3: An Eshelby-like force is generated when the blade (elastic planar rod) buckles, so that the length of the rod inserted into the sliding sleeve (l_{eq}) decreases when the applied compressive load P is increased. As a consequence, the length of the rod inside the sliding sleeve can become even smaller than in the unloaded configuration (i.e. $l_{eq} < 0$, lower part, right) with the increasing of the compressive load. This counterintuitive effect is due to the presence of an vertical upward Eshelby-like force generated by the sliding sleeve which is greater than the vertical downward load P. The structural model has been realized following the scheme reported in Fig. 5.2.

by the fact that the rod, freely sliding at one edge, can change its length and therefore release elastic energy. The presence of a configurational force produced by the sliding sleeve in the structure shown in Fig. 5.1 strongly affects the post-critical behaviour and its stability. The effects of this force can be counterintuitive, so that the springs in the structure shown in Fig. 5.3 at low load (upper part on the right, $P = 20N$) are subject to an *higher* elongation than that occurring when a higher load P is applied (lower parts on the left, $P = 30N$, and on the right, $P = 40N$).

5.1 More than one critical load for each instability mode and finite number of critical loads for continuous elastic systems

Let us consider an inextensible elastic beam with constitutive behaviour defined by the Euler-Bernoulli equation

$$M(s) = B\frac{\mathrm{d}\theta(s)}{\mathrm{d}s},$$

(5.1)

where B is the constant bending stiffness, $\theta(s)$ is the angle of inclination of the tangent to the elastica at the curvilinear coordinate s. The Euler formula provides the n-th critical load (associated to the n-th instability mode) for an elastic clamped-free planar rod of length l as

$$P_{cr,n} = \frac{(2n-1)^2\pi^2 B}{4l^2}, \qquad n \in \mathbb{N}^+.$$

(5.2)

Equation (5.2) shows that the n-th critical load P_{cr} is unique whenever the beam length l is fixed, but this uniqueness may be lost when the length becomes a function of the applied axial load, $l = l(P)$.

If, as shown in Fig. 5.1, an axial spring is introduced, the elastic planar rod (or 'blade') can penetrate into the constraint (a sliding sleeve) of an amount l_{eq}, so that

$$l(P) = \bar{l} - l_{eq}(P),$$

(5.3)

where $\bar{l}$ is the outer length of the blade at null axial load P, $l(P=0) = \bar{l}$. In the particular case of a linear spring with stiffness k and considering the blade in the straight configuration the equilibrium equation in the axial direction is given by

$$P = kl_{eq},$$

(5.4)

(an equation that does not hold when the curvature at the point $s = l_{eq}$ is different from zero, $\theta'_{eq}(l_{eq}) \neq 0$, Section 5.2) so that the length of the outer part of the blade is $l(P) = \bar{l} - P/k$ and the Euler formula (5.2) becomes

$$P_{cr,n} = \frac{(2n-1)^2\pi^2 B}{4\left(\bar{l} - \dfrac{P_{cr,n}}{k}\right)^2}, \qquad n \in \mathbb{N}^+.$$

(5.5)

The solution for the critical load $P_{cr,n}$ from equation (5.5) leads to the following cubic equation

$$p_{cr,n}^3 - 2p_{cr,n}^2 + p_{cr,n} - \frac{4}{27q_n} = 0, \qquad n \in \mathbb{N}^+,$$

(5.6)

where $p_{cr,n}$ and q_n are respectively the dimensionless n-th critical load and dimensionless relative stiffness (spring stiffness multiplied by the bar length and divided by a critical load) of the elastic system, the latter given as

$$q_n = \frac{16k\bar{l}^3}{27(2n-1)^2\pi^2 B}, \qquad n \in \mathbb{N}^+, \tag{5.7}$$

and the former is the 'n-th' and critical 'cr' value of the dimensionless load

$$p = \frac{P}{k\bar{l}}. \tag{5.8}$$

Note that the dimensionless relative stiffness is positive, $q_n > 0$, defined in a way that for $n = 1$ there is no buckling for $q_1 < 1$, and that the dimensionless n-th critical load $p_{cr,n}$ has to satisfy the following inequality[1]

$$p_{cr,n} \leq 1, \qquad n \in \mathbb{N}^+, \tag{5.9}$$

corresponding to $l(P) \geq 0$, in other words, to the constraint that the blade cannot buckle after complete penetration into the sliding sleeve.

The solution of the cubic equation (5.6) yields the following conclusions:

i) since all the coefficients of the cubic equation (5.6) are real, the following infinite sequence always exists of real roots

$$p_{cr,n}^{\mathcal{C}} = \frac{1}{3}\left[2 + \sqrt[3]{\frac{q_n}{2 - q_n + 2\sqrt{1 - q_n}}} + \sqrt[3]{\frac{2 - q_n + 2\sqrt{1 - q_n}}{q_n}}\right] > 1,$$
$$n \in \mathbb{N}^+, \tag{5.10}$$

all violating the constraint (5.9) and thus representing meaningless solutions from mechanical point of view;

ii) in the case when for a given $m \in \mathbb{N}^+$ the inequality

$$q_{m+1} < 1 < q_m, \qquad \Leftrightarrow \qquad (2m-1)^2 < q_1 < (2m+1)^2, \tag{5.11}$$

is satisfied, in addition to the sequence of real roots (5.10) other $2m$ real roots exist for the cubic equation (5.6),

$$\left.\begin{array}{c} p_{cr,n}^{\mathcal{A}} \\[2mm] p_{cr,n}^{\mathcal{B}} \end{array}\right\} = \frac{1}{3}\left[2 - \frac{1 \pm i\sqrt{3}}{2}\sqrt[3]{\frac{q_n}{2 - q_n + 2\sqrt{1 - q_n}}}\right.$$
$$\left. - \frac{1 \mp i\sqrt{3}}{2}\sqrt[3]{\frac{2 - q_n + 2\sqrt{1 - q_n}}{q_n}}\right], \qquad n \in \mathbb{N}^+ \tag{5.12}$$

---

[1] This restriction holds only for the calculation of the critical loads. Indeed, as it will be shown in Section 5.2, equilibrium configurations with $p \geq 1$ are possible for non-trivial deformation paths.

satisfying the following property

$$0 < p_{cr,n}^{\mathcal{A}} \leq p_{cr,m}^{\mathcal{A}} \leq p_{cr,m}^{\mathcal{B}} \leq p_{cr,n}^{\mathcal{B}} < 1, \qquad n \leq m \qquad n, m \in \mathbb{N}^+ \tag{5.13}$$

so that $2m$ critical loads are obtained, which correspond to 2 critical loads for the same n-th instability mode;

iii) in the particular case when, for a given $m \in \mathbb{N}^+$, $q_m = 1$ (or, equivalently, $q_1 = [2m-1]^2$), the two real roots associated to the m-th mode (5.12) are coincident,

$$p_{cr,m}^{\mathcal{A}} = p_{cr,m}^{\mathcal{B}} = \frac{1}{3}, \qquad m \in \mathbb{N}^+, \tag{5.14}$$

so that $2m-1$ critical loads are obtained, though $2m$ postcritical paths still exist.

Usually, a compressed elastic rod (with ordinary boundary conditions, e.g. doubly pinned) evidences one bifurcation load of the fundamental equilibrium path associated to each bifurcation mode. The structure shown in Fig. 5.1 displays *two* (actually three, but one of these will be shown to be physically not accessible) *bifurcation loads for the straight configuration associated to each bifurcation mode*, a situation occurring also in the simpler system analyzed by Bigoni [13].

Dimensionless critical loads, calculated with equation (5.12), are reported as functions of the dimensionless relative stiffness parameter q_1 in Fig. 5.4 for the first three modes ($n = 1$, 2, 3) together with the experimental data observed on Prototype 1. As it will be shown in the following, the dimensionless load $p_{cr,1}^{\mathcal{A}}$ corresponds to the lower buckling load and to the loss of stability of the straight configuration, while the dimensionless load $p_{cr,1}^{\mathcal{B}}$ corresponds to the upper bifurcation load and to the restabilization of the straight configuration. Note that there is no bifurcation for $q_1 < 1$ (the situation shown in Fig. 5.5 (upper part), but for $q_1 > 1$ there are always two bifurcation loads associated to the first mode ($n=1$) (called 'buckling' and 'restabilization') and later, for sufficiently high q_1, there are two bifurcation loads associated to the second mode and two to the third.

Moreover, while $p_{cr,1}^{\mathcal{A}}$ corresponds to a critical *buckling* load for which there is a spontaneous departure from the straight configuration of the blade, $p_{cr,1}^{\mathcal{B}}$ denotes a load from which the straight configuration returns to be stable, but cannot be spontaneously reached by the blade from its buckled configuration. Finally, we may observe the following.

⋄ The buckling load of the system is governed by the relative spring/bending stiffness, so that *an increase (decrease) of elastic stiffness of the spring yields a decrease (increase) in the buckling load.* Moreover, if the stiffness of the spring is low enough compared to the rod's bending stiffness ('highly compliant' system), there will be no buckling, but only
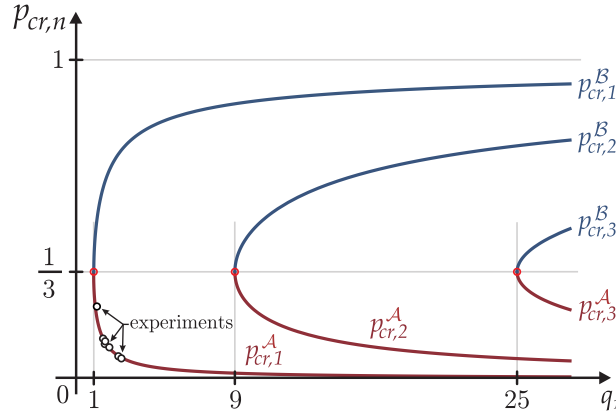
Figure 5.4: Dimensionless bifurcation loads $p_{cr,n}$ (*buckling* load $p^{\mathcal{A}}_{cr,n}$ and *restabilization* load $p^{\mathcal{B}}_{cr,n}$) as a function of the dimensionless relative stiffness q_1 of the elastic system. Note that if the stiffness ratio q_1 decreases, then the n-th buckling load increases while the n-th restabilization load decreases, and the number of bifurcation modes can even reduce to zero in the case of 'highly compliant systems' ($q_1 < 1$), where bifurcation does not occur. Experimental data (white dots) observed on Prototype 1 are also reported.

a straight penetration into the sliding sleeve. In these conditions an *increase in the elastic stiffness of the spring* may induce buckling, Fig. 5.5. Previously, this effect was theoretically noticed by Feodosyev [57] and on a simpler structure by Tarnai [58].;

◇ Buckling of an elastic rod (with ordinary boundary conditions, e.g. doubly pinned) is governed by a Sturm-Liouville problem (Broman [34]), admitting an infinite number of bifurcation loads. This is related to the fact that the system 'has infinite degrees of freedom'. Although the system shown in Fig. 1 is continuous, the moving boundary introduced by the sliding sleeve leads to a non-standard Sturm-Liouville problem, so that a *finite* number (which depends on the elastic properties of the system) of pairs (two for each mode) of buckling loads is found.

5.2 Total potential energy and equilibrium equations

An inextensible elastic planar rod (straight in its unloaded configuration, with bending stiffness B and total length $\bar{l}$) has one end constrained with a sliding sleeve and a coaxial spring of stiffness k, while at the other edge is subject to an axial (dead compressive) force P, see Fig. 5.1. Introducing the curvilinear coordinate $s \in [0, \bar{l}]$ and the rotation field $\theta(s)$ of the planar rod's axis, the axial and transverse equations decribing the shape of the elastica
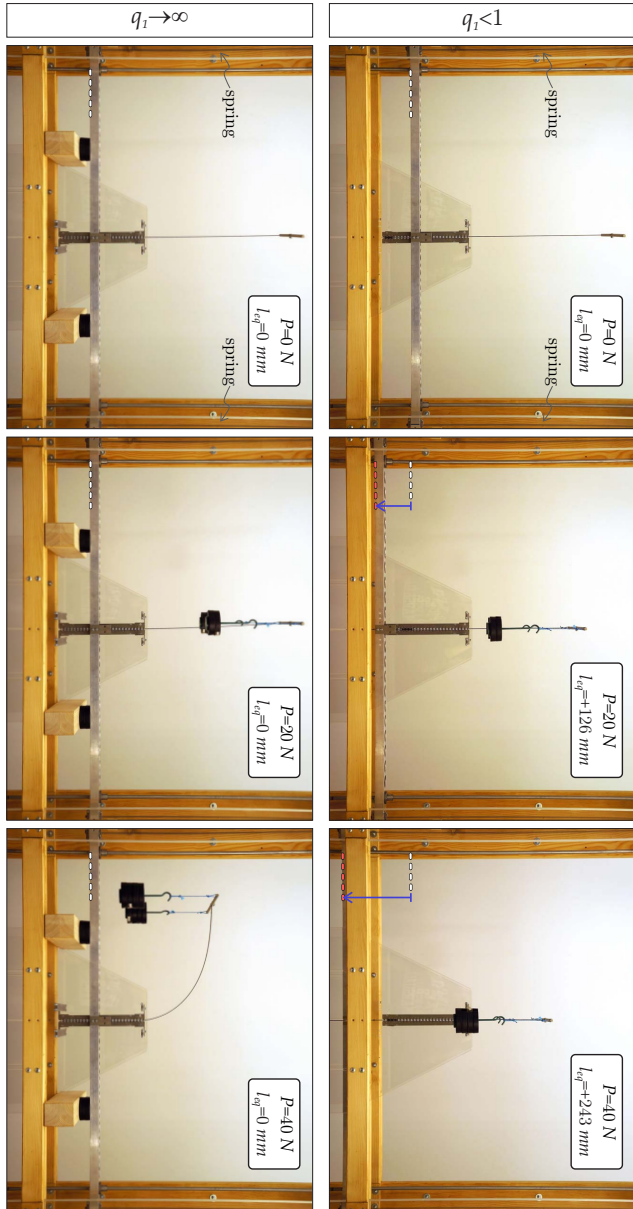
Figure 5.5: A blade (an elastic planar rod) subject to a dead compressive load P on an edge does not evidence buckling when can penetrate into a sliding sleeve restrained by springs (upper part). The same blade buckles when it is clamped at the lower edge (lower part). This model (which can be better understood by analyzing the scheme reported in Fig. 5.2) shows that an increase of stiffness (the lower clamp is infinitely stiff when compared with the springs restraining the penetration into the sliding sleeve) may lower the buckling load. The length of the blade inside the sliding sleeve at equilibrium is l_{eq}, while q_1 is the dimensionless relative stiffness defined by equation (5.7).

can be written as

$$x_1(s) = \int \cos\theta(s)\mathrm{d}s, \qquad x_2(s) = \int \sin\theta(s)\mathrm{d}s. \tag{5.15}$$

With reference to the structural system reported in Fig. 5.1, the sliding sleeve introduces the condition of null rotation for a portion of the rod,

$$\theta(s) = 0, \qquad s \in [0, l_{in}], \tag{5.16}$$

where l_{in} is the length of the rod inside the (frictionless, perfectly smooth and bilateral) sliding sleeve, while on the other end of the rod ($s = \bar{l}$) the boundary condition is

$$\theta'\left(\bar{l}\right) = 0. \tag{5.17}$$

The total potential energy is

$$\mathcal{V}(\theta, l_{in}) = \int\limits_{l_{in}}^{\bar{l}} B\frac{\left[\theta'(s)\right]^2}{2}\mathrm{d}s + \frac{1}{2}k\left(l_{in}\right)^2 - P\left[\bar{l} - \int\limits_{l_{in}}^{\bar{l}} \cos\theta(s)\mathrm{d}s\right]. \tag{5.18}$$

Since the total potential energy (5.18) is written for a system with a moving boundary l_{in}, it is expedient (Courant and Hilbert [44], see also Majidi et al. [41]) to introduce a small parameter ϵ and to take variations (subscript 'var') of an equilibrium configuration (subscript 'eq') in the form

$$\theta(s, \epsilon) = \theta_{eq}(s) + \epsilon\theta_{var}(s), \qquad l_{in}(\epsilon) = l_{eq} + \epsilon l_{var}, \tag{5.19}$$

with the boundary conditions at the sliding sleeve ($s = l_{in}$)

$$\theta_{eq}(l_{eq}) = 0, \qquad \theta(l_{eq} + \epsilon l_{var}) = 0, \tag{5.20}$$

and the boundary conditions at the other end ($s = \bar{l}$)

$$\theta'_{eq}\left(\bar{l}\right) = 0, \qquad \theta'_{var}\left(\bar{l}\right) = 0. \tag{5.21}$$

A Taylor series expansion of $\theta(l_{in})$ for small ϵ yields

$$\theta(l_{eq} + \epsilon l_{var}, \epsilon) = \theta_{eq}(l_{eq}) + \epsilon\left[\theta_{var}(l_{eq}) + \theta'_{eq}(l_{eq})l_{var}\right]$$
$$+ \frac{\epsilon^2}{2}l_{var}\left[2\theta'_{var}(l_{eq}) + \theta''_{eq}(l_{eq})l_{var}\right] + \mathcal{O}\left(\epsilon^3\right), \tag{5.22}$$

so that the boundary conditions (5.20) lead to the following compatibility equations

$$\theta_{var}(l_{eq}) + \theta'_{eq}(l_{eq})l_{var} = 0, \quad 2\theta'_{var}(l_{eq}) + \theta''_{eq}(l_{eq})l_{var} = 0. \tag{5.23}$$

The first variation of the total potential energy (5.18) is

$$\delta_\epsilon \mathcal{V} = + \int\limits_{l_{eq}}^{\bar{l}} B\theta'_{eq}\theta'_{var}(s)\mathrm{d}s - \int\limits_{l_{eq}}^{\bar{l}} P\sin\theta_{eq}(s)\theta_{var}(s)\mathrm{d}s \\ + \left[kl_{eq} - P\cos\theta_{eq}(l_{eq}) - \frac{B}{2}\theta'_{eq}(l_{eq})^2 \right] l_{var}, \tag{5.24}$$

and, taking into account the Leibniz rule of differentiation (see Section 3.1) and the boundary conditions (5.20) and (5.21), together with compatibility equations (5.23), through integration by parts, the first variation of the functional $\mathcal{V}$ becomes

$$\delta_\epsilon \mathcal{V} = - \int\limits_{l_{eq}}^{\bar{l}} \left[B\theta''_{eq} + P\sin\theta_{eq}(s) \right] \theta_{var}(s)\mathrm{d}s + \left[kl_{eq} - P + \frac{B}{2}\theta'_{eq}(l_{eq})^2 \right] l_{var}, \tag{5.25}$$

from which, by imposing vanishing for any admissible variation $\theta_{var}(s)$ and l_{var}, the elastica is obtained

$$B\theta''_{eq}(s) + P\sin\theta_{eq}(s) = 0, \tag{5.26}$$

as well as the axial equilibrium condition

$$P = kl_{eq} + \underbrace{\frac{B}{2}\left[\theta'_{eq}(l_{eq}) \right]^2}_{\text{Eshelby-like Force}}, \tag{5.27}$$

revealing the presence of an Eshelby-like force (Chapter 3 and Bigoni et al. [9]) generated by the sliding sleeve (see also the asymptotic derivation by Balabukh et al. [43]) and representing the so-called 'transversality condition' of Courant and Hilbert [44]. Note that, equation (5.27) reduces to the 'trivial' axial equilibrium equation, equation (5.4), only in the case of null curvature at the sliding sleeve, $\theta'_{eq}(l_{eq}) = 0$.

It can be noted from the axial equilibrium equation (5.27) that, the surprising (and never noticed before) equilibrium configuration shown in Fig. 5.6 is possible in the absence of the spring ($k = 0$), when the elastica is such that the curvature at the sliding sleeve satisfies

$$P = \frac{B}{2}\left[\theta'_{eq}(l_{eq}) \right]^2, \tag{5.28}$$

corresponding to the fact the dead load P and the Eshelby-like force are equal and opposite. In the absence of the *vertical* configurational force the equilibrium would be impossible (note that this configuration for the structure is unstable, as will be proven in Section 5.3 but has been photographed due to the small friction inside the sliding sleeve, even if a small perturbation of the system causes its collapse).
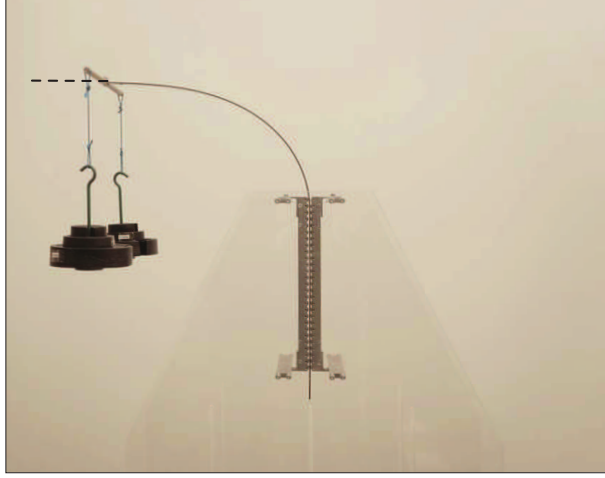
Figure 5.6: The vertical and upward Eshelby-like force (equal and opposite to the applied downward load) generated by the sliding sleeve makes the equilibrium configuration possible, even if unstable. Note that the tangent to the end of the blade is horizontal, as will be theoretically rationalized in the next section.

5.2.1 The elastica

The rotation field at equilibrium $\theta_{eq}(s)$ (Fig. 5.1) is the solution of the following non-linear second–order differential equation with moving boundary condition

$$\begin{cases} \dfrac{\mathrm{d}^2\theta_{eq}(s)}{\mathrm{d}s^2} + \lambda^2 \sin\theta_{eq}(s) = 0, \qquad s \in \left(l_{eq}, \bar{l}\right) \\[2mm] \theta_{eq}\left(l_{eq}\right) = 0, \\[2mm] \dfrac{\mathrm{d}\theta_{eq}(s)}{\mathrm{d}s}\bigg|_{s=\bar{l}} = 0, \\[2mm] \lambda^2 = \dfrac{k}{B}l_{eq} + \dfrac{1}{2}\left[\theta'_{eq}(l_{eq})\right]^2, \end{cases} \tag{5.29}$$

where the normalized axial load $\lambda^2 = P/B$ has been introduced.

The problem has the trivial solution (denoted with $^{(0)}$)

$$\theta_{eq}^{(0)}(s) = 0, \qquad l_{eq}^{(0)} = \frac{P}{k}, \tag{5.30}$$

while non-trivial solutions can be obtained through the following procedure. Multiplication of equation $(5.29)_1$ by $d\theta_{eq}/ds$ and integration in the variable s yields

$$\left[\frac{\mathrm{d}\theta_{eq}(s)}{\mathrm{d}s}\right]^2 - 2\lambda^2 \cos\theta_{eq}(s) = \text{constant}, \tag{5.31}$$

so that, setting $\theta_{eq}(\bar{l}) = \theta_{\bar{l}}$ and using the boundary condition $(5.29)_3$, it follows only the solution with the '+' sign has been considered)

$$\frac{\mathrm{d}\theta_{eq}(s)}{\mathrm{d}s} = \lambda\sqrt{2(\cos\theta_{eq}(s) - \cos\theta_{\bar{l}})}. \tag{5.32}$$

It is now a standard expedient to operate the following change of variables

$$\eta = \sin\frac{\theta_{\bar{l}}}{2}, \qquad \eta\sin\phi(s) = \sin\frac{\theta_{eq}(s)}{2}, \tag{5.33}$$

leading to the following differential problem equivalent to the system (5.29)

$$\begin{cases} \dfrac{\mathrm{d}\phi(s)}{\mathrm{d}s} = \lambda\sqrt{1 - \eta^2\sin^2\phi(s)}, \\[2mm] \phi(l_{eq}) = h\pi, \\[2mm] \phi(\bar{l}) = \dfrac{2j+1}{2}\pi, \qquad h,j \in \mathbb{Z} \\[2mm] l_{eq} = \lambda^2\dfrac{B}{k}(1 - 2\eta^2). \end{cases} \tag{5.34}$$

Integration of the differential problem (5.34) leads to non-trivial η, related to the rotation of the loaded end $\theta_{\bar{l}}$ through equation (5.33), as a function of the load parameter λ,

$$(2n-1)\mathcal{K}(\eta) = \lambda\left[\bar{l} - \lambda^2\frac{B}{k}(1 - 2\eta^2)\right], \qquad n \in \mathbb{N}^+, \tag{5.35}$$

where n corresponds to the number of the instability mode and $\mathcal{K}(\eta)$ is the complete elliptic integral of the first kind,

$$\mathcal{K}(\eta) = \int_0^{\frac{\pi}{2}} \frac{\mathrm{d}\phi}{\sqrt{1 - \eta^2\sin^2\phi}}. \tag{5.36}$$

Using the dimensionless parameters p_n and q_n, equation (5.7) and (5.8), the solution (5.35) can be rewritten in the following form

$$(1 - 2\eta^2)^2 p_n^3 - 2(1 - 2\eta^2)p_n^2 + p_n - \frac{4}{27q_n}\left[\frac{2\mathcal{K}(\eta)}{\pi}\right]^2 = 0, \qquad n \in \mathbb{N}^+, \tag{5.37}$$

which is a cubic equation providing in general three 'deformation paths' $(\mathcal{A}_n; \mathcal{B}_n; \mathcal{C}_n)$ corresponding to the n-th mode, namely, three dimensionless loads $(p_n^{\mathcal{A}}; p_n^{\mathcal{B}}; p_n^{\mathcal{C}})$ for each mode as functions of the rotation at the loaded

end $\theta_{\bar{l}}$, through inversion of relation $(5.33)_1$, and the relative dimensionless stiffness q_n

$$p_n^{\mathcal{A}} = p_n^{\mathcal{A}}(\theta_{\bar{l}}, q_n), \qquad p_n^{\mathcal{B}} = p_n^{\mathcal{B}}(\theta_{\bar{l}}, q_n), \qquad p_n^{\mathcal{C}} = p_n^{\mathcal{C}}(\theta_{\bar{l}}, q_n), \qquad n \in \mathbb{N}^+. \tag{5.38}$$

Note that in the limit of undeformed configuration (implying a null angle at the loaded end $\theta_{\bar{l}} \to 0$, so that $\eta \to 0$, $\mathcal{K}(\eta \to 0) \to \pi/2$), the cubic equation (5.37) corresponds to that obtained within the small displacement theory, equation (5.6), and again yields the critical dimensionless loads $(p_{cr,n}^{\mathcal{A}}; p_{cr,n}^{\mathcal{B}}; p_{cr,n}^{\mathcal{C}})$, given by equation (5.10) and (5.12).

For a given value of the applied load, the rotation at the loaded end (related to the three 'deformation paths') can be computed from equation (5.37) and then, through inversion of relation $(5.33)_1$, the corresponding rotation field can be obtained

$$\theta_{eq}(s) = 2 \arcsin\left[\eta \operatorname{sn}\left(\lambda\left(s - l_{eq}\right), \eta\right)\right], \tag{5.39}$$

from which the axial and transverse equations describing the shape of the elastica are obtained by integration, equation (5.15), as

$$
\begin{aligned}
x_1(s) &= -s + \frac{2}{\lambda} E\left[\operatorname{am}\left(\lambda\left(s - l_{eq}\right), \eta\right), \eta\right] - l_{eq}, \\
x_2(s) &= \frac{2\eta}{\lambda}\left[1 - \operatorname{cn}\left(\lambda\left(s - l_{eq}\right), \eta\right)\right],
\end{aligned}
\tag{5.40}
$$

which can be evaluated at the loaded end in order to obtain axial and transverse displacements, thus yielding

$$u_1\left(\bar{l}\right) = \frac{2}{\lambda}\left[E\left(\eta\right) - \mathcal{K}\left(\eta\right)\right] - l_{eq}, \qquad u_2(\bar{l}) = \frac{2\eta}{\lambda}. \tag{5.41}$$

In equation (5.40) the functions am, cn and sn denote the Jacobi amplitude, Jacobi cosine amplitude and Jacobi sine amplitude functions,

$$\operatorname{cn}\left(x, \eta\right) = \cos\left[\operatorname{am}\left(x, \eta\right)\right], \qquad \operatorname{sn}\left(x, \eta\right) = \sin\left[\operatorname{am}\left(x, \eta\right)\right], \tag{5.42}$$

while $E(x, \eta)$ is the incomplete elliptic integral of the second kind of modulus η, defined as

$$E(x, \eta) = \int_o^x \sqrt{1 - \eta^2 \sin^2 t} \, \mathrm{d}t. \tag{5.43}$$

Finally, in the case when the stiffness of the axial spring vanishes ($k = 0$, Fig. 5.6), equation (5.28) represents the only possible equilibrium configuration of the system. This equation can be rewritten, by introducing a change of variables in equation (5.33), as

$$1 - 2 \sin^2\left(\frac{\theta_{\bar{l}}}{2}\right) = 0. \tag{5.44}$$

Equation (5.44) reveals that the only equilibrium configuration for the system without spring occurs when the end tangent to the rod is orthogonal to the sliding sleeve, $\theta_{\bar{l}} = \pi/2$, representing *a purely geometrical condition*, visibly satisfied in Fig. 5.6.

Note that, when $k = 0$, if another load P^* will be hung at the other free end of the rod (at the end of the rectilinear part of the blade outside the sliding sleeve, bottom part of Fig. 5.6), the unique (unstable) equilibrium configuration, shown in Fig. 5.7, is possible through the following relation

$$P \cos \theta_{\bar{l}} + P^* = 0, \tag{5.45}$$

where the two weights have to satisfied the condition

$$0 \leq \frac{P^*}{P} \leq 1, \tag{5.46}$$

and the limit $P^* = 0$ occurs in Fig. 5.6, while $P^* = P$ reveals a non-physical situation because means $\theta_{\bar{l}} = \pi$, a situation that happens only if the length of the inflected elastica tends to ∞.

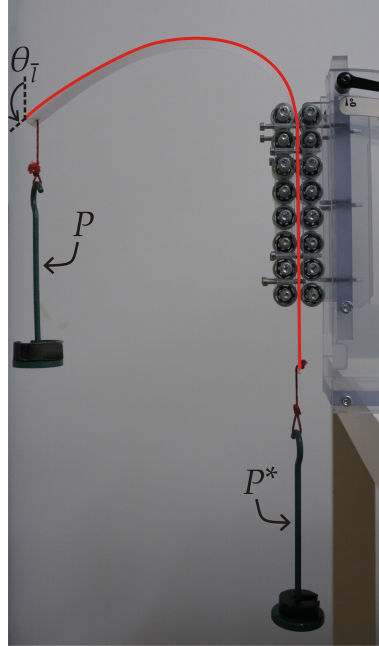

Figure 5.7: The Eshelby-like force guarantees other equilibria by hunging another load at the bottom end of the rod. The geometrical condition of equilibrium is possible when equation 5.45 is satisfied. In figure the loads are $P = 2$N and $P^* = 3$N, so that the angle $\theta_{\bar{l}} = 131.81°$.

This concept will be used in Chapter 6 for the design of an innovative elastica arm scale.

5.3 Stability of configurations

In order to evaluate the stability of the equilibrium configurations for the penetrating blade, the second variation of the functional $\mathcal{V}$, equation (5.18), has to be calculated. Considering the boundary conditions (5.20) and the perturbations in the rotation field $\theta_{var}(s)$ and in the length l_{var} satisfying the compatibility equations (5.23), the second variation evaluated at an inflexed equilibrium configuration can be written as

$$\delta_\epsilon^2 \mathcal{V} = \frac{1}{2} \left\{ k l_{var}^2 + B \int\limits_{l_{eq}}^{\bar{l}} \left[\theta_{var}'(s) \right]^2 \mathrm{d}s - P \int\limits_{l_{eq}}^{\bar{l}} [\theta_{var}(s)]^2 \cos\theta_{eq}(s) \mathrm{d}s \right\}. \tag{5.47}$$

The stability or instability of an equilibrium configuration is then related to the sign of the second variation $\delta_\epsilon^2 \mathcal{V}$, evaluated for that equilibrium configuration, namely,

$$\delta_\epsilon^2 \mathcal{V} = \begin{cases} > 0 & \text{stable equilibrium configuration,} \\ < 0 & \text{unstable equilibrium configuration,} \end{cases} \tag{5.48}$$

for any admissible perturbations $\theta_{var}(s)$ and l_{var} satisfying the compatibility equation (5.23).

Considering the auxiliary function $\Gamma(s)$, solution of the following boundary value problem (the Riccati equation plus a boundary condition, see van Brunt [60])

$$\begin{cases} \dfrac{\partial \Gamma(s)}{\partial s} - P \cos\theta_{eq}(s) - \dfrac{\Gamma(s)^2}{B} = 0, \\ \Gamma(\bar{l}) = 0, \end{cases} \tag{5.49}$$

the compatibility equation (5.23) and the following identity

$$\int\limits_{l_{eq}}^{\bar{l}} \frac{\mathrm{d}}{\mathrm{d}s} \left[\theta_{var}^2(s) \Gamma(s) \right] \mathrm{d}s - \left[\theta_{var}^2(s) \Gamma(s) \right]_{l_{eq}}^{\bar{l}} = 0, \tag{5.50}$$

the second variation, equation (5.47), can be rewritten as

$$\delta_\epsilon^2 \mathcal{V} = \frac{1}{2} \left\{ B \int\limits_{l_{eq}}^{\bar{l}} \left[\theta_{var}'(s) + \frac{\Gamma(s)}{B} \theta_{var}(s) \right]^2 \mathrm{d}s + l_{var}^2 \left[\left[\theta_{eq}'(l_{eq}) \right]^2 \Gamma(l_{eq}) + k \right] \right\}. \tag{5.51}$$

To judge the stability of the equilibrium configurations, the two conditions obtained by Majidi et al. [41] are exploited here. In particular (note that the existence of a bounded $\Gamma(s)$ on the interval $\left[l_{eq}, \bar{l} \right]$ implies that the integral in (5.51) is non-negative)

⬦ *Necessary condition* (N) for the equilibrium configuration defined by $\{\theta_{eq}(s), l_{eq}\}$ to be stable (so that it minimizes the functional $\mathcal{V}$) are that

  – (N_1) the auxiliary function $\Gamma(s)$, solution of to the boundary-value problem (5.49), cannot become unbounded in the interval $\left[l_{eq}, \bar{l}\,\right]$;
  – (N_2) the following inequality is satisfied

$$\Delta = \left[\theta'_{eq}(l_{eq})\right]^2 \Gamma(l_{eq}) + k \geq 0. \tag{5.52}$$

⬦ *Sufficient condition* (S) for the trivial $\{\theta_{eq}(s) = 0, l_{eq} = P/k\}$ equilibrium configuration to be stable is that the auxiliary function $\Gamma(s)$, solution of the boundary-value problem (5.49), is bounded.

In order to obtain the auxiliary function $\Gamma(s)$, it is instrumental to consider the Jacobi transformation

$$\Gamma(s) = -B \frac{\Lambda'(s)}{\Lambda(s)}, \tag{5.53}$$

leading to the following Jacobi boundary value problem

$$\begin{cases} \Lambda''(s) + \lambda^2 \cos\theta_{eq}(s)\, \Lambda(s) = 0, \\ \Lambda(\bar{l}) = 1, \\ \Lambda'(\bar{l}) = 0. \end{cases} \tag{5.54}$$

Once the function $\Gamma(s)$ and the auxiliary function $\Lambda(s)$ are obtained for a specific equilibrium configuration by solving the differential equation (5.49) and (5.54), the stability of that equilibrium configuration can be judged through the necessary (N_1 and N_2) and sufficient (S) conditions.

5.3.1 Stability of trivial configurations

In the case when the equilibrium configuration is straight, identifying the trivial solution $\{\theta_{eq}(s) = 0;\ l_{eq} = P/k\}$, the Jacobi boundary value problem (5.54) simplifies to

$$\begin{cases} \Lambda''(s) + \lambda^2 \Lambda(s) = 0, \\ \Lambda(\bar{l}) = 1, \\ \Lambda'(\bar{l}) = 0, \end{cases} \tag{5.55}$$

which, through the Jacobi transformation (5.53), leads to the following solution for the auxiliary function $\Gamma(s)$

$$\Gamma(s) = \sqrt{PB} \tan\left(\sqrt{\frac{P}{B}}\,(\bar{l} - s)\right). \tag{5.56}$$

The auxiliary function $\Gamma(s)$, equation (5.56), is bounded for $s \in \left[l_{eq} = P/k, \bar{l} \, \right]$ if and only if

$$\frac{P}{B} \left(\bar{l} - \frac{P}{k} \right)^2 < \frac{\pi^2}{4}, \qquad (5.57)$$

which can be rewritten in the dimensionless form

$$p \left(1 - p \right)^2 < \frac{4}{27 q_1}, \qquad (5.58)$$

so that, considering the necessary (N_1 and N_2) and sufficient (S) conditions, the *trivial straight configuration is*:

◇ for $q_1 < 1$: *stable* ('highly compliant' systems, see equation (5.7));

◇ for $q_1 > 1$:

    − *stable*   if $P < P_{cr,1}^{\mathcal{A}}$,

    − *unstable*   if $P_{cr,1}^{\mathcal{A}} < P < P_{cr,1}^{\mathcal{B}}$,

    − *stable*   if $P_{cr,1}^{\mathcal{B}} < P < k\bar{l}$.

In usual structural systems, stability of the fundamental path is lost after buckling and is not 'later' recovered. Differently, the straight configuration of the structure shown in Fig. 5.1 returns to be stable after a second bifurcation load (associated to the first instability mode) is met (Fig. 5.8), a situation occurring also in the simpler systems analyzed by Bigoni [13] and Potier-Ferry [59].[2]

5.3.2   Stability of non-trivial configurations

In the case of non-trivial equilibrium configurations, $\theta_{eq}(s) \neq 0$, the function $\Lambda(s)$, solution of the Jacobi problem (5.54), can be obtained only through numerical integration. Numerical investigations performed varying the dimensionless relative stiffness q_1 and the applied load P show which non-trivial configuration is unstable, through application of the necessary condition (N). In particular, a configuration is unstable either (N_1) when the function $\Lambda(\hat{s}) = 0$ with $\hat{s} \in \left[l_{eq}, \bar{l} \, \right)$, namely, the auxiliary function $\Gamma(s)$, is bounded, or (N_2) when $\Delta < 0$, see equation (5.52).

It is concluded that *unstable equilibrium configurations* are:

◇ all the investigated non-trivial equilibrium configurations of the paths $\mathcal{A}_n$, $\mathcal{B}_n$, and $\mathcal{C}_n$ with $n \geq 2$, due to condition (N_1);

---

[2] For monotonically increasing loading the structure buckles and does not 'spontaneously' return in the straight configuration. Therefore, the system has to be set in this configuration to observe its stability beyond the second buckling load.

A system that spontaneously self-restabilizes has been shown by Potier-Ferry [59].
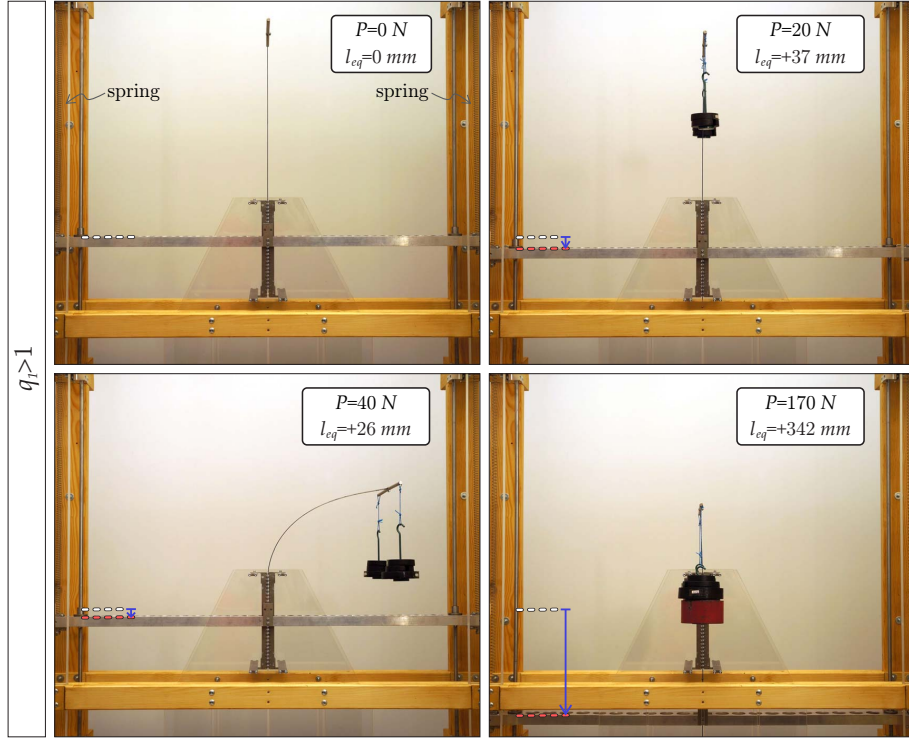
Figure 5.8: The straight configuration for the blade (elastic planar rod) is stable at small load (upper part, right), becomes unstable at higher load (lower part, left) and, for further increase, it eventually returns stable (lower part, right). The structural model has been realized following the scheme reported in Fig. 5.2. The length of the blade inside the sliding sleeve at equilibrium is l_{eq}, while q_1 is the dimensionless relative stiffness defined by equation (5.7).

$\diamond$ all the non-trivial equilibrium configurations of the path $\mathcal{B}_1$, due to condition (N_2);

$\diamond$ all the non-trivial equilibrium configurations of the path $\mathcal{A}_1$, due to condition (N_2), when $q_1 < 1$;

$\diamond$ the non-trivial equilibrium configurations associated to a negative slope in the $\theta_{\bar{l}} - P$ plane (snap-through instability) of the path $\mathcal{A}_1$, due to condition (N_2), and occurring only when $1 < q_1 < q^{ST} \approx 1.6875$.

All other non-trivial equilibrium configurations not listed above satisfy the necessary conditions (N_1 and N_2) and therefore *could* be stable, although this cannot be proven and remains an open problem. However, although stability for these cases cannot –for the moment– be rigorously decided, the stability of the non-trivial equilibrium configurations $\mathcal{A}_1$ has been experimentally confirmed (see the experimental results presented in the next section).

Finally, it is straightforward to judge the stability of the system in the case when the axial spring is absent ($k = 0$, Fig. 5.6) and conclude that, although

the auxiliary function $\Gamma(s)$ is always bounded, all the possible equilibrium configurations are unstable due to condition (N_2).

5.4 Theoretical behaviour of the blade

The buckling loads of the structure sketched in Fig. 5.1 are given by equation (5.12). Moreover, for a given value of the applied load P, λ is known from its definition ($\lambda^2 = P/B$), so that equation (5.35) allows the calculation of the corresponding η and thus l_{eq} is known from equation $(5.34)_4$. Finally, equation (5.40) give the components of the elastica and, in particular, equation (5.41) permit the evaluation of the displacement components of the blade's end point. Instability (stability) of the configurations has been determined using condition N (condition S) obtained in Section 5.3. As we have already mentioned in that section, the stability of the ascending branches of the first-mode of postcritical behaviour (where the necessary condition for stability is verified) has been *only conjectured* on the basis of our experimental results, while stability and instability of all the rest of the trivial and bifurcated paths has been rigorously proven.

Restricting the attention for the moment only to the first bifurcation mode of the structure shown in Fig. 5.1, the dimensionless load $p = P/(k\bar{l})$ is plotted as a function of the dimensionless displacement components $\{x_1(s = \bar{l}) = u_1(\bar{l})/\bar{l}, \, x_2(s = \bar{l}) = u_2(\bar{l})/\bar{l}, \, \theta_{\bar{l}}\}$ in Fig. 5.9, for different values of the dimensionless stiffness q_1, taken equal to 0.7, 1.1, and 2. Note that solid (dashed) lines represent stable (unstable) configurations.

The following observations can be drawn.

⋄ The upper part of Fig. 5.9 is relative to $q_1 = 0.7$. In this case, no bifurcation occurs and the blade rigidly penetrates into the sliding sleeve. Note that alternative (and unstable) equilibrium configurations exist in addition to the trivial straight configuration, but (with the exception of the figure on the left, which can give a false impression of bifurcation) they do not cross (and even 'touch') the trivial path, so that these non-trivial unstable configurations cannot spontaneously be reached by the system.

⋄ Both the central and the lower parts of Fig. 5.9 show *two bifurcation loads associated to the first bifurcation mode* and show the *restabilization of the straight configuration* after the second buckling load.

⋄ The central part of Fig. 5.9, referred to $q_1 = 1.1$, shows an example of a descending path of the lower equilibrium branch, associated to a snap-through of the system. On the other hand, the lower part of Fig. 5.9, referred to $q_1 = 2$, shows that the lower equilibrium branch has always a positive slope (so that snap-through does not occur).
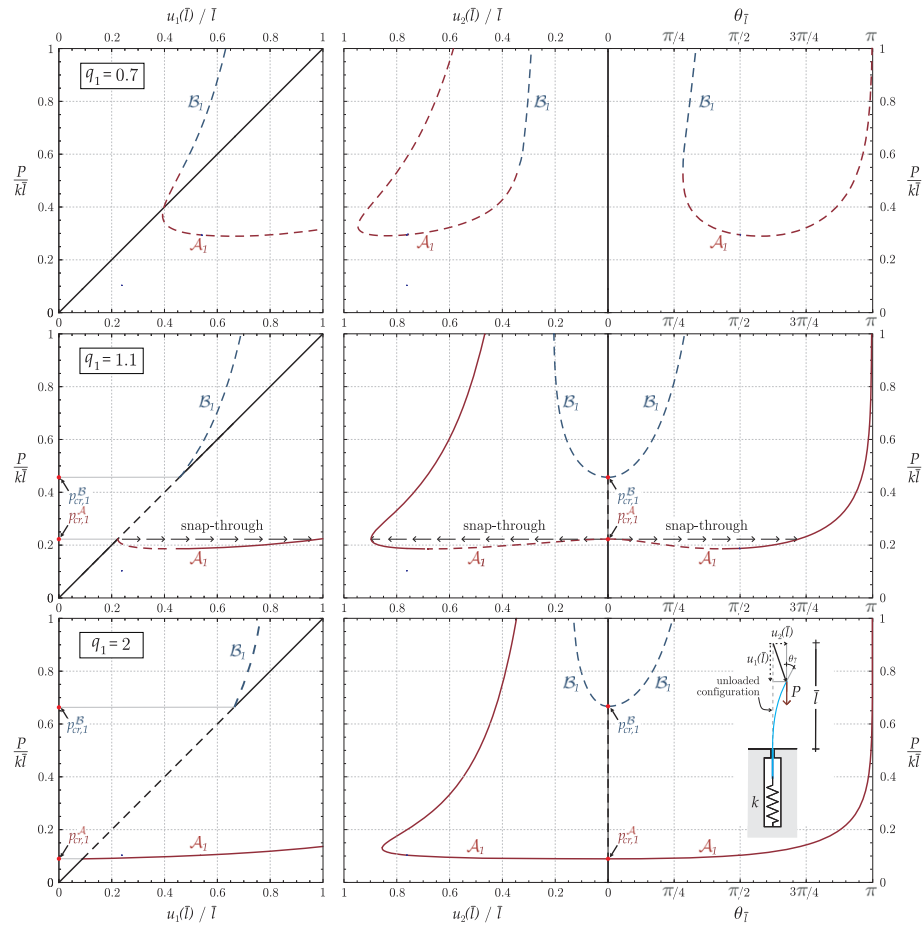
95

Figure 5.9: First-mode of bifurcation: deformation paths of the structure sketched in the inset, expressed as the (dimensionless) applied load versus (dimensionless) displacement components and rotation of the blade loaded edge.
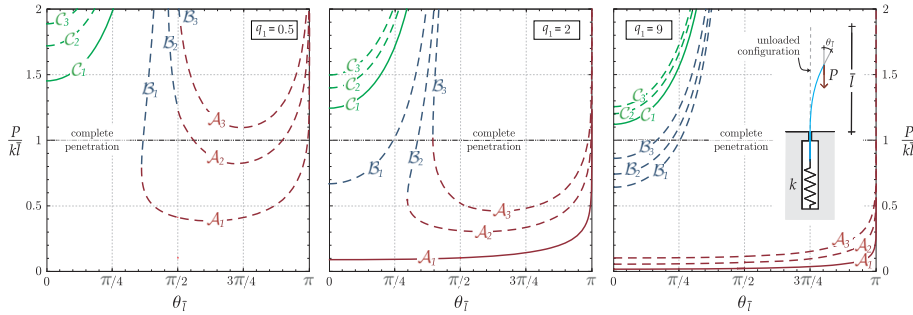
Figure 5.10: Force vs. blade's edge rotation of the structure sketched in the inset, evidencing the first, second and third mode of bifurcation. The threshold marked as 'complete penetration' corresponds to the complete penetration of the blade into the sliding sleeve. In the example on the left there is no bifurcation, while in the central part of the figure only the first mode is involved. In the part of the figure on the right first, second and third mode of bifurcation may occur before the 'complete penetration' is attained.

⋄ Comparing the central and the lower parts of Fig. 5.9 we may observe that *an increase in the stiffness of the system decreases the buckling load and increases the restabilization load.*

⋄ The fact that a vertical *Eshelby-like force is generated and 'expels' the blade from the sliding sleeve after buckling* is not directly visible in Fig. 5.9. The visualization of this effect requires plotting P as a function of l_{eq}, which is done in Fig. 5.12 where comparison with experiments is presented.

An example of bifurcation paths involving the first, the second and the third mode is reported in Fig. 5.10, where the load P (made dimensionless through division by $k\bar{l}$) is plotted as a function of the rotation of the loaded end of the blade, $\theta_{\bar{l}}$. In the three parts of Fig. 5.10, referring (from left to right) to q_1 equal to 0.5, 2, and 9, a line denoted as 'complete penetration' is reported at the value of parameter $p = P/(k\bar{l}) = 1$, corresponding to the complete penetration of the blade into the sliding sleeve. Therefore, curves reported beyond that limit are mathematically corrected, but meaningless from mechanical point of view. A situation where the postcritical paths do not intersect the vertical axis (corresponding to stable equilibrium only for the trivial straight configuration), and thus bifurcation does not occur, is reported in the left part of the figure, $q_1 = 0.5$. Here, first- and second-mode non-trivial unstable configurations exist below the 'complete penetration' limit but these cannot be reached during loading of the system. Bifurcation is possible in the central, $q_1 = 2$, and right, $q_1 = 9$, parts of the figure. While only first mode bifurcations occur in the former case, in the latter case first, second and third modes bifurcations are possible. In general, all modes superior to the first have been always found unstable in all cases analyzed
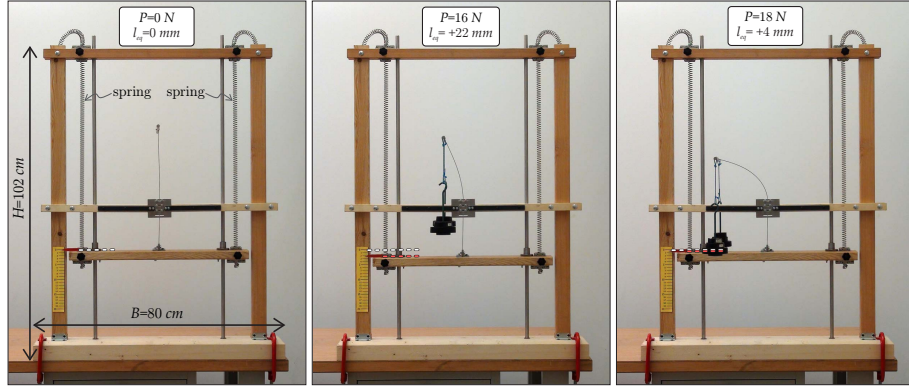
Figure 5.11: The unloaded configuration (left) and two deformed configurations (center and right) of Prototype 0. At high load (right) the base of the structure has an upward rigid translation when compared with the configuration at low load (center), a clear indication of the presence of the Eshelby-like force.

(not only in those reported in this section).

5.5 Experiments

An essential part in the present study is to show that all the found mechanical behaviours can be realized in practice. To this purpose, we have designed, realized and tested model structures to verify the theoretical findings. We have already anticipated with Figs. 5.5–5.6 that the theory has been fully confirmed, so that the intention is now to provide quantitative support.

Two prototypes (called 'Prototype 0', see Fig. 5.11, and 'Prototype 1', Fig. 5.2, right) of the structure sketched in Fig. 5.1 have been realized, according to the design scheme shown in Fig. 5.2 (left).

⬦ **Prototype 0**. It has been realized (Fig. 5.11) to provide a qualitative experimental validation of the features displayed by the mechanical system shown in Fig. 5.1. Two blades have been employed (with lengths 250 mm and 200 mm), both realized with a C62 carbon-steel strip (25 mm × 1 mm cross section). The sliding sleeve, 31 mm in length, has been realized with three pairs of rollers (15 mm diameter teflon cylinders, each containing two roller bearings). Three pairs of carbon steel (EN 10270-1 SH) springs (D19060, 0.8 mm wire diameter and 5 mm mean coil diameter; D19130, 1.6 mm wire diameter and 12.5 mm mean coil diameter; D19100, 1.25 mm wire diameter and 8 mm mean coil diameter all purchased from D.I.M.) have been used. The two linear bushings (LHFRD12) used to maintain horizontal the bar to which the blade is clamped have been purchased from Misumi Europe. Load has been controlled by manually imposing given weights.

⋄ **Prototype 1**. The linear elastic spring represented in Fig. 5.1 has been realized by hanging a highly-stiff horizontal bar (to which the elastic blade is clamped) with two metal springs. The horizontal bar can only rigidly translate as constrained by two linear bushings (LHFRD12, Misumi Europe). The dead load at the end of the blade has been imposed by filling (at a constant rate of 10 g/s) two containers with water and has been measured with two miniaturized Leane XFTC301 (R.C. 500N) load cells. Five blades have been employed (lengths: 600 mm, 530 mm, 510 mm, 430 mm, and 360 mm) with the 'stiff' springs and four blades (lengths: 600 mm, 530 mm, 510 mm and 430 mm) with the 'compliant' one, all realized with C62 carbon-steel strips (25 mm × 2 mm cross section) in the experiments performed with Prototype 1 (Fig. 5.2, on the right). For these blades the bending stiffness B has been determined with flexure experiments to be equal to 2.70 Nm². The same sliding sleeve employed by Bigoni et al. (2013) has been used, which is 384 mm in length and has been realized with 32 pairs of rollers (made up of 10 mm diameter and 15 mm length teflon cylinders, each containing two roller bearings). The tolerance between the metal strip and the rollers can be calibrated with four micrometrical screws and have been set to be 0.1 mm. Two pairs of carbon steel (EN 10270-1 SH) springs (the so-called 'stiff': D19130, 1.6 mm wire diameter and 12.5 mm mean coil diameter, k=600 N/m; and the so-called 'compliant': D19100 1.25 mm wire diameter and 8 mm mean coil diameter, k=540 N/m, purchased from D.I.M.) have been used. The penetration length l_{eq} has been obtained by measuring the displacement of the lower edge of the blade through a magnetic noncontact displacement transducer GC-MK5 (from Gemac).

Both prototypes have fully confirmed the theory, although Prototype 0 only in a qualitative way, so that Prototype 1 has been later manufactured to obtain quantitative results.For both Prototypes 0 and 1, all the experimental tests have been performed in a controlled temperature (20±0.2°C) and humidity (48±0.5%) room and data have been acquired with a NI CompactDAQ system, interfaced with Labview 8.5.1 (National Instruments). Furthermore, photos have been taken with a Sony NEX 5N digital camera, equipped with 3.5-5.6/18-55 lens (optical steady shot from Sony Corporation) and movies have been recorded during the tests with a Sony handycam (model HDR-XR550VE).

Experimental results, expressed in terms of applied load P (measured in N) as a function of the amount of blade internal to the sliding sleeve, l_{eq} (measured in cm), are reported in Fig. 5.12. Results reported on the left refer to 'compliant' spring, $k = 540N/m$, while result reported on the right to the 'stiff' one, $k = 600N/m$. Four blades of different length have been used in the former case, five in the latter. Experimental results (solid lines) have
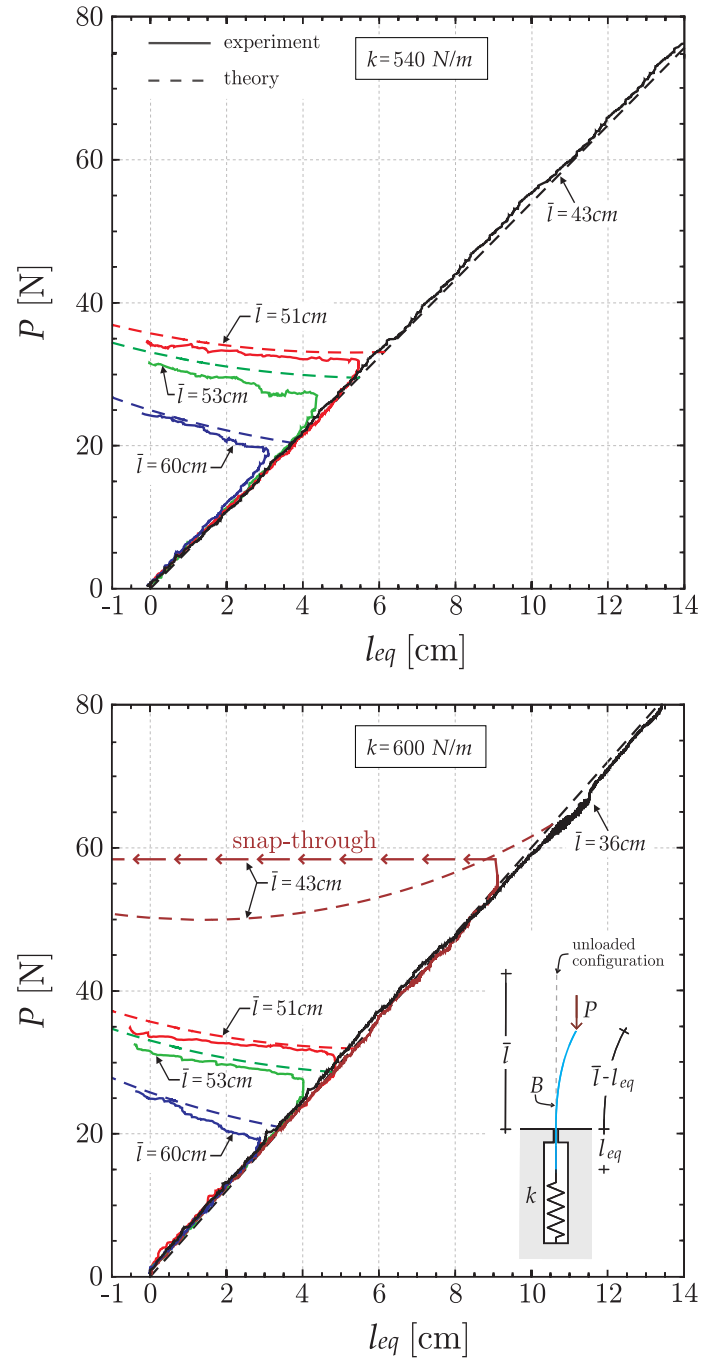
Figure 5.12: Comparison of theoretical and experimental results obtained with the set-up shown in Fig. 5.2.

been reported in the figures together with theoretical predictions (dashed lines). For both spring stiffnesses, the blades with shortest length show a pure translation without buckling, while buckling has been observed for all the other lengths. A snap-through behaviour was theoretically predicted for $\bar{l} = 51$ cm of the 'compliant' spring case and for $\bar{l} = 43$ cm of the 'stiff' spring case. In the former case ($\bar{l} = 51$ cm) the descending postcritical path is so short and weakly inclined that it becomes hardly visible in the graph and therefore the snap-through has not been experimentally observed. On the other hand, in the latter case ($\bar{l} = 43$ cm) the snap-through has been so violent that the experiment has been immediately interrupted and subsequent data have not been measured.

A very nice agreement between theory and experiments (fully confirming the presence of the Eshelby-like force) can be noted from Fig. 5.12, with departures from the straight configuration observed to occur slightly before the theoretical loads for buckling, which is nothing but the usual effect of the imperfections (see for instance Bigoni et al. [51]). Experiments clearly show that the blade is ejected from the sliding sleeve (which corresponds to a decrease in l_{eq}) during the postcritical behaviour of the structure.

Movies of the experiments can be found at http://ssmg.unitn.it//blade.html.

5.6 Blade with different boundary conditions

In this section will be briefly shown the governing equations for the blade with different boundary conditions at its right edge (clamped, clamped in rotation and simply supported), while the other edge remains constrained by a linear spring of stiffness k and can slide into a perfect smooth and frictionless sleeve. These systems are similar to those extensively analyzed in Chapter 2, so that we cross-refer to them for details.

5.6.1 Clamped blade

Let us consider the system in Fig. (5.13), where an inextensible elastic planar rod is forced to penetrate a sliding sleeve, restrained by an axial linear spring of stiffness k, through the application of a dead compressive load P at the other edge, which is constrained by a movable clamp.

Considering only the outer part of the beam at an equilibrium configuration, under the assumption that the inner part of the blade would not buckle, since the elastica configuration of the inner part is completely defined by the kinematic constraint $\theta(s) = 0$ for $s \in [0, l_{eq}]$, the rotation field at equilibrium $\theta_{eq}(s)$ is unknown only for the outer part, so that, introducing the normalized axial load $\lambda^2 = P/B$, it is a solution of the following differential problem
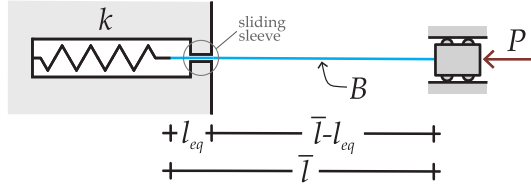
Figure 5.13: The penetrating blade in an equilibrium configuration with a movable clamped end subjected to a dead load P. The system can slide into a frictionless channel and is restrained by a spring of stiffness k coaxial to the elastic planar rod.

$$\begin{cases} \dfrac{\mathrm{d}^2\theta_{eq}(s)}{\mathrm{d}s^2} + \lambda^2 \sin\theta_{eq}(s) = 0, & s \in \left(l_{eq}, \bar{l}\right) \\[2mm] \theta_{eq}\left(l_{eq}\right) = \theta_{eq}\left(\bar{l}\right) = 0, \\[2mm] \dfrac{\mathrm{d}\theta_{eq}(s)}{\mathrm{d}s}\bigg|_{s=\frac{\bar{l}+3l_{eq}}{4}} = 0, \\[2mm] \lambda^2 = \dfrac{k}{B}l_{eq} + \dfrac{1}{2}\left[\theta'_{eq}(l_{eq})\right]^2, \end{cases} \tag{5.59}$$

where the curvature is null for $s = (\bar{l} + 3l_{eq})/4$ and $s = (3\bar{l} + l_{eq})/4$, but only the former condition will be used because, thanks to the symmetry of the problem, only the first quarter of the outer blade will be considered, as in Section 2.2.3. For conciseness, only the first bifurcation mode will be analyzed, but relations for superior (unstable) modes may be determined following Section 2.2.3. The rotation at the inflection point is $\theta_{eq}\left(\dfrac{\bar{l}+3l_{eq}}{4}\right) = \theta_q$ and, through change of variables and Riemann theorem, integration of the differential problem (5.59) leads to the relation between load parameter λ and the angle θ_q

$$4\mathcal{K}\left(\sin\frac{\theta_q}{2}\right) = \lambda\left[\bar{l} - \lambda^2\frac{B}{k}\left(1 - 2\sin^2\frac{\theta_q}{2}\right)\right]. \tag{5.60}$$

From equation (5.60) can be observed that the relation $P - \theta_q$ is equal to the behaviour $P - \theta_{\bar{l}}$, obtained through equation (5.35), except for the value of the stiffness parameter for which there is no buckling, that is now $q_1^q < 27\pi^2\dfrac{k\bar{l}^3}{B}$.

The analytical form for the axial and transverse equations describing the shape of the elastica of the outer part of the blade $s \in \left(l_{eq}, \bar{l}\right)$ is obtained by integration of equation (5.15) as

$$x_1(s) = -s + \frac{2}{\lambda} E \left[\text{am} \left(\lambda \left(s - l_{eq} \right), \sin \frac{\theta_q}{2} \right), \sin \frac{\theta_q}{2} \right] - l_{eq},$$

$$x_2(s) = \frac{2}{\lambda} \sin \frac{\theta_q}{2} \left[1 - \text{cn} \left(\lambda \left(s - l_{eq} \right), \sin \frac{\theta_q}{2} \right) \right].$$

(5.61)

5.6.2 Blade clamped in rotation

The differential problem governing the behaviour of the system reported in Fig. (5.14), where the elastic blade is constrained in rotation at its loaded edge, is

$$\begin{cases} \dfrac{\mathrm{d}^2 \theta_{eq}(s)}{\mathrm{d}s^2} + \lambda^2 \sin \theta_{eq}(s) = 0, \qquad s \in \left(l_{eq}, \bar{l} \right) \\[2mm] \theta_{eq} \left(l_{eq} \right) = \theta_{eq} \left(\bar{l} \right) = 0, \\[2mm] \dfrac{\mathrm{d}\theta_{eq}(s)}{\mathrm{d}s} \bigg|_{s = \frac{\bar{l} + l_{eq}}{2}} = 0, \\[2mm] \lambda^2 = \dfrac{k}{B} l_{eq} + \dfrac{1}{2} \left[\theta'_{eq}(l_{eq}) \right]^2, \end{cases}$$

(5.62)

where the rotation at the inflection point (midspan of the outer part of the elastic rod, namely $s = (\bar{l} + l_{eq})/2$ is named θ_m. For this system, the relation between the dimensionless load parameter λ and the rotation at the rod's midspan θ_m, for the first buckling mode, is written as

$$2\mathcal{K} \left(\sin \frac{\theta_m}{2} \right) = \lambda \left[\bar{l} - \lambda^2 \frac{B}{k} \left(1 - 2 \sin^2 \frac{\theta_m}{2} \right) \right].$$

(5.63)

Equation (5.63) is similar to equation (5.35) referred to the blade with one free edge, except for the value of the stiffness parameter for which there is no buckling, that is now $q_1^m < \dfrac{27\pi^2}{4} \dfrac{k\bar{l}^3}{B}$. The analytical form for the axial and transverse displacements of this system, from which it is possible to calculate the shape of any deformed configurations, is the same reported in equation (5.61).

5.6.3 Simply supported blade

Let us consider the system in Fig. (5.15), where the elastic blade is simply supported in its loaded edge and may slide into the frictionless sliding sleeve. An axial spring of stiffness k restrains the other edge of the planar rod.

Considering only the outer part of the beam, under the assumption that the inner part of the blade would not buckle, the rotation field $\theta(s)$ is obtained
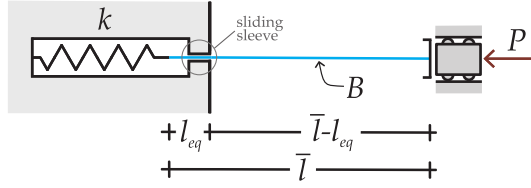
Figure 5.14: The penetrating blade in an equilibrium configuration clamped in rotation at its loaded edge. The system can slide into a frictionless channel and is restrained by a spring of stiffness k coaxial to the elastic planar rod.
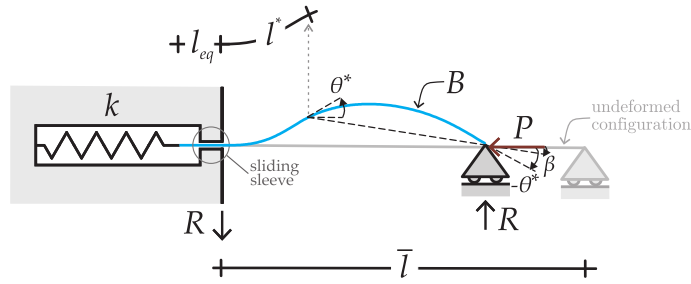
Figure 5.15: The penetrating blade in a deformed equilibrium configuration, where its loaded edge is simply supported, while the other edge slides into a frictionless channel and it is restrained by a spring of stiffness k. At the curvilinear coordinate $s = l^*$ exists an inflection point and the rotation angle is denoted with $\theta(s = l^*) = \theta^*$. The angle β defines the inclination with respect the horizontal direction of the resultant between the applied dead load P and the vertical reaction of the support R.

through the following differential problem

$$
\begin{cases}
\dfrac{\mathrm{d}^2\theta_{eq}(s)}{2} + \dfrac{P}{B}\sin\theta_{eq}(s) + \dfrac{R}{B}\sin\theta_{eq}(s) = 0, \qquad s \in \left(l_{eq}, \bar{l}\right) \\[2mm]
\theta_{eq}\left(l_{eq}\right) = 0, \\[2mm]
\left.\dfrac{\mathrm{d}\theta_{eq}(s)}{\mathrm{d}s}\right|_{s=\bar{l}} = 0, \\[2mm]
\displaystyle\int_0^{\bar{l}} \sin\theta(s)\mathrm{d}s = 0, \\[2mm]
\dfrac{\sqrt{P^2 + R^2}}{B} = \dfrac{k}{B}l_{eq} + \dfrac{1}{2}\left[\theta'_{eq}(l_{eq})\right]^2.
\end{cases}
\tag{5.64}
$$

Introducing the normalized load $\gamma^2 = \sqrt{P^2 + R^2}/B$ and the angle $\psi(s) = \theta_{eq}(s) + \beta$, where β is the angle of the resultant between P and R as in

104

Fig. 5.15, the differential problem (5.64) is rewritten as

$$
\begin{cases}
\dfrac{\mathrm{d}^2\psi(s)}{\mathrm{d}s^2} + \gamma^2 \sin\psi(s) = 0, \qquad s \in \left(l_{eq}, \bar{l}\right) \\[2mm]
\psi\left(l_{eq}\right) = \beta, \\[2mm]
\left.\dfrac{\mathrm{d}\psi(s)}{\mathrm{d}s}\right|_{s=\bar{l}} = 0, \\[2mm]
\displaystyle\int_0^{\bar{l}} \sin\left(\psi(s) - \beta\right)\mathrm{d}s = 0, \\[2mm]
\dfrac{\sqrt{P^2 + R^2}}{B} = \dfrac{k}{B}l_{eq} + \dfrac{1}{2}\left[\psi'\left(l_{eq}\right)\right]^2.
\end{cases}
\tag{5.65}
$$

Similarly to antisymmetric buckling modes of doubly clamped rod, analyzed in Section 2.2.3, it is a standard expedient to operate the following change of variables

$$
\eta = \sin\frac{\psi^*}{2}, \qquad \eta\sin\omega(s) = \sin\frac{\psi(s)}{2},
\tag{5.66}
$$

where $\psi^* = \theta^* + \beta$. Integration of differential problem (5.65) leads to the non-trivial for θ^*, related to the dimensionless load parameter γ and the angle β for the first bifurcation mode

$$
3\mathcal{K}\left(\eta\right) - \mathcal{K}\left(\eta, \omega_\beta\right) = \gamma\left[\bar{l} - \gamma^2\frac{B}{k}\left(1 - 2\eta^2\right)\right],
\tag{5.67}
$$

where $\omega_\beta = \arcsin\left(\eta^{-1}\sin\left(\dfrac{\beta}{2}\right)\right)$. Using dimensionless parameters $p = \dfrac{P}{k\bar{l}}$ and $q_1^* = \dfrac{27\pi^2}{2}\dfrac{k\bar{l}^3}{B}$ (so that, for $q_1^* < 1$ the system does not show bifurcation) it is possible to rewrite equation (5.68) in the following form

$$
pq_1^*\left(1 - p\left(1 - 2\eta^2\right)\right)^2 = \left(1 - 2\sin^2\frac{\beta}{2}\right)\left[3\mathcal{K}(\eta) - \mathcal{K}\left(\eta, \omega_\beta\right)\right]^2.
\tag{5.68}
$$

Since only this equation is not sufficient to define a relation between the load P and the kinematic parameter θ^*, we have to use condition $(5.64)_4$ in order to provide a correspondence between θ^* and β, which is written, similarly to equation (2.89) reported in Section 2.2.3, as

$$
-2\eta\cos\omega_\beta\left(1 - 2\eta^2\sin^2\omega_\beta\right)
$$

$$
+2\eta\sin\omega_\beta\sqrt{1 - \eta^2\sin^2\omega_\beta}\left\{3\left[2E(\eta) - K(\eta)\right] - 2E(\omega_\beta, \eta) + K(\omega_\beta, \eta)\right\} = 0.
\tag{5.69}
$$

Equations (5.68) and (5.69) are highly non-linear and represent the non-trivial solution. The relation between β and θ^* (the former contained in ω_β and the latter in η) can be numerically obtained from equation (5.69) and used into equation (5.68) to have the relation $P - \theta^*$. Finally, from integration of the kinematic fields (5.15) we are able to write the analytical form for the axial and transverse displacements of the outer part of the blade $s \in \left(l_{eq}, \bar{l}\right)$ as

$$
\begin{aligned}
x_1(s) = {}& + \sin\beta \left[-\frac{2\eta}{\gamma}\mathrm{cn}\big(\gamma\,(s - l_{eq}) + \mathcal{K}(\omega_\beta,\eta),\eta\big) + \frac{2\eta}{\gamma}\mathrm{cn}\big(\mathcal{K}(\omega_\beta,\eta),\eta\big) \right] \\
& \cos\beta \Big\{ -s + \frac{2}{\gamma}\big[E\left[\mathrm{am}\left(\gamma\,(s) + \mathcal{K}(\omega_\beta,\eta),\eta\right),\eta\right] \\
& - E\left[\mathrm{am}\left(\mathcal{K}(\omega_\beta,\eta),\eta\right),\eta\right] \big] \Big\},
\end{aligned}
$$

$$
\begin{aligned}
x_2(s) = {}& \cos\beta \left[-\frac{2\eta}{\gamma}\mathrm{cn}\big(\gamma\,(s) + \mathcal{K}(\omega_\beta,\eta),\eta\big) + \frac{2\eta}{\gamma}\mathrm{cn}\big(\mathcal{K}(\omega_\beta,\eta),\eta\big) \right] \\
& - \sin\beta \Big\{ -s + \frac{2}{\gamma}\big[E\left[\mathrm{am}\left(\gamma\,(s) + \mathcal{K}(\omega_\beta,\eta),\eta\right),\eta\right] \\
& - E\left[\mathrm{am}\left(\mathcal{K}(\omega_\beta,\eta),\eta\right),\eta\right] \big] \Big\}.
\end{aligned}
$$

$$
(5.70)
$$

5.7 The imperfect blade and its self-restabilization

In the following the effects of imperfections on the behaviour of the penetrating blade will be considered. In particular, defect of tilt angle α and initial constant curvature χ_0 are analyzed through both theoretical and experimental approaches, showing that, for some values of the dimensionless stiffness q_1 and imperfection parameters, a monotonic increase of the load P concurs to an increase and then a decrease of inflection, until the rod tends to return in its straight configuration when it is completely penetrated into the sleeve, revealing the *asymptotic* nature of the *self-restabilization*.

5.7.1 Penetrating blade with an imperfection of angle

An inextensible elastic planar rod with bending stiffness B and total length $\bar{l}$ is allowed to slide into a frictionless sliding sleeve with a linear spring of stiffness k at its end. The other edge of the beam is loaded through a dead vertical compressive load P, see Fig. 5.16 (left). The system can be considered *geometrically imperfect* because of its initial tilt angle α respect the vertical position, so that by varing the imperfection parameter α we can obtain a family of imperfect systems that may eventually degenerate to the perfect system when $\alpha \to 0$ (Section 5.2.1).
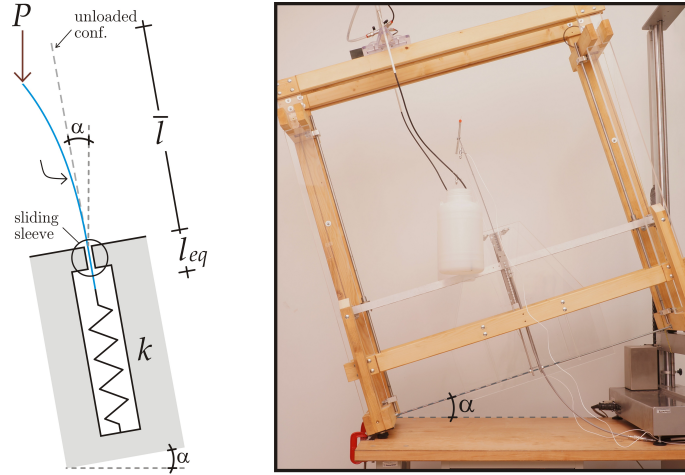
Figure 5.16: The elastic planar rod of constant bending stiffness B has a free end subject to the dead load P, while the other edge of the blade slides into a frictionless sleeve and is restrained by an axial linear spring of stiffness k. The length of the blade inside the sliding sleeve at equilibrium is l_{eq}, while the total length of the rod in its unloaded configuration is $\bar{l}$. The system is made imperfect because of the presence of a tilt angle defect α. The design scheme is reported on the left, while for the experiments the prototype 1 (Section 5.5) has been used, inclined through the movable beam of an electromechanical tension-compression machine, as visible on the right.

Total potential energy and equilibrium equations

Introducing the curvilinear coordinate $s \in [0; \bar{l}]$ and the rotation $\theta(s)$ of the plane rod's axis, since l_{in} is the segment of the rod inserted into the perfectly smooth and bilateral sliding sleeve, it follows that $\theta(s) = 0$ for $s \in [0; l_{in}]$. Denoting by a prime the derivative with respect to s, the total potential energy of the system is

$$\mathcal{V}(\theta, l_{in}) = \int\limits_{l_{in}}^{\bar{l}} B \frac{\left[\theta'(s)\right]^2}{2} \mathrm{d}s + \frac{1}{2} k \left(l_{in}\right)^2 - P \left[\cos\alpha \left(\bar{l} - \int\limits_{l_{in}}^{\bar{l}} \cos\theta(s)\mathrm{d}s \right) \right.$$

$$\left. + \sin\alpha \int\limits_{l_{in}}^{\bar{l}} \sin\theta(s)\mathrm{d}s \right].$$

(5.71)

Following the calculus of variations adopted in Section 5.2, the compatibility equations (5.23) and the boundary conditions (5.20) and (5.21) are used together with Leibniz rule of differentiation and integration by part, in

order to arrive at the first variation of the functional $\mathcal{V}$

$$
\begin{aligned}
\delta_\epsilon \mathcal{V} = -\int_{l_{eq}}^{\bar{l}} & \left[B\theta''_{eq} + P\big(\cos\alpha\sin\theta_{eq}(s) + \sin\alpha\cos\theta_{eq}(s)\big) \right] \theta_{var}(s)\mathrm{d}s \\
& + \left[kl_{eq} - P + \frac{B}{2}\theta'_{eq}(l_{eq})^2 \right] l_{var},
\end{aligned}
\tag{5.72}
$$

from which, imposing the vanishing of equation (5.72) for any admissible variations $\theta_{\mathrm{var}}(s)$ and l_{var}, the differential equilibrium equation for the elastica with a moving boundary l_{eq} is obtained as

$$
\begin{aligned}
& \theta''_{\mathrm{eq}}(s) + \lambda^2 \left(\cos\alpha\sin\theta_{\mathrm{eq}}(s) + \sin\alpha\cos\theta_{\mathrm{eq}}(s) \right) = 0, \qquad s \in \left(l_{\mathrm{eq}}, \bar{l} \right) \\
& l_{\mathrm{eq}} = \frac{B}{k} \left(\lambda^2 \cos\alpha - \frac{1}{2} \left[\theta'_{\mathrm{eq}}(l_{\mathrm{eq}}) \right]^2 \right),
\end{aligned}
\tag{5.73}
$$

where the load parameter $\lambda^2 = P/B$ has been introduced. Operating in a standard manner following Section 3.1.3, the introduction of the auxiliary angle $\varphi(s) = \theta_{eq}(s) + \alpha$, together with the change of variables (3.29), leads to the non-trivial solution for η, related to the rotation of the free end $\theta_{\bar{l}}$ by means of equation $(3.29)_1$ and the tilt angle α, as a function of the load parameter λ

$$
\mathcal{K}(\eta) - \mathcal{K}(m, \eta) = \lambda \left[\bar{l} - \lambda^2 \frac{P}{k} \left(1 - 2\eta^2 \right) \right],
\tag{5.74}
$$

where $m = \arcsin\left[\dfrac{\sin\dfrac{\alpha}{2}}{\eta} \right]$ and $\eta = \sin\dfrac{\theta_{\bar{l}} + \alpha}{2}$. Recalling the definition of the dimensionless load p and the dimensionless relative stiffness for the first mode q_1 (spring stiffness multiplied by the bar length and divided by a critical load) as

$$
p = \frac{P}{k\bar{l}}, \qquad q = \frac{16k\bar{l}^3}{27\pi^2 B},
\tag{5.75}
$$

the solution (5.74) can be rewritten in the form

$$
(1 - 2\eta^2)^2 p^3 - 2(1 - 2\eta^2)p^2 + p - \frac{16}{27\pi^2 q} \left[\mathcal{K}(\eta) - \mathcal{K}(m, \eta) \right]^2 = 0,
\tag{5.76}
$$

which is a cubic equation providing three equilibrium paths $p^{\mathcal{A}}; p^{\mathcal{B}}; p^{\mathcal{C}}$ corresponding to the first mode. One of these paths, namely $\mathcal{C}$, has no physical meaning because the rod is already penetrated into the sliding sleeve, since $p^{\mathcal{C}} > 1$. The other two paths, namely $\mathcal{A}$ and $\mathcal{B}$, are plotted in Fig. 5.17 (left) as a function of the free end rotation $\theta_{\bar{l}}$ for $q = 0.5$, showing that *asymptotic self-restabilization* occurs for $\alpha = 10°$, whereas it does not happen
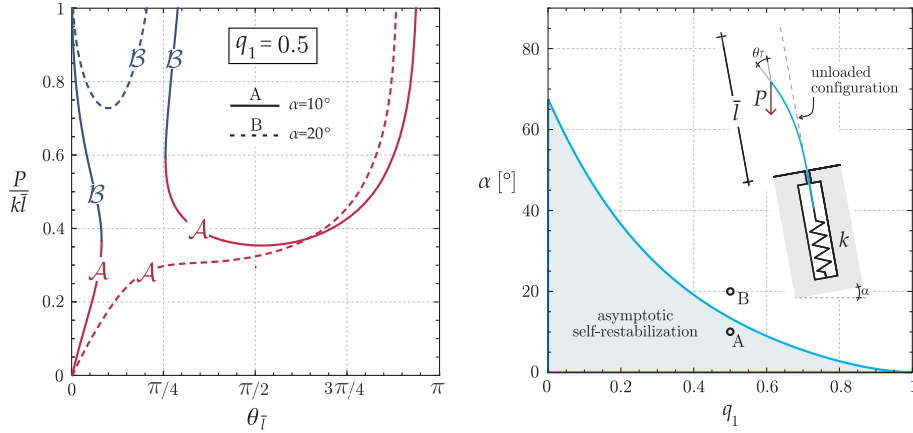
Figure 5.17: Left: equilibrium paths $\mathcal{A}$ and $\mathcal{B}$ expressed as the dimensionless applied load p versus rotation of the blade loaded edge $\theta_{\bar{l}}$ for dimensionless relative stiffness $q = 0.5$ and imperfection angles $\alpha = \{10; 20\}°$. Right: region in the plane $q - \alpha$ where asymptotic self-restabilization of the system is possible. Two dots that corresponds to the deformed paths shown in the left graph, $\alpha = 10°$ (A) and $\alpha = 20°$ (B), are reported for $q = 0.5$.

for $\alpha = 20°$. This means that for some particular values of the parameters q and α a monotonic increase of the vertical dimensionless dead load p implies firstly an increase and then a decrease of inflection up to the initial straight configuration, in the limit of blade's complete penetration inside the sliding sleeve ($p \to 1$). The restabilization phenomenon is characterized by the join of paths $\mathcal{A}$ and $\mathcal{B}$, or it can be analytically recognized if $p^{\mathcal{A}}$ is not defined for all values of the kinematic parameter $\theta_{\bar{l}} \in [0; 180° - \alpha]$. Through this criterion a 'restabilization' zone has been discovered in the plane $q - \alpha$, as reported in Fig. 5.17 (right).

The rotational field $\theta_{\text{eq}}(s)$ can be expressed through inversion of relation $(3.29)_1$ as

$$\theta(s) = 2 \arcsin \left[\eta \operatorname{sn} \left(\lambda \left(s - l_{eq} \right) + \mathcal{K} \left(m, \eta \right), \eta \right) \right] - \alpha. \qquad (5.77)$$

from which the axial and transverse equations describing the shape of the

elastica are obtained by integration of equation (5.15) as

$$
\begin{aligned}
x_1(s) = {}& -\frac{2\eta}{\lambda}\sin\alpha\Big\{\mathrm{cn}\big(\lambda\,(s-l_{eq})+\mathcal{K}(m,\eta),\eta\big)-\mathrm{cn}\big(\mathcal{K}(m,\eta),\eta\big)\Big\}-l_{eq} \\
& \cos\alpha\Big\{-s+\frac{2}{\lambda}\Big[E\big[\mathrm{am}\big(\eta\,(s-l_{eq})+\mathcal{K}(m,\eta),\eta\big)\big] \\
& -E\big[\mathrm{am}\big(\mathcal{K}(m,\eta),\eta\big)\big]\Big]\Big\},
\end{aligned}
$$

$$
\begin{aligned}
x_2(s) = {}& \frac{2\eta}{\lambda}\cos\alpha\Big\{\mathrm{cn}\big(\lambda\,(s-l_{eq})+\mathcal{K}(m,\eta),\eta\big)-\mathrm{cn}\big(\mathcal{K}(m,\eta),\eta\big)\Big\} \\
& +\sin\alpha\Big\{-s+\frac{2}{\lambda}\Big[E\big[\mathrm{am}\big(\lambda\,(s-l_{eq})+\mathcal{K}(m,\eta),\eta\big)\big] \\
& -E\big[\mathrm{am}\big(\mathcal{K}(m,\eta),\eta\big)\big]\Big]\Big\},
\end{aligned}
\tag{5.78}
$$

where the functions am, cn and sn denote the Jacobi amplitude, Jacobi cosine amplitude and Jacobi sine amplitude functions while $E(x,\eta)$ is the incomplete elliptic integral of the second kind of modulus η. Equations (5.78) can be evaluated at the loaded end, providing the following axial and transverse displacement of the free edge of the blade

$$
\begin{aligned}
u_1\left(\bar{l}\right) = {}& \frac{1}{\lambda}\Big\{2\eta\sin\alpha\cos m+\cos\alpha\big[2E\left(\eta\right)-2E\left(m,\eta\right)+\mathcal{K}\left(m,\eta\right)-\mathcal{K}\left(\eta\right)\big] \\
& +\mathcal{K}\left(m,\eta\right)-\mathcal{K}\left(\eta\right)\Big\}-l_{eq},
\end{aligned}
$$

$$
u_2\left(\bar{l}\right) = \frac{1}{\lambda}\Big\{2\eta\cos\alpha\cos m+\sin\alpha\big[2E\left(m,\eta\right)-2E\left(\eta\right)+\mathcal{K}\left(\eta\right)-\mathcal{K}\left(m,\eta\right)\big]\Big\},
\tag{5.79}
$$

Equations (5.74) and (5.79) reveal the response of the system as a function of the dimensionless load p, for different values of the relative stiffness parameter q_1. In particular, from Fig.5.18 can be noticed that

⋄ for $q < 1$ *asymptotic self-restabilization* may occur if the value of imperfection angle α belongs to the coloured area in Fig.5.17. For these values the rod 'spontaneously' return, for a monotonic increase of p, in the straight configuration when $p \to 1$ (upper part of Fig. 5.18, for $q = 0.7$ and $\alpha = 5°$). If the values of q and α do not belong to the coloured area, *asymptotic self-restabilization* does not occur and the system shows a monotonic increase of inflection with an increase of p (upper part of Fig. 5.18, for $q_1 = 0.7$ and $\alpha = 10°$);

⋄ for $q > 1$ the imperfect system follows exactly the behaviour of the perfect system ($\alpha = 0°$, see Bigoni et al. [10]) and self-restabilization cannot occur (bottom part of Fig.5.18, for $q = 2$ and $\alpha = 5°$ or $\alpha = 10°$).
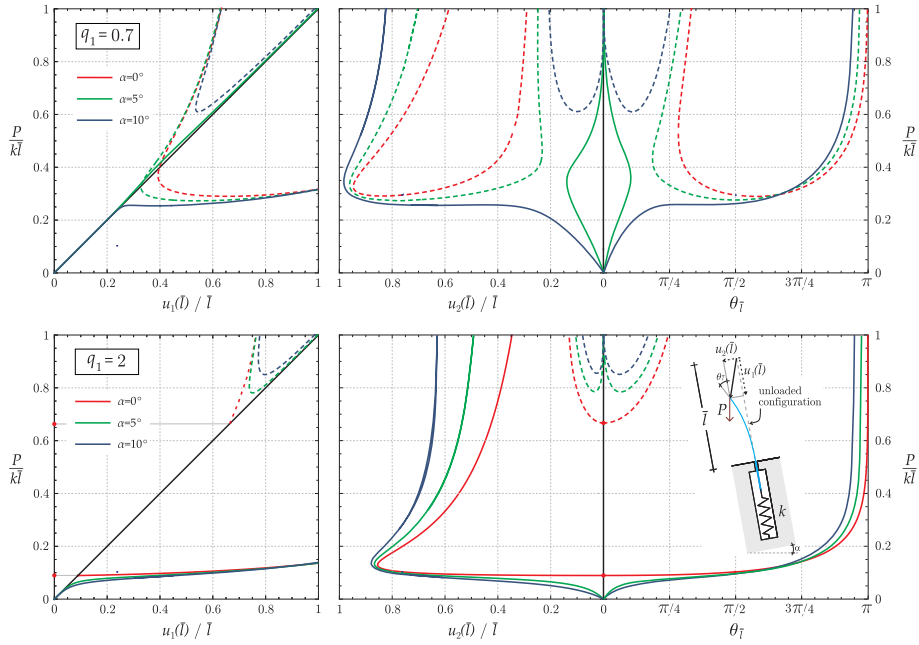
Figure 5.18: First-mode of bifurcation: deformation paths of the structure sketched in the inset, expressed as the (dimensionless) applied load versus (dimensionless) displacement components and rotation of the blade loaded edge. In every graph the path of the perfect system ($\alpha = 0°$) is reported together with the paths of the blade with two different tilt angles ($\alpha = 5°$ and $\alpha = 10°$). Note that for $q_1 = 0.6$ and $\alpha = 5°$ an asymptotic self-restabilization of the triavial undeformed configuration occurs.

Finally, considering constant geometrical and material properties of the rod (B), the reduction of elastic spring stiffness k leads to a decrease of the inflection on equal applied load P. This effect is the same noticed by Feodosiev [57], Tarnai [58] and Bigoni et al. [10] where an increase of elastic stiffness of the spring yields a decrease in the buckling load.

Stability of configurations

In order to evaluate the stability of the equilibrium configurations for the considered system, the second variation of the functional $\mathcal{V}$, equation (5.71), has to be calculated considering the boundary conditions (5.20) and the perturbations in the rotation field $\theta_{var}(s)$ and in the length l_{var} satisfying the compatibility equations (5.23). Therefore the second variation evaluated

at an equilibrium configuration can be written as

$$
\delta_\epsilon^2 \mathcal{V} = \frac{1}{2} \left\{ \left[k - 2P \sin \alpha \theta_{eq}'(l_{eq}) \right] l_{var}^2 + B \int\limits_{l_{eq}}^{\bar{l}} \left[\theta_{var}'(s) \right]^2 \mathrm{d}s \right.
$$

$$
\left. + P \int\limits_{l_{eq}}^{\bar{l}} \left(\sin \alpha \sin \theta_{eq}(s) - \cos \alpha \cos \theta_{eq}(s) \right) [\theta_{var}(s)]^2 \, \mathrm{d}s \right\}. \tag{5.80}
$$

The stability or instability of an equilibrium configuration is then related to the sign of the second variation $\delta_\epsilon^2 \mathcal{V}$, evaluated for that equilibrium configuration, as in equation (5.48), for any admissible perturbations $\theta_{var}(s)$ and l_{var} satisfying the compatibility eqns (5.23).

Considering the auxiliary function $\Gamma(s)$, solution of the following boundary value problem (the Riccati equation plus a boundary condition, see [60])

$$
\begin{cases}
\dfrac{\partial \Gamma(s)}{\partial s} - P \cos \alpha \cos \theta_{eq}(s) + P \sin \alpha \sin \theta_{eq}(s) - \dfrac{\Gamma(s)^2}{B} = 0, \\[4mm]
\Gamma(\bar{l}) = 0,
\end{cases} \tag{5.81}
$$

the compatibility equations (5.23) and the identity (5.50), the second variation, equation (5.47), can be rewritten as

$$
\delta_\epsilon^2 \mathcal{V} = \frac{1}{2} \left\{ B \int\limits_{l_{eq}}^{\bar{l}} \left[\theta_{var}'(s) + \frac{\Gamma(s)}{B} \theta_{var}(s) \right]^2 \mathrm{d}s \right.
$$

$$
\left. + l_{var}^2 \left[\theta_{eq}'(l_{eq}) \left(\theta_{eq}'(l_{eq}) \Gamma(l_{eq}) - 2P \sin \alpha \right) + k \right] \right\}. \tag{5.82}
$$

The auxiliary function $\Gamma(s)$ can be obtained through the following Jacobi transformation

$$
\Gamma(s) = -B \frac{\Lambda'(s)}{\Lambda(s)}, \tag{5.83}
$$

leading to the Jacobi boundary value problem

$$
\begin{cases}
\Lambda''(s) + \lambda^2 \left(\cos \alpha \cos \theta_{\mathrm{eq}}(s) - \sin \alpha \sin \theta_{\mathrm{eq}}(s) \right) \Lambda(s) = 0, \\[2mm]
\Lambda(\bar{l}) = 1, \\[2mm]
\Lambda'(\bar{l}) = 0.
\end{cases} \tag{5.84}
$$

The functions $\Gamma(s)$ and $\Lambda(s)$ can be obtained for a specific equilibrium configuration, defined by $\{\theta_{\mathrm{eq}}(s), l_{\mathrm{eq}}\}$, by solving the differential equations (5.81) and (5.84), so that the instability of that equilibrium configuration can be speculated when one of the following *necessary conditions* of stability $(\delta_\epsilon^2 \mathcal{V} > 0)$, obtained by Majidi et al. [41], are not satisfied:

◇ (N₁) The auxiliary function $\Gamma(s)$, solution of to the boundary-value problem (5.81), is not unbounded in the interval $\left[l_{eq}, \bar{l}\,\right]$, or, equivalently, the function $\Lambda(s)$, solution of to the differential problem (5.84), has a conjugate point to $s = \bar{l}$ in the interval $\left[l_{eq}, \bar{l}\,\right)$. [3]

◇ (N₂) The following inequality is satisfied

$$\Delta = \theta'_{eq}(l_{eq}) \left(\theta'_{eq}(l_{eq})\Gamma(l_{eq}) - 2P\sin\alpha\right) + k \geq 0. \qquad (5.85)$$

Numerical investigations of solution of the Jacobi problem (5.84), performed varying the dimensionless relative stiffness q, the dimensionless applied load p and the tilt angle α show that equilibrium configurations of the path reported with a dashed line in Fig.5.18 ($\mathcal{B}$ for systems that do not show self-restabilization and $\mathcal{A}, \mathcal{B}$ of not-restabilizing path for systems that do show self-restabilization) are unstable, due to condition N₂. All the other equilibrium paths satisfy the necessary conditions (N₁ and N₂) and therefore *could* be stable, although this cannot –for the moment– be proven and remains a theoretical open problem, even if the stability of these equilibrium configurations has been experimentally confirmed (see the experimental results presented in the next section).

Experiments

Experiments have been performed on Prototype 1, which has been already described in Section 5.5, while the angle of inclination α has been provided lifting one support of the prototype through the movable (in the vertical direction) rigid beam of an electromechanical tension-compression machine. An elastic blade of length 450 mm, realized with C62 Carbon-steel strip (25 mm x 2 mm cross section, bending stiffness $B = 2.70 \text{ Nm}^2$) has been employed. Two pair of carbon steel (EN 10270-1 SH) springs (D19100, 1 mm wire diameter and 3 mm mean coil diameter, $k = 225 \text{ N/m}$, purchased from D.I.M.) have been used. The dead load at the end of the blade has been imposed by filling (at a constant rate of 10 g/s) two containers with water and has been measured with two miniaturized Leane XFTC301 (R.C. 500N) load cell. The penetration length l_{eq} has been obtained by measuring the displacement of the lower edge of the blade through a magnetic noncontact displacement transducer GC-MK5 (from Gemac). The data have been acquired with a NI CompactDAQ system, interfaced with Labview 8.5.1 (national Instruments). Experimental results, expressed in terms of applied dimensionless load p as a function of the dimensionless amount of the blade inserted into the sliding sleeve, $l_{eq}/\bar{l}$, are reported in Fig. 5.19 for a dimensionless stiffness parametr $q_1 = 0.45$. Results reported on the top refer to a tilt angle $\alpha = 10°$, for which

---

[3]The existence of a bounded $\Gamma(s)$ on the interval $\left[l_{eq}, \bar{l}\right]$ implies that the integral in (5.82) is non-negative.

asymptotic self-restabilization occurs, whereas results reported on the bottom to a tilt angle $\alpha = 20°$, for which asymptotic self-restabilization is not shown. Experimental results (red line) have been reported together with theoretical prediction (black line), showing every nice agreement between theory and experiments.

Furthermore, a simple experiment has been performed on Prototype 1, inclined of $\alpha = 12°$ with respect to the vertical direction, hanging different load $\{24, 44, 64, 84\}$N to the blade's free edge. The length of the C62 carbon-steel strip initially external to the sliding sleeve is 470 mm, so that using the two pairs of spring of stiffnes $k = 225$ N/m, the dimensionless relative stiffness parameter is $q_1 = 0.52$. From the five photos taken with a Sony NEX 5N digital camera, equipped with 3.5-5.6/18-55 lens (optical steady shot from Sony Corporation), is clearly visible the phenomenon of asymptotic self-restabilization, because deflection of the blade is increased (up to case C)) and then decreased (cases D) and E)) with an increase of the applied vertical load. When $P = k\bar{l}$, the blade tends to return in its rectilinear undeformed configuration, because it is completely penetrated into the sleeve.

5.7.2 Penetrating blade with an imperfection of intrinsic curvature

In this section we briefly show the influence of an initial constant curvature χ_0 on the blade perfect system, Fig.5.1. The system reported in Fig.5.21 in composed of an inextensible elastic planar rod (of bending stiffness B and total length $\bar{l}$) with an initial curvature of the rod $\chi_0 = 1/r$ (where r is the radius of curvature), loaded through a dead compressive load P at its free edge and free to slide into a frictionless sleeve with inside a linear spring of stiffness k. Since the initial curvature is constant in the curvilinear coordinate of the beam, the rotation field $\theta(s)$ of the elastica of the outer part of the blade is a solution of the following differential problem

$$\begin{cases} \dfrac{\mathrm{d}^2\theta_{eq}(s)}{\mathrm{d}s^2} + \lambda^2 \sin\theta_{eq}(s) = 0, \qquad s \in \left(l_{eq}, \bar{l}\right) \\[2mm] \theta_{eq}\left(l_{eq}\right) = 0, \\[2mm] \left.\dfrac{\mathrm{d}\theta_{eq}(s)}{\mathrm{d}s}\right|_{s=\bar{l}} = \chi_0, \\[2mm] \lambda^2 = \dfrac{k}{B}l_{eq} + \dfrac{1}{2}\left[\theta'_{eq}(l_{eq})^2 - \chi_0^2\right]. \end{cases} \qquad (5.86)$$

Proceding in a standard manner as we have done in previous sections, and considering only the first bifurcation mode, once the initial curvature χ_0 is known, we obtain relation between the dimensionless load parameter λ and
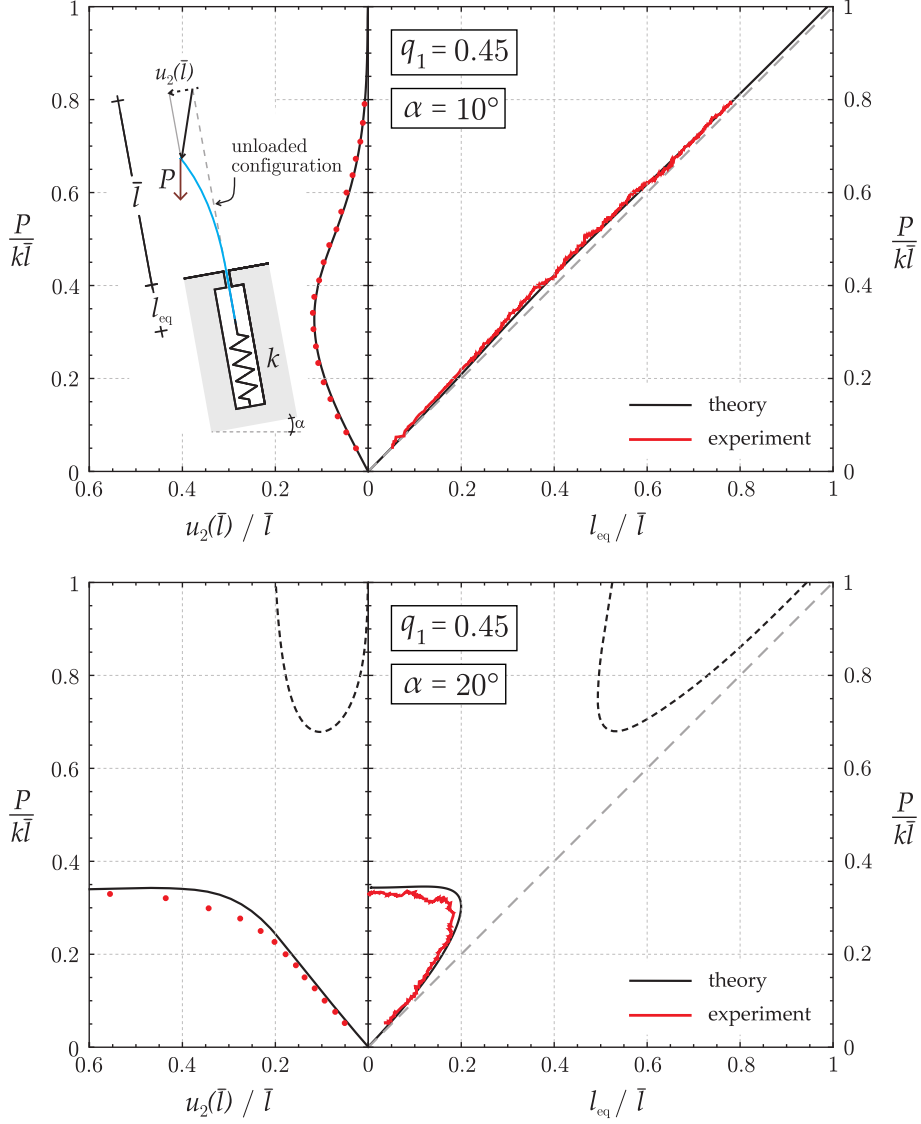
Figure 5.19: Comparison between theoretical and experimental results for the system sketched in the inset where the dimensionless load p is reported as a function of the dimensionless amount of the blade internal to the sliding sleeve $l_{eq}/\bar{l}$. On the left portion of the graphs the behaviour of the transverse dimensionless component of the blade loaded edge, $u_2\left(\bar{l}\right)/\bar{l}$, reveals that, for $\alpha = 10°$ (upper) asymptotic self-restabilization occurs, while for $\alpha = 20°$ (lower) asymptotic self-restabilization is not possible. Red dots are experimental observations not directly measured, but extracted from the video of the tests.
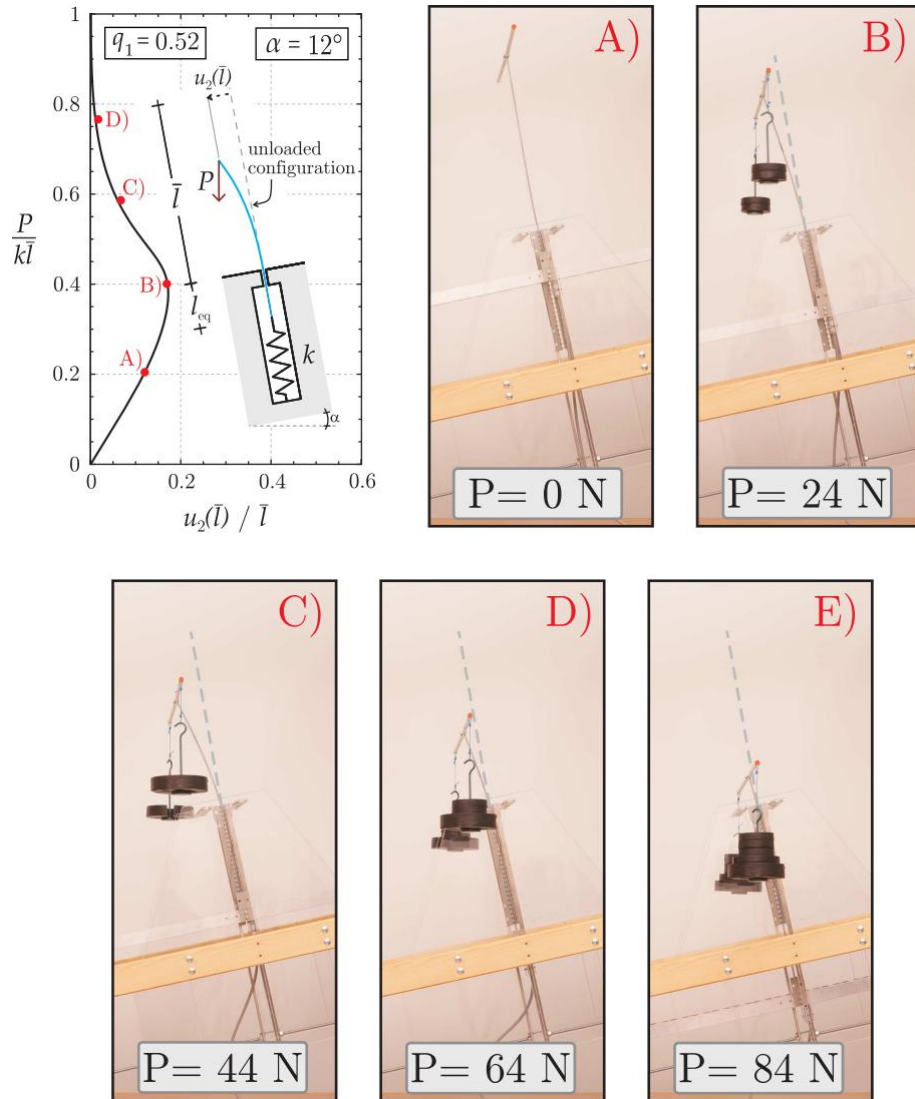
Figure 5.20: Dimensionless load parameter p as a function of the transverse dimensionless component of the blade loaded edge $u_2\left(\bar{l}\right)/\bar{l}$ for $\alpha = 12°$ and $q_1 = 0.52$ (upper-left). Five photos revealing an increase and then a decrease of deflection with an increase of the applied vertical dead load. A point that represent each photo is reported in the upper-left graph, showing the excellent agreement between theoretical predictions and experiments.
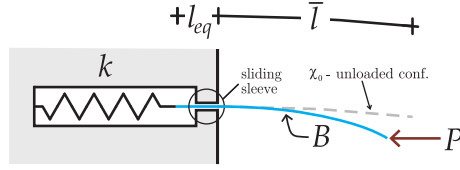
Figure 5.21: The elastic planar rod of constant bending stiffness B has a free end subject to the dead load P, while the other edge of the blade slides into a frictionless sleeve and is restrained by an axial linear spring of stiffness k. The length of the blade inside the sliding sleeve at equilibrium is l_{eq}, while the total length of the rod in its unloaded configuration is $\bar{l}$. The system is made imperfect because of the presence of an initial constant curvature χ_0.

the rotation at the rod's free end $\theta_{\bar{l}}$

$$\mathcal{K}\left(\arccos\frac{\chi_0}{2\sigma\lambda}, \sigma\right) = \lambda\left[\bar{l} - \lambda^2\frac{B}{k}\left(1 - 2\sigma^2 + \frac{\chi_0^2}{2\lambda}\right)\right] \qquad (5.87)$$

where $\sigma = \dfrac{\sqrt{2\lambda^2 - \chi_0^2 - 2\lambda^2\cos\theta_{\bar{l}}}}{2\lambda}$.
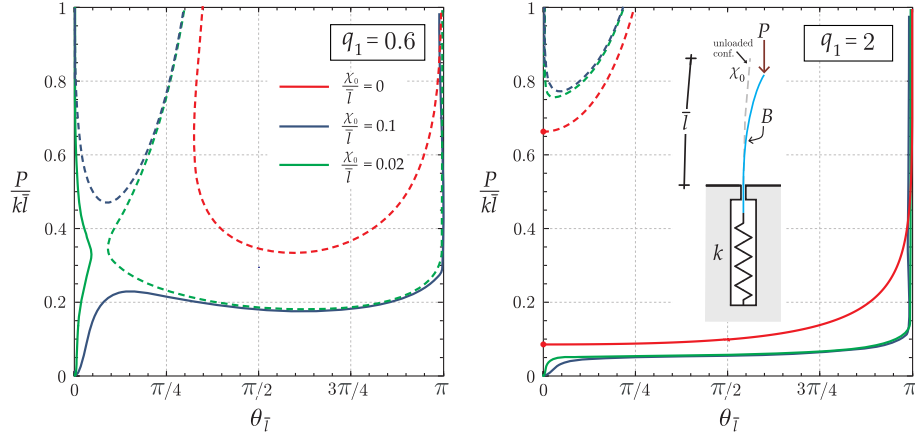
Figure 5.22: First-mode of bifurcation: deformation paths of the structure sketched in the inset, expressed as the (dimensionless) applied load versus (dimensionless) rotation of the blade loaded edge. (Left) The value of the dimensionless relative stiffness $q_1 = 0.6$ allows an asymptotic self-restabilization of the trivial loading path for low initial dimensionless curvature $\chi_0/\bar{l} = 0.02$, while for $\chi_0/\bar{l} = 0.1$ it does not occur. (Right) The system with $q_1 = 2$ follows the behaviour of the perfect blade, $\chi_0/\bar{l} = 0$, and does not show restabilization.
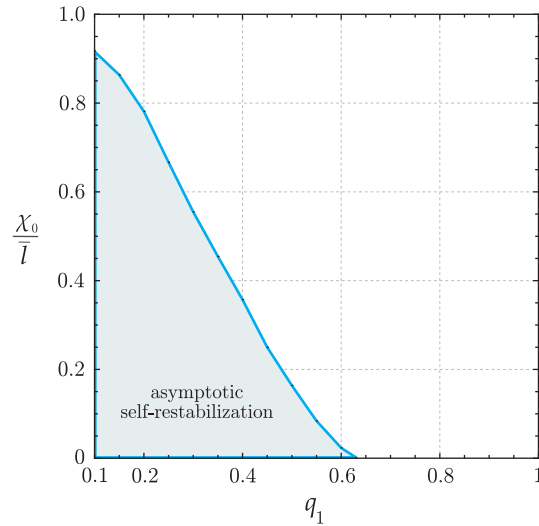

Figure 5.23: Region in the plane $q_1 - \chi_0/\bar{l}$ where asymptotic self-restabilization of the system is possible.

Chapter 6

An elastica arm scale

The concept of 'deformable arm scale' (completely different from a traditional rigid arm balance) is theoretically introduced and experimentally validated. The idea is not intuitive, but is the result of nonlinear equilibrium kinematics of rods inducing configurational forces, so that deflection of the arms becomes necessary for the equilibrium, which would be impossible for a rigid system. In particular, the rigid arms of usual scales are replaced by a flexible elastic lamina, free of sliding in a frictionless and inclined sliding sleeve, which can reach a unique equilibrium configuration when two vertical dead loads are applied. Prototypes realized to demonstrate the feasibility of the system show a high accuracy in the measure of load within a certain range of use. Moreover, they represent the first innovative application of configurational mechanics to elastic structures.

The measuring of the weight is a very common action, dating back to the earliest days of civilization. In fact, for millennia the equal and unequal arm balance scales have been used (for instance the classic Roman balance, see Fig. 6.1 left), and still are used (see the overview by Robens et al. [61]), to measure weight by exploiting equilibrium of a rigid lever, so that a deformation of the arms would merely represent an undesired effect. On the other hand, the modern digital weighting systems, inspired by the principle of the elastic balance and invented at the end of the 17th century by Robert Hooke are based on the elongation of a spring (Fig. 6.1 right), so that equilibrium is always satisfied and the weight measure is directly linked to deformation, where a counterweight is not needed. These are suitable for different technological sectors.

A new paradigm, based on exploitation of nonlinear kinematics and configurational mechanics of elastic rods, is proposed here for a scale with deformable arms, where an inflected equilibrium configuration can be exploited to measure weight. In a sense, the proposed balance is a sort of combination between a rigid arm and a spring balance, because equilibrium and deformation are both simultaneously exploited. Therefore, the concept

Figure 6.1: (Left) A classical steelyard based on rigid lever principle and (right) a spring balance based on deformation.

introduced here differs completely from that underlying traditional scale design, so that the proposed device can work *with or without a counterweight*.

The 'elastically deformable arm scale' is shown on the left of Fig. 6.2 (photo of prototype 1) as a realization of the scheme reported on the right of Fig. 6.2, where an elastic rod (inclined at an angle $\alpha \in [0, \pi/2]$ with respect to the two vertical dead loads applied at its edges) is free of sliding in a frictionless sleeve of length l^*. For given loads (P_1 and P_2), the scale admits an equilibrium configuration, possible by virtue of the flexural deformation of the arms (would these be rigid, the equilibrium would be trivially violated).

This equilibrium configuration is inherently nonlinear, as it necessarily involves the presence of configurational or 'Eshelby-like' forces [9], but can be derived from stationarity of the total potential energy in a form suitable for direct calculations. Therefore, the nonlinear equilibrium equations (Section 6.1) can be exploited to determine a load from the measure of a configurational parameter (the length a_{eq}). Considerations on the second variation of the total potential energy (Section 6.3), show that the equilibrium configurations of the scale are unstable, a feature that may enhance the precision of the load measure and that does not prevent the feasibility of the scale, as shown through realization of two 'proof-of-concept prototypes' (Section 6.5). Furthermore, a sensitivity analysis and the experiments performed on the prototypes indicate that the deformable arm balance works correctly and that can be more performing than traditional balances in certain load ranges.

6.1 Flexural equilibrium through Eshelby-like forces

The system shown in Fig. 6.2 (right) attains equilibrium because two forces exist, tangential to the sliding sleeve, which can be interpreted as 'con-
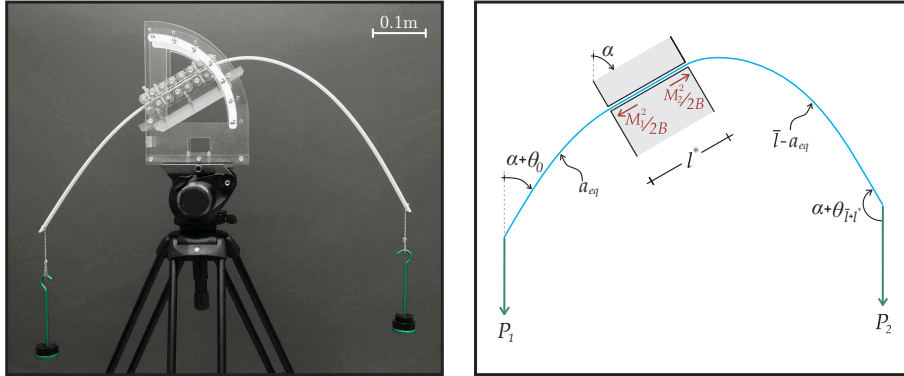
Figure 6.2: (Left) Prototype 1 and (right) scheme of the deformable arm scale. The rod used in the prototype is made up of a solid polycarbonate elastic lamina of bending stiffness $B{=}0.20$ Nm^2 and total length $\bar{l}+l^*{=}0.98$ m with ends subject to dead loads $P_1{=}2.03$ N and $P_2{=}2.52$ N. The lamina can slide into a frictionless sliding sleeve (realized with 8 roller pairs) of length $l^*{=}0.148$ m, inclined at an angle $\alpha{=}60°$ with respect to the vertical direction. The theoretical value of the length defining the equilibrium configuration is $a_{eq}{=}0.35$ m, while the value measured on the prototype is equal to 0.34 m.

figurational' (or 'Eshelby-like' [9]), in the sense that they depend on the configuration assumed by the system at equilibrium. These forces and the equilibrium conditions of the system can be obtained for an inextensible elastic lamina of bending stiffness B and total length $\bar{l}+l^*$ from the first variation of the total potential energy of the system [13]

$$
\mathcal{V}(\theta(s), a) = \int\limits_0^a B\frac{\left[\theta'(s)\right]^2}{2}\mathrm{d}s + \int\limits_{a+l^*}^{\bar{l}+l^*} B\frac{\left[\theta'(s)\right]^2}{2}\mathrm{d}s
$$
$$
- P_1\left[\cos\alpha\int\limits_0^a \cos\theta(s)\mathrm{d}s - \sin\alpha\int\limits_0^a \sin\theta(s)\mathrm{d}s\right] \tag{6.1}
$$
$$
- P_2\left[-\cos\alpha\int\limits_{a+l^*}^{\bar{l}+l^*} \cos\theta(s)\mathrm{d}s + \sin\alpha\int\limits_{a+l^*}^{\bar{l}+l^*} \sin\theta(s)\mathrm{d}s\right],
$$

where $s \in \left[0; \bar{l}+l^*\right]$ is a curvilinear coordinate, $\theta(s)$ is the rotation of the rod's axis, a and $a+l^*$, are the curvilinear coordinates at which, respectively, the left arm terminates and the right one initiates, so that $\theta(s) = 0$ for $s \in [a; a+l^*]$. The parameter a, defining the position of the rod with respect to the sliding sleeve, is variable, to be adjusted until the equilibrium configuration is reached.

Considering a small parameter ϵ and taking variations (subscript 'var') of an equilibrium configuration (subscript 'eq') in the form $\theta = \theta_{eq}(s) + \epsilon\theta_{var}(s)$

and $a = a_{eq} + \epsilon a_{var}$, four compatibility equations are obtained from a Taylor series expansion of the rotation field $\theta(\hat{s})$ for $\hat{s} = a$ and $\hat{s} = a + l^*$, namely (see [10] or Section 3.1.2 for details),

$$\theta_{var}(a_{eq}) = -a_{var}\theta'_{eq}(a_{eq}) \qquad \theta_{var}(a_{eq} + l^*) = -a_{var}\theta'_{eq}(a_{eq} + l^*),$$

$$\theta'_{var}(a_{eq}) = -\frac{1}{2}a_{var}\theta''_{eq}(a_{eq}), \quad \theta'_{var}(a_{eq} + l^*) = -\frac{1}{2}a_{var}\theta''_{eq}(a_{eq} + l^*),$$

(6.2)

once the two kinematic boundary conditions at the edges of the sliding sleeve are considered

$$\theta_{eq}(a_{eq}) = 0, \quad \theta(a_{eq} + \epsilon a_{var}) = 0, \quad \theta_{eq}(a_{eq} + l^*) = 0, \quad \theta(a_{eq} + \epsilon a_{var} + l^*) = 0.$$

(6.3)

Through integration by parts and consideration of the first two compatibility conditions (6.2) and the static conditions at the free edges, $\theta'_{eq}(0) = \theta'_{eq}(\bar{l} + l^*) = 0$, the first variation of the total potential energy (6.1) can be obtained as

$$\delta_\epsilon \mathcal{V} = -\int_0^{a_{eq}} \left[B\theta''_{eq} - P_1\big(\cos\alpha\sin\theta_{eq}(s) + \sin\alpha\cos\theta_{eq}(s)\big) \right] \theta_{var}(s)\mathrm{d}s$$

$$-\int_{a_{eq}+l^*}^{\bar{l}+l^*} \left[B\theta''_{eq} + P_2\big(\cos\alpha\sin\theta_{eq}(s) + \sin\alpha\cos\theta_{eq}(s)\big) \right] \theta_{var}(s)\mathrm{d}s \qquad (6.4)$$

$$+ \left\{ \frac{B}{2}\left[\theta'_{eq}(a_{eq}+l^*)^2 - \theta'_{eq}(a_{eq})^2 \right] - (P_1 + P_2)\cos\alpha \right\} a_{var},$$

and imposed to vanish (for every variation in the rotation field $\theta_{var}(s)$ and in the length a_{var}) to obtain the equilibrium configuration. This is governed by:

i) the elastica [15] for the two arms of the lamina

$$B\theta''_{eq}(s) - P_j\sin\left[\theta_{eq}(s) - (-1)^j\alpha\right] = 0, \qquad (6.5)$$

where $j = 1$ for the left arm ($s \in [0, a_{eq}]$) and $j = 2$ for the right one ($s \in [a_{eq} + l^*, \bar{l} + l^*]$), and

ii) the rigid-body equilibrium condition along the sliding direction of the sleeve

$$(P_1 + P_2)\cos\alpha + \underbrace{\frac{M_1^2 - M_2^2}{2B}}_{\text{Eshelby-like forces}} = 0, \qquad (6.6)$$

where $M_1 = B\theta'_{eq}(a_{eq})$ and $M_2 = B\theta'_{eq}(a_{eq} + l^*)$. The latter condition reveals the presence of two so-called 'Eshelby-like forces' [9], provided

by the sliding sleeve at its left and right ends and generated by the flexural deformation of the left and right arms, respectively, which define the equilibrium condition of the system and are the key concept of the deformable arm scale.

Following the same procedure adopted in Section 3.1.3, the rotations at the free ends at equilibrium, $\theta_0 = \theta_{eq}(0)$ and $\theta_{\bar{l}+l^*} = \theta_{eq}(\bar{l}+l^*)$, can be obtained by introduction of the auxiliary angles $\psi_1(s) = \theta_{eq}(s) + \alpha + \pi$ and $\psi_2(s) = \theta_{eq}(s) + \alpha$, for $s \in [0, a_{eq}]$ and $s \in [a_{eq} + l^*, \bar{l} + l^*]$ respectively, and double integration of the elastica (6.5), leading to the following conditions

$$a_{eq}\sqrt{\frac{P_1}{B}} = \mathcal{K}(\kappa_1) - \mathcal{K}(m_1, \kappa_1), \qquad (\bar{l} - a_{eq})\sqrt{\frac{P_2}{B}} = \mathcal{K}(\kappa_2) - \mathcal{K}(m_2, \kappa_2),$$
$$(6.7)$$

where $\mathcal{K}(\kappa_j)$ and $\mathcal{K}(m_j, \kappa_j)$ are respectively the complete and incomplete elliptic integral of the first kind

$$\mathcal{K}(\kappa_j) = \int_0^{\frac{\pi}{2}} \frac{\mathrm{d}\phi_j}{\sqrt{1 - \kappa_j^2 \sin^2 \phi_j}}, \quad \mathcal{K}(m_j, \kappa_j) = \int_{m_j}^{\frac{\pi}{2}} \frac{\mathrm{d}\phi_j}{\sqrt{1 - \kappa_j^2 \sin^2 \phi_j}}, \quad j = 1, 2.$$
$$(6.8)$$

and

$$\kappa_1 = \sin\frac{\theta_0 + \alpha + \pi}{2}, \qquad m_1 = \arcsin\left[\frac{\sin\dfrac{\alpha + \pi}{2}}{\kappa_1}\right],$$

$$\kappa_2 = \sin\frac{\theta_{\bar{l}+l^*} + \alpha}{2}, \qquad m_2 = \arcsin\left[\frac{\sin\dfrac{\alpha}{2}}{\kappa_2}\right], \qquad (6.9)$$

$$\kappa_1 \sin\phi_1(s) = \sin\frac{\theta_{eq}(s) + \alpha + \pi}{2}, \quad \kappa_2 \sin\phi_2(s) = \sin\frac{\theta_{eq}(s) + \alpha}{2}.$$

Further integration of the elastica (6.5) leads to the solution for the rotation field at equilibrium

$$\theta_{eq}(s) = \begin{cases} \pi - 2\arcsin\left[\kappa_1\mathrm{sn}\left(\mathcal{K}(\kappa_1) - \sqrt{\frac{P_1}{B}}s, \kappa_1\right)\right] - \alpha, \qquad s \in [0, a_{eq}], \\\\ 2\arcsin\left[\kappa_2\mathrm{sn}\left(\sqrt{\frac{P_2}{B}}(s - a_{eq} - l^*) + \mathcal{K}(m_2, \kappa_2), \kappa_2\right)\right] - \alpha, \\\\ \hspace{6cm} s \in [a_{eq} + l^*, \bar{l} + l^*], \\ \hspace{7cm} (6.10) \end{cases}$$

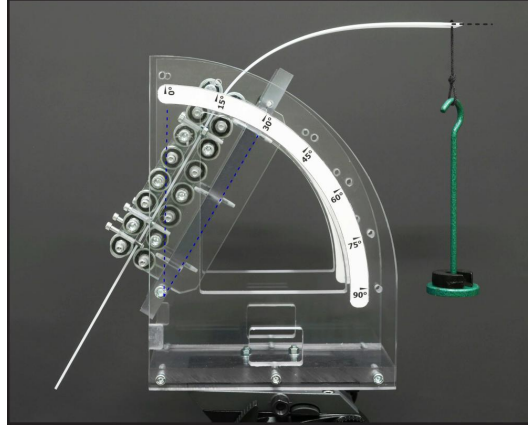where sn is the Jacobi sine amplitude function. Since the solution (6.10)

Figure 6.3: The Prototype 1 loaded in a configuration which does not need any counterweight. The rod used in the prototype is made up of a solid polycarbonate elastic lamina (inclined at an angle α=30° with respect to the vertical direction) of bending stiffness B=0.03 Nm^2 and total length $\bar{l} + l^*$=0.487 m with one end subject to a dead load P_2=1.53 N. The theoretical value of the length defining the equilibrium configuration is a_{eq}=0.128 m, while the value measured on the prototype is equal to 0.126 m.

implies

$$B\theta'_{eq}(a_{eq})^2 = 2P_1 \left[\cos(\theta_0 + \alpha) - \cos\alpha\right],$$

$$B\theta'_{eq}(a_{eq} + l^*)^2 = 2P_2 \left[\cos\alpha - \cos(\theta_{\bar{l}+l^*} + \alpha)\right],$$

(6.11)

the equilibrium along the sliding direction of the sleeve (6.6) can be expressed as a 'geometrical condition' of equilibrium, which relates the angles at the free edges to the two applied vertical dead loads as

$$P_1 \cos(\alpha + \theta_0) + P_2 \cos(\alpha + \theta_{\bar{l}+l^*}) = 0,$$

(6.12)

and represents the balance of axial thrust of the deformable scale ($0 \leq \alpha + \theta_0 \leq \alpha$ and $\pi/2 \leq \alpha + \theta_{\bar{l}+l^*} \leq \pi$).

When $\alpha + \theta_{\bar{l}+l^*} = \pi/2$ the equilibrium equation (6.12) implies $P_1 = 0$, so that *a counterweight is not needed*, Fig. 6.3.

6.2 Mode of use of the elastic scale

The following modes of use of the elastic scale can be envisaged.

⬦ The easiest way to use the elastic scale is referring to equation (6.12) and measuring the two angles θ_0 and $\theta_{\bar{l}+l^*}$. Assuming that P_1 and α are known, P_2 can be evaluated. Note that B is not needed in this mode of use.

◇ Another mode of use of the elastic scale is through the measure of the length a_{eq}. Knowing P_1, B, and α, P_2 can be determined in the following steps:

i) Equation $(6.7)_1$ gives θ_0;

ii) Equation (6.12) gives $\theta_{\bar{l}+l^*}$ as a function of the unknown P_2;

iii) Equation $(6.7)_2$ provides an equation for the unknown P_2, to be numerically solved.
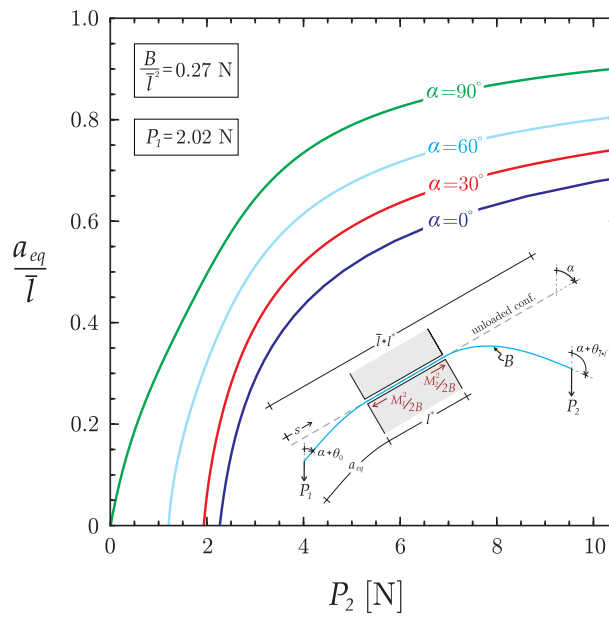

Figure 6.4: Equilibrium length a_{eq} versus weight P_2 for different inclination $\alpha = \{0; 30; 60; 90\}^{\circ}$. The values of the counterweight P_1 and the parameter $B/\bar{l}$ are the same adopted during the experiments, Section 6.6

Note that equations (6.7) define a_{eq} as a one-to-one function respectively of θ_0, equation $(6.7)_1$, and $\theta_{\bar{l}+l^*}$, equation $(6.7)_2$, while equation (6.12) defines a unique relation between θ_0 and $\theta_{\bar{l}+l^*}$ (within the limits of variability of these two angles). Therefore, if all the possible deformations of the elastica which are unstable even for clamped end are not considered, the equilibrium solution of equations (6.7) and (6.12), when it exists is unique.

In order to adopt the second mode of use (selected for the experiments), once decided the value of the counterweight P_1, the material and geometrical parameters of the lamina B and $\bar{l}$, the graph reported in Fig. 6.4 can be easily utilized to obtain the value of P_2 from the measured length a_{eq}. The inclination of the scale α can be adjusted in order to have an appropriate range of measured weight P_2 or sensitivity $\mathbb{S}$ (see Section 6.4.2). In fact, when α increases from $0°$ (vertical configuration where no counterweight is

needed) to 90° (horizontal configuration), the range of measure weight tends to increase up to the case when all possible values of P_2 are covered, namely $\alpha = 90°$.

6.3 Stability

Equilibrium configurations of the proposed mechanical system are expected to be unstable by observing that a perturbation of the system at an equilibrium position, $a = a_{eq}$, through an increase (or decrease) of a, yields a leftward (or rightward) unbalanced Eshelby-force, which tends to increase the perturbation itself. However, instability of the equilibrium configuration exploited in the deformable arm scale does not necessarily represent a drawback, as it could increase precision in the measure.

In a rigorous way, the instability of a deformed configuration can be detected by investigating the sign of the second variation of the total potential energy, which can be written as

$$
\begin{aligned}
\delta_\epsilon^2 \mathcal{V} = \frac{1}{2} \Bigg\{ & B \int_0^{a_{eq}} \left[\theta_{var}'(s) \right]^2 \mathrm{d}s + B \int_{a_{eq}+l^*}^{\bar{l}+l^*} \left[\theta_{var}'(s) \right]^2 \mathrm{d}s \\
& - \sin\alpha \left[P_1 \theta_{eq}'(a_{eq}) + P_2 \theta_{eq}'(a_{eq}+l^*) \right] a_{var}^2 \\
& + P_1 \int_0^{a_{eq}} \left(\cos\alpha \cos\theta_{eq}(s) - \sin\alpha \sin\theta_{eq}(s) \right) \theta_{var}^2(s) \mathrm{d}s \\
& + P_2 \int_{a_{eq}+l^*}^{\bar{l}+l^*} \left(\sin\alpha \sin\theta_{eq}(s) - \cos\alpha \cos\theta_{eq}(s) \right) \theta_{var}^2(s) \mathrm{d}s \Bigg\}.
\end{aligned}
\tag{6.13}
$$

The second variation, equation (6.13), becomes

$$
\begin{aligned}
\delta_\epsilon^2 \mathcal{V} = \frac{1}{2} \Bigg\{ & B \int_0^{a_{eq}} \left[\theta_{var}'(s) + \frac{\Gamma_1(s)}{B} \theta_{var}(s) \right]^2 \mathrm{d}s \\
& + B \int_{a_{eq}+l^*}^{\bar{l}+l^*} \left[\theta_{var}'(s) + \frac{\Gamma_2(s)}{B} \theta_{var}(s) \right]^2 \mathrm{d}s \\
& + \left[\Gamma_2(a_{eq}+l^*) \left[\theta_{eq}'(a_{eq}+l^*) \right]^2 - \Gamma_1(a_{eq}) \left[\theta_{eq}'(a_{eq}) \right]^2 \right. \\
& \left. - \sin\alpha \left(P_1 \theta_{eq}'(a_{eq}) + P_2 \theta_{eq}'(a_{eq}+l^*) \right) \right] a_{var}^2 \Bigg\},
\end{aligned}
\tag{6.14}
$$

when the two auxiliary functions $\Gamma_1(s)$ and $\Gamma_2(s)$ are introduced as the solutions of the following boundary value problems (for details, see 5.3)

$$
\begin{cases}
\dfrac{\partial \Gamma_1(s)}{\partial s} + P_1 \cos \alpha \cos \theta_{eq}(s) - P_1 \sin \alpha \sin \theta_{eq}(s) - \dfrac{\Gamma_1(s)^2}{B} = 0, \\[2mm]
\Gamma_1(0) = 0, \qquad\qquad\qquad\qquad\qquad\qquad s \in [0, a_{eq}],
\end{cases}
$$

$$
\begin{cases}
\dfrac{\partial \Gamma_2(s)}{\partial s} - P_2 \cos \alpha \cos \theta_{eq}(s) + P_2 \sin \alpha \sin \theta_{eq}(s) - \dfrac{\Gamma_2(s)^2}{B} = 0, \\[2mm]
\Gamma_2(\bar{l} + l^*) = 0, \qquad\qquad\qquad\qquad\quad s \in [a_{eq} + l^*, \bar{l} + l^*].
\end{cases}
$$
$$(6.15)$$

Considering the necessary condition by Majidi et al. [41], an equilibrium configuration can be stable if

$$
\begin{aligned}
\Delta = {} & \Gamma_2(a_{eq} + l^*) \left[\theta'_{eq}(a_{eq} + l^*) \right]^2 - \Gamma_1(a_{eq}) \left[\theta'_{eq}(a_{eq}) \right]^2 \\
& - \sin \alpha \left(P_1 \theta'_{eq}(a_{eq}) + P_2 \theta'_{eq}(a_{eq} + l^*) \right) \geq 0.
\end{aligned}
$$
$$(6.16)$$

Introducing the Jacobi transformation

$$
\Gamma_j(s) = -B \frac{\Lambda'_j(s)}{\Lambda_j(s)}, \qquad j = 1, 2,
$$
$$(6.17)$$

which leads to the following Jacobi boundary value problems

$$
\begin{cases}
\Lambda''_1(s) + \dfrac{P_1}{B} \left(\sin \alpha \sin \theta_{eq}(s) - \cos \alpha \cos \theta_{eq}(s) \right) \Lambda_1(s) = 0, \\[2mm]
\Lambda_1(0) = 1, \\[2mm]
\Lambda'_1(0) = 0, \qquad\qquad\qquad\qquad\qquad\qquad s \in [0, a_{eq}],
\end{cases}
$$

$$
\begin{cases}
\Lambda''_2(s) + \dfrac{P_2}{B} \left(\cos \alpha \cos \theta_{eq}(s) - \sin \alpha \sin \theta_{eq}(s) \right) \Lambda_2(s) = 0, \\[2mm]
\Lambda_2(\bar{l} + l^*) = 1, \\[2mm]
\Lambda'_2(\bar{l} + l^*) = 0, \qquad\qquad\qquad\qquad\quad s \in [a_{eq} + l^*, \bar{l} + l^*],
\end{cases}
$$
$$(6.18)$$

the auxiliary functions $\Gamma_j(s)$ with $j = 1, 2$ have been numerically evaluated for all configurations considered in the experiments and, although conjugate points are not present, the unstable character of the configurations follows from $\Delta < 0$. Note that, although the equilibrium configurations have been found to be unstable, the small friction inside the sliding sleeve allows the experimental photography of these states, as reported in Figs. 6.2 and 6.3.

6.3.1 Instability of the solution at small rotations

A general proof that all equilibrium configurations are unstable can be easily derived under the assumption of small rotations. In this case, the equilibrium configuration can be explicitly obtained as a function of the length a as

$$
\theta_{eq}(s,a) = \begin{cases} \dfrac{P_1 \sin \alpha}{2B}(s^2 - a^2), & s \in [0, a], \\[2ex] \dfrac{P_2 \sin \alpha}{2B}\left[(a + l^*)(a - l^* - 2\bar{l}) + 2(\bar{l} + l^*)s - s^2\right], & \\[2ex] & s \in [a + l^*, \bar{l} + l^*], \end{cases}
\tag{6.19}
$$

so that the total potential energy (6.1) is evaluated as

$$
\mathcal{V}(a) = -\frac{\sin^2 \alpha}{6B}\left[P_1^2 a^3 + P_2^2(\bar{l} - a)^3\right] - a\cos\alpha(P_1 + P_2).
\tag{6.20}
$$

The length a at equilibrium a_{eq} can be obtained by imposing the vanishing of the first derivative of the total potential energy (6.20), while evaluation of its second derivative at equilibrium results in the following expression

$$
\left.\frac{\partial^2 \mathcal{V}(a)}{\partial a^2}\right|_{a_{eq}} = -\sin^2\alpha\left[a_{eq}P_1^2 + (\bar{l} - a_{eq})P_2^2\right] < 0, \qquad \forall\, a_{eq} \in [0; \bar{l}],
\tag{6.21}
$$

demonstrating the instability of all the equilibrium configurations for small rotations.

6.3.2 Stable systems

Finally, it is worth noting that a deformable scale where the equilibrium configuration is stable can be easily obtained by adding to the proposed system a linear elastic spring of stiffness k, located inside the sliding sleeve (thus restraining the sliding of the elastic rod, see Chapter 5 or [10]). In this case, the stabilizing term $k(a - a_0)^2/2$ (in which a_0 is the length a in the unloaded configuration) is added to the elastic potential energy (6.1). Therefore, findings reported in this chapter pave the way to the realization of stable systems, would instability prevent the practical realization of an equilibrium configuration, which is not the case of the scale shown in the Fig. 6.2 (left), as shown below.

6.4 Sensitivity analysis and comparisons between balances

In order to appreciate the performance of the elastic arm scale, a comparison with the classical unequal arm balance (Fig. 6.1 left) is needed because it is

its hystorical predecessor, although still used nowadays in many fields. The comparison may be possible through the parameter of sensitivity, which will be adopted both to compare the elastic scale with the classical unequal arm balance and to evaluate the performances of elastic balances with different inclination angle α and bending stiffness B.

6.4.1 Steelyard

The steelyard is based on the principle of the lever between two rigid arm, so that it operates exactly as the second mode of use of the elastic scale, presented in Section 6.2. In this scale the equilibrium equation is guaranteed by the moment balance at the fulcrum

$$P_1 a_{eq} = P_2 \left(\bar{l} - a_{eq} \right), \tag{6.22}$$

where P_1 is the counterweight associated with the left arm of length a_{eq}, whereas P_2 represents the weigth (to be measured) linked with the right arm of length $\bar{l} - a_{eq}$ (see also the scheme in Fig. 6.5). Therefore, also for the unequal balance, once fixed the value of the counterweight P_1 and the total length of the rigid bar $\bar{l}$, the value of P_2 can be obtained from equation (6.22) once the length a_{eq} has been measured.

6.4.2 Sensitivity analysis

In the treatise of Robens, Jayaweera and Kiefer [61] the concept of sensitivity is associated to balances in order to compare their precision in weighing. Sensitivity, according to DIN/ISO, is defined as the response of a measuring instrument, which may be an angle or a length, divided by the corresponding change in the stimulus, that is the mass placed on it. In our case, sensitivity $\mathcal{S}$ is the quotient of the observed variation of the variable a_{eq} and the corresponding variation of the measured weight at a given weight value

$$\mathcal{S} = \frac{\partial a_{eq}}{\partial P_2}. \tag{6.23}$$

Therefore, definition (6.23) is fundamental to define a quality characteristic of a balance and for the classical steelyard, taking into account equilibrium equation (6.22), sensitivity is expressed as

$$\mathcal{S}_{\text{steelyard}} = \frac{P_1 \bar{l}}{(P_1 + P_2)^2}, \tag{6.24}$$

whereas for the elastic arm scale it should be computed numerically due to the non linearity nature of equilibrium equations (6.7) and (6.12).
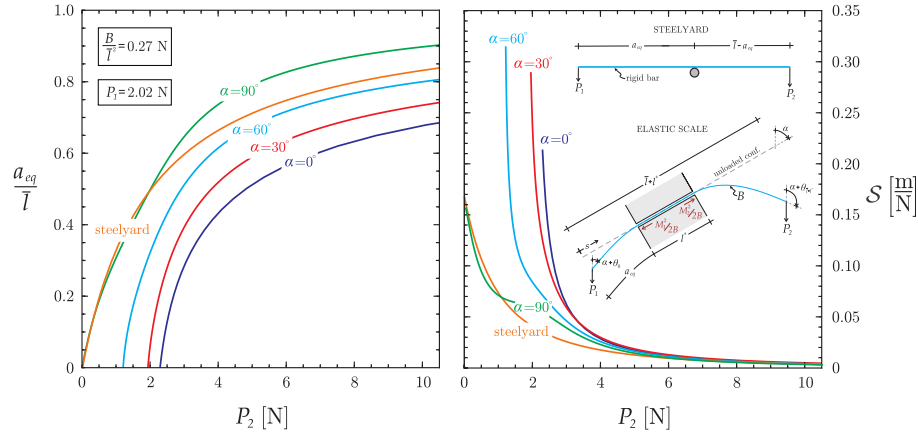
Figure 6.5: Comparison between classical steelyard and elastic scale at different inclinations $\alpha = \{0; 30; 60; 90\}^\circ$: (left) equilibrium length a_{eq} and (right) sensitivity $\mathcal{S}$ versus weight P_2. The values of the counterweight P_1 and the parameter $B/\bar{l}$ are the same adopted during the experiments, Section 6.6

6.4.3 Comparison with steelyard

A comparison between the classical unequal arm balance and our elastic scale is reported in Fig. 6.5, where the graph on the left shows the equilibrium length a_{eq} function of the unknown weight P_2, while on the right is reported the sensitivity $\mathcal{S}$, which represent the inclination of the previous graph. From the first image can be noticed that the roman balance can measure all range of weight P_2, as well as the horizontal configuration ($\alpha = 90°$) of the elastic scale, whereas the other inclined position of the flexible arm balance can not measure lightweights. Nevertheless, the sensitivity analysis proves that the inclined elastic scale is able to measure weights with an higher precision respect the rigid arm balance. In fact, on equal weight to be measured P_2, sensitivity improves with the increasing of the inclination towards the vertical configuration ($\alpha = 0°$) where no counterweight is requested and possible effects due to friction are considerably reduced.

6.4.4 Comparison with different elastic scales

Finally, a comparison between elastic scales with different bending stiffness B (in the hypothesis that the length of the flexible rod $\bar{l}$ remains constant), reported in Fig. 6.6, demonstrates that a decrease (increase) in the bending stiffness produces an increase (decrease) of the range of measured weights and an increase (decrease) in sensitivity $\mathcal{S}$. Therefore a more accurate device can be designed either reducing the rod's bending stiffness (keeping constant the length $\bar{l}$) or increasing the length $\bar{l}$ (keeping constant the material and the section properties, namely B).
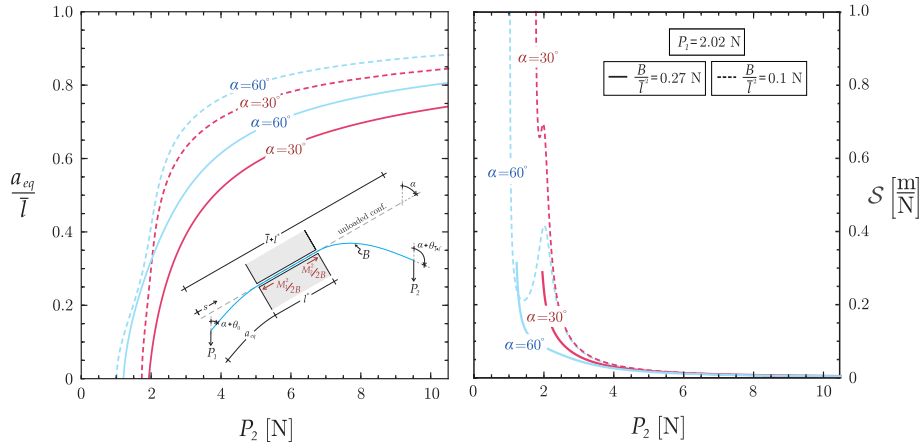
Figure 6.6: Comparison between elastic scales with different parameter $B/\bar{l}$ at two different inclinations $\alpha = \{30; 60\}^\circ$: (left) equilibrium length a_{eq} and (right) sensitivity $\mathcal{S}$ versus weight P_2.
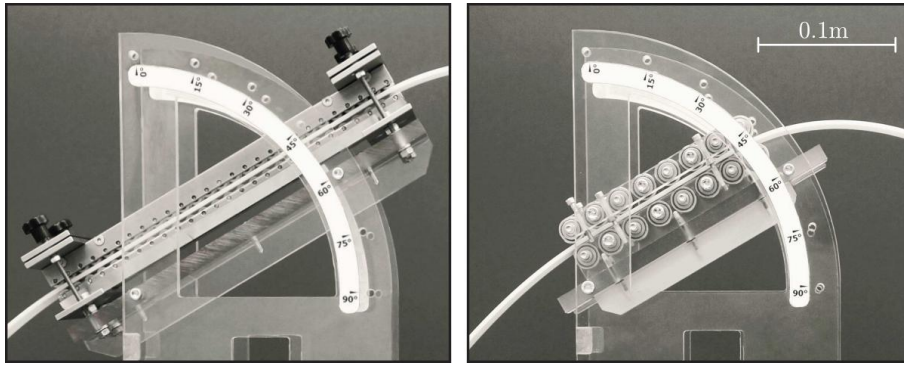

Figure 6.7: Two prototypes of the deformable arm scale: prototype 0 (left) and prototype 1 (right).

6.5 Prototypes of deformable scale

To test the possibility of realizing a deformable scale, two prototypes (called 'prototype 0' and 'prototype 1') have been designed, produced and tested (at the Instabilities Lab of the University of Trento).

In prototype 0 (shown in Fig. 6.7, left) the sliding sleeve is 296 mm in length and is made up of 27 roller pairs (each roller is a teflon cylinder 10 mm in diameter and 15 mm in length, containing two roller bearings). In prototype 1 (shown in Fig. 6.2, left, and in Fig. 6.7, right) the sliding sleeve, 148 mm in length, is realized with 8 roller (Press-Fit Straight Type, 20 mm in diameter and 25 mm in length) pairs from Misumi Europe. The tolerance between the elastic strip and the rollers inside the sliding sleeve can be calibrated with four micrometrical screws. Two elastic laminas have been realized in solid polycarbonate (white 2099 Makrolon UV from Bayer,
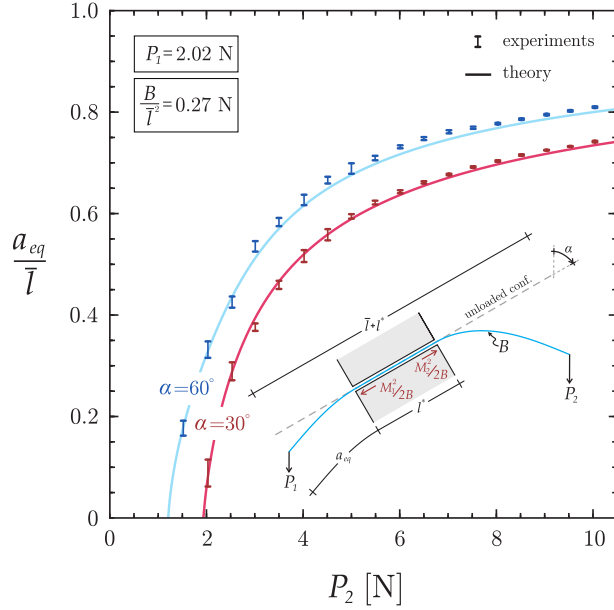
Figure 6.8: Equilibrium length a_{eq} measured on the prototype shown in Fig. 6.2 (left, at two inclinations α) for different loads P_2 versus theoretical predictions.

elastic modulus 2250 MPa), one with dimensions 980 mm × 40.0 mm × 3.0 mm and the other 487 mm × 24.5 mm × 1.9 mm; the latter has been used for the experiments reported in Fig. 6.8 and 6.9, while the former is shown in Fig. 6.2 (left). The sliding sleeve is mounted on a system (realized in PMMA) that may be inclined at different angles α. The two vertical dead loads applied at the edges of the elastic lamina have been imposed manually. The tests have been performed on an optical table (1HT-NM from Standa) in a controlled temperature $20 \pm 0.2°$ and humidity $48 \pm 0.5\%$ room. The prototypes represent proof-of-concept devices, demonstrating the feasibility of the elastic scale, with an accuracy which can be highly improved in a more sophisticated design.

6.6 Experiments

Experiments have been fulfilled both on prototype 0 and 1, but the following results are presented only for the second prototype because the results have been found to be more accurate thanks to the sliding sleeve in it, designed especially to reduce friction respect to the first prototype. Therefore, experimental results (presented in Fig. 6.8 in terms of measured values of the length a_{eq}, for different weights P_2) find an excellent agreement with the theory. The sensitivity of the scale $\mathcal{S}$ has been reported in Fig. 6.9, together with the maximum absolute error 'err' found in the experimental determination of the load P_2. The figure correctly shows that errors decrease at high sensitivity.
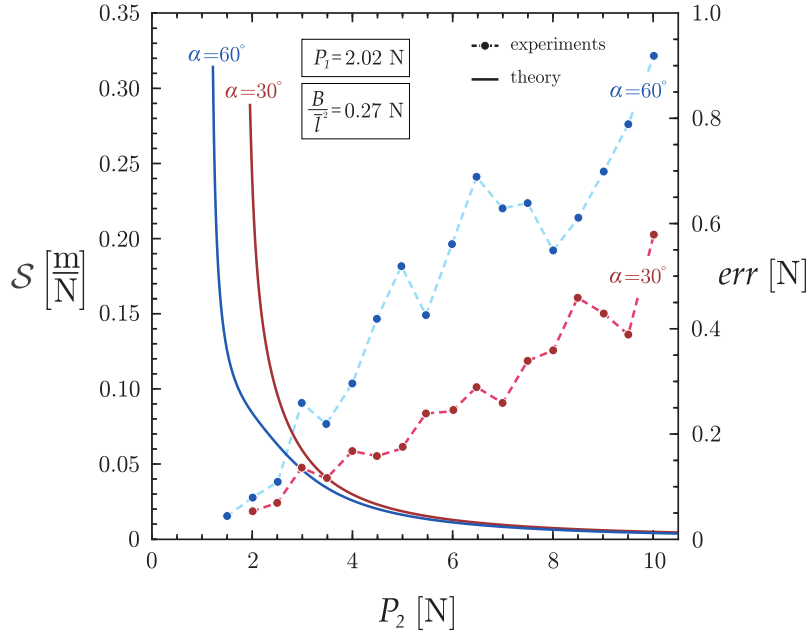
Figure 6.9: Sensitivity $\mathcal{S}$ of the deformable arm scale (at two inclinations α) as a function of the load P_2, reported together with the maximum absolute error (denoted by err) on the loads measured on the prototype shown in Fig. 6.2 (left).

Moreover, the sensitivity is so high for small P_2 that the scale could in a certain range of use become more accurate than a traditional balance, confirming what presented in Section 6.4.3. A movie with experiments on the prototypes is available at http://ssmg.unitn.it/elasticscale.html.

Finally, the reported findings represent a first step towards applications to deformable systems, in which nontrivial equilibrium configurations at high flexure can be exploited even for actuators or to realize locomotion, as will be explained in the next chapter.

Chapter 7

Torsional locomotion

The second application of configuration mechanics appears considering an elastic rod with one edge inserted into a frictionless and fitting socket head, whereas the other edge is subject to a torque, generating a uniform twisting moment. It is theoretically shown and experimentally proven that, although perfectly smooth, the constraint realizes an expulsive axial force on the elastic rod, which amount is independent of the shape of the socket head. The axial force explains why screwdrivers at high torque have the tendency to disengage from screw heads and demonstrates torsional locomotion along a perfectly smooth channel. This new type of locomotion finds direct evidence in the realization of a 'torsional gun', capable of transforming torque into propulsive force.

Motion based on self-propulsion, or locomotion, is a research topic currently attracting a strong attention in mechanics, robotics, and biology. Since pioneering studies by Gray on serpentine propulsion [62–64], elastic bending of a rod has been shown to produce an axial tractive force. Our previous results show that a motion along the channel can be induced even when the applied forces are orthogonal to it. Moreover, it has been shown in previous chapters (i.e. Chapter 3 and Chapter 6) that the Eshelby-like forces can have a magnitude comparable with the applied loads. These forces are the essence of snake and fish locomotion and must play an important role in the problem of beam snaking occurring during smart drilling of oil wells and in plumbing [65]. In fact, configurational force are related with the change in curvature, so that (in the words of Gray [64]) 'a snake cannot progress round the arc of a circle or along a perfectly straight line'. From Gray's findings, nowadays it is known that an eel cannot glide over a board without pegs, though its body may develop very large muscular waves. On the other end, the same eel is able to move forward over a board studded with smooth pegs or inside a smooth channel with changes in curvature. For this reason, the sliding sleeve employed in the realization of the elastic arm scale and considered also in [9] and [10] can be viewed as a perfectly frictionless and tight channel in which an elastic rod can move through bending, while torsion

has never been linked to locomotion.[1]

In mechanics, torsion of elastic rods is an old, but still ongoing and important research topic [66–73], which is linked in the following to locomotion through the following model problem.

A rectilinear inextensible elastic rod is subject to an applied torque at one end while the other edge is inserted into a perfectly smooth and fitting female constraint, able to react to the applied moment, Fig. 7.1 (A). For instance, the elastic rod can be realized as a blade of thin rectangular cross section inserted in a flathead screw, or as a cylindrical rod of hexagonal cross section inserted in a hex socket. In these conditions, if l is the length of the rod between the application point of the torque M and the end of the female constraint, D the torsional rigidity (product of the elastic shear modulus G and the torsion constant J_t) of the rod, the total potential energy of the system at equilibrium is

$$\mathcal{V}(l) = -\frac{M^2 l}{2D}. \tag{7.1}$$

Would the length l of the rod be fixed, nothing special follows, but, since this length is a free parameter, an 'Eshelby-like' or 'configurational' force P is obtained as negative of the derivative of the potential energy with respect to the configurational parameter, namely, the length l

$$P = -\frac{d\mathcal{V}(l)}{dl} = \frac{M^2}{2D}, \tag{7.2}$$

parallel to the axis of the rod and expelling the rod from the constraint, if not balanced. This force, nonlinear in M, was never previously noticed. It is at a first glance unexpected, because of the smoothness of the female constraint, and simply explains why a screwdriver tends to disengage from a screw head. Even more interestingly, this axial force (7.2) can be understood as a propulsive force opening new possibilities for locomotion, while previously Lavrentiev and Lavrentiev [74] and Kuznetsov et al. [75] related locomotion of snakes and fish to the possibility of a system of releasing elastic flexural energy.

7.1 The existence of the torsionally-induced axial force

The existence of the propulsive force P, equation (7.2), can be proven with a variational argument and recurring to a perturbation technique.

---

[1]The connection between configurational forces and the problem of snake locomotion may also appear clear for anyone who's ever tried to use a hand-held snake to unclog a toilet becuase of the arising of the axial reaction force (i.e. the Eshelby-like force).

7.1.1 Variational approach

The total potential energy $\mathcal{V}$ of a rod, which can slide into a frictionless sleeve, subject on the left end to an axial dead load S and on the right end to a torque M is (Fig. 7.1 (B))

$$\mathcal{V}(\theta(s), l_{in}) = D \int_{l_{in}}^{\bar{l}} \frac{\left[\theta'(s)\right]^2}{2} \mathrm{d}s - M\theta(\bar{l}) - S\,l_{in}, \qquad (7.3)$$

where s is the coordinate along the rod's axis, $\theta(s)$ is the cross section rotation in its plane, $\bar{l}$ is the total length of the rod and $l_{in} = \bar{l} - l$ defines its portion lying inside the constraint, so that the kinematical boundary condition $\theta(l_{in}) = 0$ and the statical boundary condition $\theta'(\bar{l}) = M/D$ follow.

Considering the rotation field $\theta(s)$ and the length l_{in} as the sum of the equilibrium configuration $\{\theta_{eq}(s); l_{eq}\}$ and the respective variations $\{\epsilon\theta_{var}(s); \epsilon l_{var}\}$ through a small parameter ϵ, the boundary conditions, similarly of previous chapters, define as compatibility equations

$$\theta_{var}(l_{eq}) = -\theta'_{eq}(l_{eq})l_{var} = 0,$$

$$\theta'_{var}(l_{eq}) = -\frac{1}{2}\theta''_{eq}(l_{eq})l_{var}, \qquad (7.4)$$

restricting the variations in the rotation field and in the length.

Equilibrium can be obtained by imposing the stationarity of the functional $\mathcal{V}$ to any small variation in the rotation field $\theta_{var}(s)$ and in the length l_{var}. The first variation $\delta_\epsilon\mathcal{V}$ can be obtained as

$$\delta_\epsilon\mathcal{V} = -\int_{l_{eq}}^{\bar{l}} D\theta''_{eq}(s)\theta_{var}(s)\mathrm{d}s + \left[D\frac{\theta'_{eq}(l_{eq})^2}{2} - S\right]l_{var}, \qquad (7.5)$$

so that the equilibrium equations are

$$\theta''_{eq}(s) = 0 \qquad s \in [l_{eq}, \bar{l}],$$

$$\underbrace{D\frac{\theta'_{eq}(l_{eq})^2}{2}}_{\text{Eshelby-like Force}} - S = 0, \qquad (7.6)$$

the latter providing the axial equilibrium and showing the Eshelby-like or configurational force P, equation (7.2), once the former is solved taking into account the statical boundary condition $\theta'(\bar{l}) = M/D$.
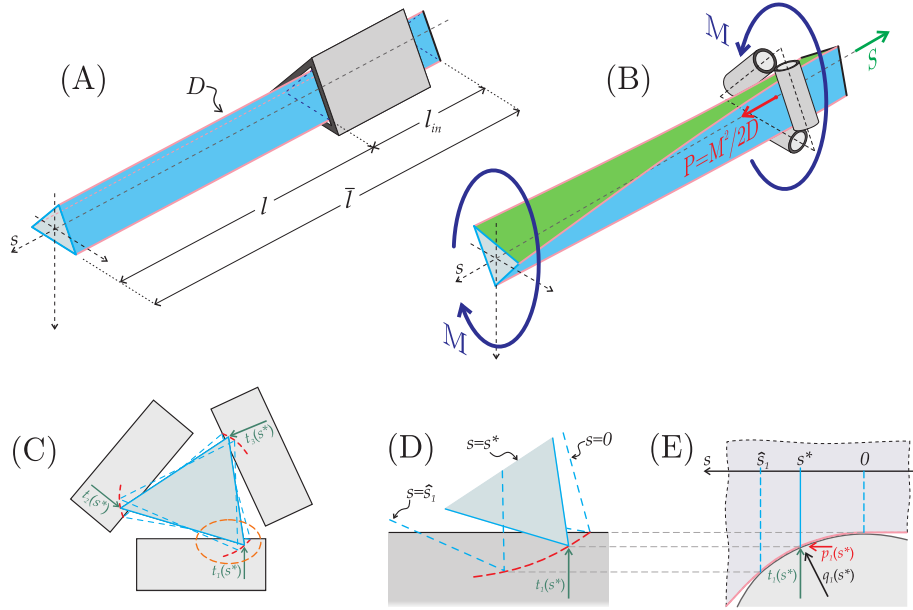
Figure 7.1: (A) Structural scheme of the elastic system employed to disclose the Eshelby-like propulsive force related to torsion; the cross section has been sketched triangular, but can have any shape capable of resisting torsion. (B) Perturbative approach to analyze the Eshelby-like propulsive force P induced by the application of the torque M: the rod is imperfectly clamped to the sliding sleeve, in the sense that there is a misfit gap and the contact is idealized as with circular rollers. (C) Front view of the elastic rod, where the misfit gap is visible between cross section and torsional constraint. (E) The imperfect fitting of the rod/sliding sleeve system yields to contact over a certain line, so that the cross section 'grasps' the rollers along this line (sketched red in the details C and D), where the reaction $q_i(s)$, orthogonal to the profile, is acting.

7.1.2 Perturbative approach

The Eshelby-like force (7.2) can be obtained by introducing the assumption that the female constraint, though perfectly frictionless, has some geometrical imperfection. In particular:

⬦ there is a gap between the rod's cross section and the female;

⬦ the profile of the female is not sharply cut, but has a curvature (sketched for simplicity as circular in Fig. 7.1 B, E).

This imperfection will be shown to lead to the configurational force $P = M^2/2D$ (independently of the misfit gap and of the female's profile) and therefore to remain unchanged in the limit when the imperfection tends to zero (differently from the propulsive forces generated by bending, Chapter 3 or [9]). This approach was introduced by Balabukh et al. [43] for a system

subjected to bending and already adopted for a demonstration of the Eshelby-like force, and is extended now to torsion where it results complicated by the 3D nature of the problem.

The elastic rod (with a polygonal cross section) of axis s is assumed to be constrained by N (equal to 3 in Fig. 7.1) smooth cylindrical rigid profiles having a plane normal to their axes containing the $s-$axis. The shape of the cross section boundary of each rigid profile (assumed circular for simplicity in Fig. 7.1 B,C,D) is described by $g_i = h_i(s)$, with $i = 1, .., N$. The contact points may vary along s, so that the contact points are defined by the set $\mathcal{C}(s)$. Considering perfectly frictionless contact, at each contact point a reaction orthogonal to the profile is acting (Fig. 7.1 C,D,E), expressed by the line force $q_i(s)$, with $i \in \mathcal{C}(s)$, with transversal component $t_i(s)$ and axial component $p_i(s)$ given by

$$p_i(s) = t_i(s)h_i'(s), \tag{7.7}$$

where a prime denotes a derivative with respect to s. The cross section of the elastic rod (triangular in Fig. 7.1), considered rigid in its plane, is subject to an internal twisting moment $m(s)$ varying along the elastic rod in the zone of contact and in equilibrium in its plane with the contact forces $t_i(s)$, so that the principle of virtual work written for an incremental torsion angle $\mathrm{d}\theta$ and corresponding incremental displacements $\mathrm{d}g_i = h_i'(s)\,\mathrm{d}s$ writes as

$$\sum_{i \in \mathcal{C}(s)} t_i(s)\,\mathrm{d}g_i = m'(s)\,\mathrm{d}\theta, \tag{7.8}$$

which, employing the constitutive equation $\mathrm{d}\theta = m(s)/D\,\mathrm{d}s$ and the definition (7.7), becomes

$$\sum_{i \in \mathcal{C}(s)} p_i(s) = \frac{\left(m^2(s)\right)'}{2D}. \tag{7.9}$$

Therefore, a propulsive force P is generated, that can be obtained as

$$P = \int_0^{\hat{s}} \sum_{i \in \mathcal{C}(s)} p_i(s)\,\mathrm{d}s, \tag{7.10}$$

where $\hat{s}$ is the point at which complete detachment from the rigid profiles occurs ($\hat{s} = \max_i\{\hat{s}_i\}$). A substitution of equation (7.9) into equation (7.10) and subsequent integration yields formula (7.2) for the propulsive force P, since $m(0) = 0$, and $m(\hat{s}) = M$ by equilibrium. Note that the thrust P is independent of the shape of the female's profile and of the amount of the initial gap, present between the rod and the smooth profiles, meaning that the amount of propulsive force, equation (7.2), is not affected by imperfections of the female constraints.

7.2 Experimental proof of the torsionally-induced axial force

The system sketched in Fig. 7.1 (B) has been realized to provide a direct experimental measure of the axial thrust P, equation (7.2). In particular, the torsional apparatus (Fig. 7.2) has been designed and manufactured at the Instabilities Lab (http://ssmg.unitn.it/) of the University of Trento. The torque M is provided through a pulley (180 mm in diameter) loaded at a constant rate with a simple hydraulic device in which water is poured into a container at 10 gr/s (the applied load is measured with a miniaturized cell from Leane, type XFTC301, R.C. 500 N). The elastic rod under twist is constrained against rotation by employing roller bearings from Misumi Europe (Press-Fit Straight Type, 20 mm in diameter and 25 mm in length), modified to reduce friction. Where the torque is applied, the elastic rod has been left free to slide axially through a double system, consisting of a linear bushing (LHGS 16-30 from Misumi Europe) mounted over a linear bearing (type Easy Rail SN22-80-500-610, from Rollon), so that longitudinal friction has been practically eliminated. The Eshelby-like force has been measured using a Gefran OC-K2D-C3 (R.C. 50 N) load cell and all data have been acquired with a NI CompactDAQ system, interfaced with Labview 8.5.1 (National Instruments). The torsional device has been mounted on an optical table (from TMC, equipped with four Gimbal piston air isolators) to prevent spurious vibrations, which have been checked to remain negligible employing two IEPE accelerometers (PCB Piezotronics Inc., model 333B50).

Experimental results, presented in Fig. 7.3 for different cross section, length, elastic modulus, and constraint condition of the elastic rod subject to torsion, fully confirm the theoretical predictions. In particular, results obtained with rods of different lengths l and different misfit gaps Δ between the rod's cross section and the female constraint (right) show unequivocally the indifference of the Eshelby-like force from these parameters. Moreover, tests have been conducted with different elastic moduli for the rod employing HDPE (high-density polyethylene) and PC (polycarbonate) and different (thin rectangular, square, triangular and trapezoidal, corresponding to $D = \{31.29; 36.37; 156.97; 638.86\}$Nm^2, respectively) cross sections left). In all cases the theoretical predictions have been found to be extremely tight to experimental results (see the movie available as electronic supplementary material for a sample of the test).

7.3 Torsional locomotion and torsional guns

Gray [62–64] has been the first to point out that a release of flexural elastic energy of a rod free of sliding in a frictionless channel can produce a locomotion force and he employed this force to explain fish and snake movement, so
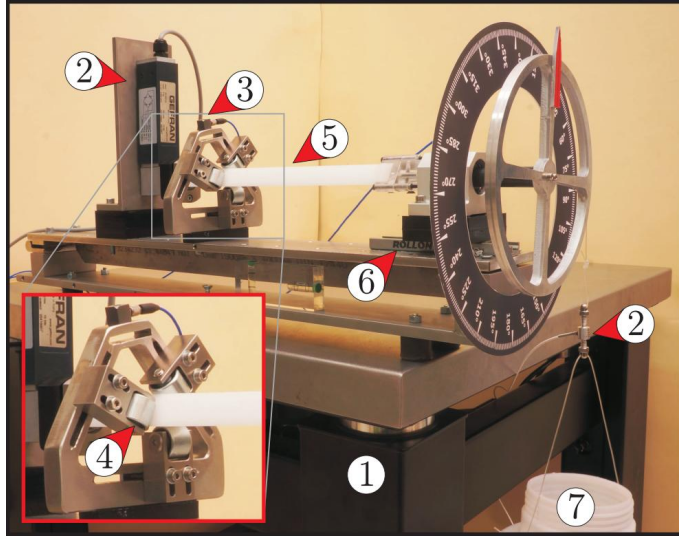
Figure 7.2: The torsional apparatus working at imposed twisting moment M, with a detail of the realization of the frictionless sleeve to constrain a rod with triangular cross section. The enumerated objects are: (1) optical table, (2) load cell, (3) accelerometer, (4) roller, (5) elastic rod, (6) axial double sliding sleeve and (7) water container.

that a snake can propel itself producing bending by the backbone and its muscles. Within the terminology introduced in the present work, the axial thrust produced during flexural deformation is the Eshelby-like force related to the release of elastic energy associated to curvature changes [11]. It is therefore obvious to conclude that the configurational force P, equation (7.2), can be interpreted as a propulsive force capable of producing longitudinal motion through the application of a torque M.

To definitely prove that a torsional deformation can generate a longitudinal propulsion, a proof-of-concept device has been developed as shown in Fig. 7.4 (A) and (B). In particular, an elastic strip (19.5 mm wide and made in PC, weight 0.62 N) has been used, realized with two pieces with different rectangular cross section (one is 1.8 mm and the other 5.3 mm thick), so that one half of the strip, called 'soft' in the following, has D_1=3.02 Nm^2, while the other, called 'stiff', has D_2=67.36 Nm^2. The elastic strip is constrained with two pairs of roller bearings (at a distance $\tilde{l} = 535$ mm) leaving possibility of axial motion, but allowing the application of a torque M or a relative rotation Θ. Initially, the elastic strip is inserted within the rollers so that the soft part of the strip has a length l_1 and the stiff one has a length $l_2 = \tilde{l} - l_1$. If a relative rotation Θ or a constant torque M is imposed between the two
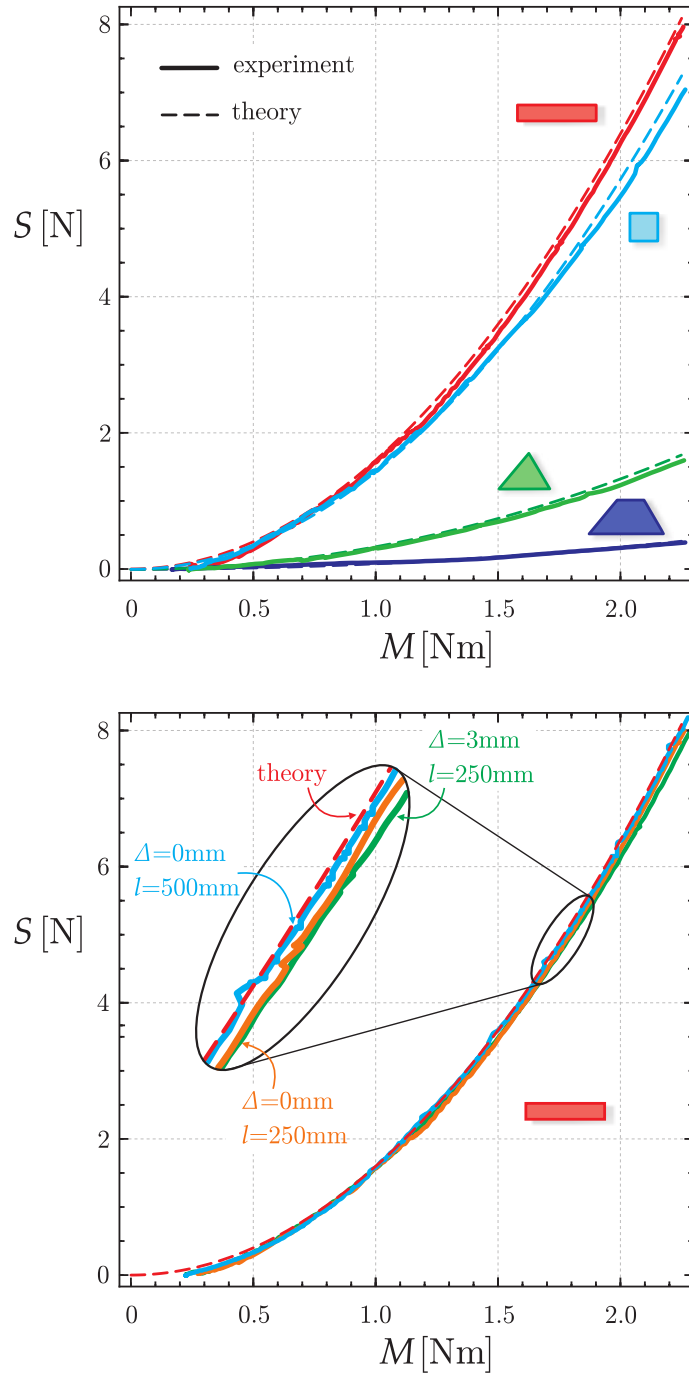
Figure 7.3: Torsionally-induced axial thrust S measured as a function of the applied torque M and compared with theoretical predictions equation (7.2) for: (upper) elastic rods differing in cross section and material (rectangular and square in PC, triangular and trapezoidal in HDPE), and (lower) elastic rods in PC with rectangular cross section having different lengths ($l = \{90; 180\}$ mm) and a null and a 3 mm misfit gap Δ.
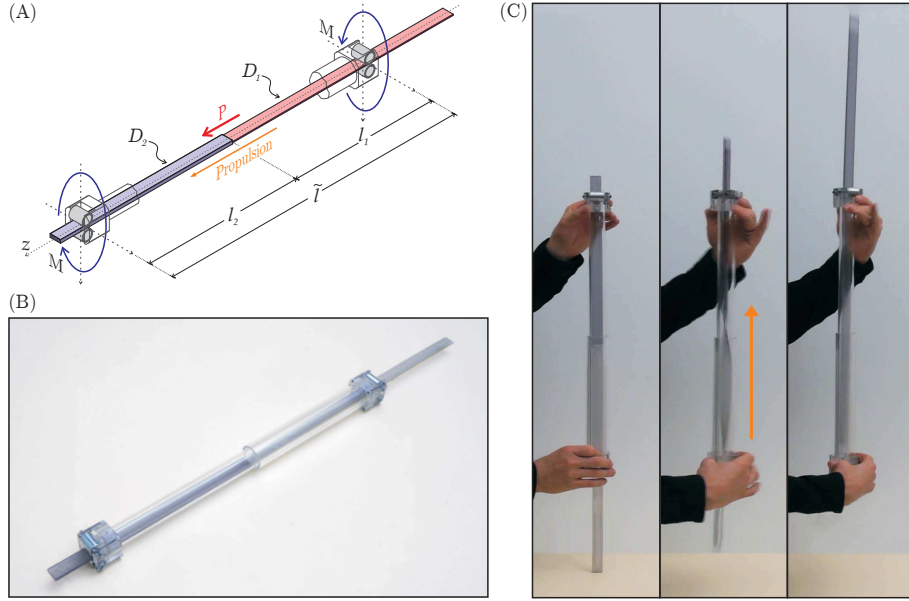
Figure 7.4: Scheme of the model (A) and photo of the prototype (B) of the torsional gun. An elastic strip made up of two laminae with different cross sections (so that one is 'stiff', D_2=67.36 Nm^2, and the other 'soft', D_1=3.02 Nm^2) is hold between two pairs of roller bearings (at a distance $\tilde{l} = 535$ mm). The system can be quickly twisted, so that a release of torsional elastic energy produces a propulsive force P enough to eject the elastic lamina. (C) The torsional gun in action: a sequence of three photos taken at 30 fps, showing that the propulsive force overcomes the gravity.

roller pairs, the total potential energy is respectively

$$\mathcal{V}(\Theta, l_1) = \frac{D_2 \Theta^2}{2\left(l_1(D2/D_1 - 1) + \tilde{l}\right)}, \quad \mathcal{V}(M, l_1) = -\frac{\left((D_2/D_1 - 1)l_1 + \tilde{l}\right) M^2}{2D_2},$$

(7.11)

so that the propulsive forces can be calculated as the negative of the derivative taken with respect to l_1

$$P(\Theta, l_1) = \frac{D_2(D_2/D_1 - 1)\Theta^2}{2\left(l_1(D_2/D_1 - 1) + \tilde{l}\right)^2}, \quad P(M) = \frac{(D_2/D_1 - 1)M^2}{2D_2}, \quad (7.12)$$

two formulas (the former holding for $l_1 < \tilde{l}$) showing that the axial thrust is constant when M is imposed while is a decreasing function of l_1 when Θ is fixed. The elastic properties of the rod affects the amount of the propulsive force P. For instance, for a material with low shear modulus G, the torsional rigidities D_1 and D_2 of the projectile would decrease, while the propulsive force P would increase (decrease) for a given twisting moment M (for an imposed angle Θ). With the employed materials and geometrical setup

143

(l_1=215 mm and l_2=320 mm) and for an imposed angle $\Theta = \pi/2$, the device realizes an initial propulsive force $P = 0.68$ N, enough to overcome gravity when the device is held in a vertical configuration.

During a manual use of the torsional gun, neither Θ, nor M, are precisely imposed, but a quick hand torsion of the device originates a propulsive longitudinal force able to eject the rod, even against gravity, see Fig. 7.4 (C) and the movie available at http://ssmg.unitn.it/torsionallocomotion.html.

Note that, differently from a bow or a catapult, in the 'torsional gun' the elastic deformation is stored in the projectile. The prototype of a torsional gun proves in an indisputable way that an axial motion can be produced via torsion, even in the absence of friction, so that a 'flat animal' can climb a frictionless narrow channel by employing a muscular torque.

Moreover, this phenomenon is ideal for development as an actuator. By using piezoelastic or thermal effects to apply a torque the actuator will produce linear motion, without the use of motors, gears or transmission mechanisms. This will lead to less complex systems, to systems without vibrations and to lighter weight system. Since the longitudinal motion only depends on the elasticity of the rod, it means that the designer can essentially choose from a very large variety of materials allowing for actuators that can be used in extreme conditions such as very high temperature or pressure, chemically aggressive environments, vacuum etc, for both aerospace applications or nanotechnology.

Bibliography

[1] J.D. Eshelby. "The force on an elastic singularity". In: *Phil. Trans. Roy. Soc. London A* 244.877 (1951), pp. 87–112. DOI: 10.1098/rsta.1951.0016 (cit. on pp. 1, 43).

[2] J.D. Eshelby. "The continuum theory of lattice defects". In: *Solid State Phys.* 3.C (1956), pp. 79–144. DOI: 10.1016/S0081-1947(08)60132-0 (cit. on pp. 1, 43).

[3] J.D. Eshelby. "Energy relations and the energy-momentum tensor in continuum mechanics". In: *Inelastic Behaviour of Solids* (1970). Ed. by M.F. Kanninien et al., pp. 17–115 (cit. on pp. 1, 43).

[4] J.D. Eshelby. "The elastic energy-momentum tensor". In: *Journal of Elasticity* 5.3-4 (1975), pp. 321–335. DOI: 10.1007/BF00126994 (cit. on pp. 1, 43).

[5] M.E. Gurtin. *Configurational forces as basic concept of continuum physics*. Berlin, Heidelberg, New York: Springer, 2000 (cit. on pp. 1, 43).

[6] R. Kienzler and G. Herrmann. *Mechanics in Material Space*. Berlin, Heidelberg, New York: Springer, 2000 (cit. on pp. 1, 43).

[7] G.A. Maugin. *Material Inhomogeneities in Elasticity*. Ed. by Chapman and Hall/CRC. Vol. 3. Applied Mathematics and Mathematical Computation. London: Springer, 1993 (cit. on pp. 1, 43).

[8] G.A. Maugin. *Configurational forces: Thermodynamics, physics, mathematics and numerics*. Ed. by Chapman and Hall/CRC. Modern Mechanics and Mathematics. New York: Taylor and Francis Ltd, 2011 (cit. on pp. 1, 43).

[9] D. Bigoni et al. "Eshelby-like forces acting on elastic structures: theoretical and experimental proof". In: *Mech. Materials* 80 (2015), pp. 368–374. DOI: 10.1016/j.mechmat.2013.10.009. URL: http://www.ing.unitn.it/~bigoni/paper/eshelbylikeforcesMoM2013.pdf (cit. on pp. 1, 59, 86, 120–122, 135, 138).

[10] D. Bigoni et al. "Instability of a penetrating blade". In: *J. Mech. Phys. Solids* 64 (2014), pp. 411–425. DOI: `10.1016/j.jmps.2013.12.008`. URL: `http://www.ing.unitn.it/~bigoni/paper/bladestabilityJMPS2014. pdf` (cit. on pp. 2, 110, 111, 122, 128, 135).

[11] F. Bosi et al. "An Elastica Arm Scale". In: *Proc. Roy. Soc. A* 470.2169 (2014). DOI: `10.1098/rspa.2014.0232`. URL: `http://www.ing.unitn. it/~bigoni/paper/elastic_scale_bosi_misseroni_dalcorso_ bigoni.pdf` (cit. on pp. 5, 141).

[12] D. Bigoni et al. "Torsional locomotion". In: *Proc. Roy. Soc. A* 470.2171 (2014), p. 20140599. DOI: `10.1098/rspa.2014.0599`. URL: `http:// rspa.royalsocietypublishing.org/content/470/2171/20140599. full` (cit. on p. 6).

[13] D. Bigoni. *Nonlinear solid mechanics. Bifurcation theory and material instability.* Cambridge, UK: Cambridge University Press, 2012 (cit. on pp. 7, 51, 60, 82, 93, 121).

[14] S.P Timoshenko and J.M. Gere. *Theory of elastic stability.* New York: McGraw-Hill, 1961 (cit. on p. 7).

[15] A.E.H. Love. *A treatise on the mathematical theory of elasticity.* Vol. 158. Fourth Edition. Cambridge: Cambridge university Press, 1927 (cit. on pp. 7, 17, 35, 51, 60, 122).

[16] E.L. Reiss. "Column buckling: An elementary example of bifurcation". In: *Bifurcation theory and nonlinear eigenvalue problems.* Ed. by J.B. Keller and S. Antman. New York: W.A. Benjamin Inc., 1969, pp. 1–16 (cit. on pp. 7, 15, 18).

[17] C.Y. Wang. "Post-buckling of a clamped-simply supported elastica". In: *Int. J. Nonlinear Mech.* 32.6 (1997), pp. 1115–1122. DOI: `10.1016/ S0020-7462(01)00072-5` (cit. on p. 7).

[18] M.A. Vaz and D.F.C. Silva. "Post-buckling analysis of slender elastic rods subjected to terminal forces". In: *Int. J. Nonlinear Mech.* 38 (2003), pp. 483–492. DOI: `10.1016/S0020-7462(01)00072-5` (cit. on p. 7).

[19] Y. Mikata. "Complete solution of elastica for a clamped-hinged beam, and its applications to a carbon nanotube". In: *Acta Mech.* 190 (2007), pp. 133–150. DOI: `10.1007/s00707-006-0402-z` (cit. on pp. 7, 27).

[20] O.M O'Reilly and D.M Peters. "On Stability Analysis of Three Classical Buckling Problems for the Elastic Strut". In: *J. Elast.* 105.1-2 (2011), pp. 117–136. DOI: `10.1007/s10659-010-9299-9` (cit. on p. 7).

[21] O.M O'Reilly and D.M Peters. "Nonlinear stability criteria for tree-like structures composed of branched elastic rods". In: *Proc. Roy. Soc. A* 468 (2012), pp. 206–226. DOI: `10.1098/rspa.2011.0291` (cit. on p. 7).

[22] J.H. Maddocks. "Stability of nonlinear elastic rods". In: *Arch. Rat. Mech. Analysis* 85.4 (1984), pp. 311–354. DOI: 10.1007/BF00275737 (cit. on pp. 7, 20, 34).

[23] R. S. Manning, K. A. Rogers, and J. H. Maddocks. "Isoperimetric conjugate points with application to the stability of DNA minicircles". In: *Proc. Roy. Soc. A* 454.1980 (1998), pp. 3047–3074. DOI: 10.1098/rspa.1998.0291 (cit. on pp. 7, 31, 37).

[24] K. A. Hoffman, R. S. Manning, and R. C. Paffenroth. "Calculation of the stability index in parameter-dependent calculus of variations problems: buckling of a twisted elastic strut". In: *SIAM J. Appl. Dyn. Syst.* 1.1 (2002), pp. 115–145. DOI: 10.1137/S1111111101396622 (cit. on pp. 7, 31, 37).

[25] R. S. Manning. "Conjugate points revisited and Neumann-Neumann problems". In: *SIAM Review* 51.1 (2009), pp. 193–212. DOI: 10.1137/060668547 (cit. on pp. 7, 37).

[26] R. S. Manning. "A catalogue of stable equilibria of planar extensible or inextensible elastic rods for all possible dirichlet boundary conditions". In: *J. Elast.* 115.2 (2014), pp. 105–130. DOI: 10.1007/s10659-013-9449-y (cit. on pp. 7, 37).

[27] V.M. Kuznetsov and S.V. Levyakov. "Secondary loss of stability of an euler rod". In: *J. Appl. Mech. Tech. Phy.* 40.6 (1999), pp. 1161–1162. DOI: 10.1007/BF02469190 (cit. on p. 7).

[28] S.V. Levyakov. "States of equilibrium and secondary loss of stability of a straight rod loaded by an axial force". In: *J. Appl. Mech. Tech. Phy.* 42.2 (2001), pp. 321–327. DOI: 10.1023/A:1018844423385 (cit. on p. 7).

[29] V.M. Kuznetsov and S.V. Levyakov. "Complete solution of the stability problem for elastica of Euler's column". In: *Int. J. Non-Linear Mech.* 37.6 (2002), pp. 1003–1009. DOI: 10.1016/S0020-7462(00)00114-1 (cit. on pp. 7, 20, 34).

[30] M. Jin and Z.B. Bao. "Sufficient conditions for stability of Euler elasticas". In: *Mech. Res. Commun.* 35 (2008). Ed. by Elsevier, pp. 193–200. DOI: 10.1016/j.mechrescom.2007.09.001 (cit. on p. 7).

[31] S.V. Levyakov. "Stability analysis of curvilinear configurations of an inextensible elastic rod with clamped ends". In: *Mech. Res. Commun.* 36 (2009), pp. 612–617. DOI: 10.1016/j.mechrescom.2009.01.005 (cit. on p. 7).

[32] S.V. Levyakov and V.M. Kuznetsov. "Stability analysis of planar equilibrium configurations of elastic rods subjected to end loads". In: *Acta Mech.* 211.1-2 (2010), pp. 73–87. DOI: 10.1007/s00707-009-0213-0 (cit. on pp. 7, 37).

[33] Sachkov Y.L. and S.V. Levyakov. "Stability of inflectional elasticae centered at vertices or inflection points". In: *Proc. Stelkov Inst. Math.* 271.1 (2010), pp. 177–192. DOI: 10.1134/S0081543810040140 (cit. on pp. 7, 20).

[34] A. Broman. *Introduction to Partial Differential Equations: From Fourier Series to Boundary-Value Problems*. Addison-Wesley series in applied Mathematics. London: Addison-Wesley, 1970 (cit. on pp. 13, 32, 83).

[35] N.M. Temme. *Special functions*. New York: John Wiley and Sons, 1996 (cit. on pp. 14, 15).

[36] P.F. Byrd and M.D. Friedman. *Handbook of elliptic integrals for engineers and scientists*. Berlin: Springer-Verlag, 1954 (cit. on pp. 15–18, 28).

[37] G. Domokos. "Global description of elastic bars". In: *Z. Angew. Math. Mech.* 74 (2007), T289–T291 (cit. on p. 30).

[38] C. Dascalu, G.A. Maugin, and C. Stolz. *Defect and Material Mechanics*. Springer, 2010 (cit. on p. 43).

[39] D. Bigoni and L. Deseri. *Recent Progress in the Mechanics of Defects*. Ed. by D. Bigoni and L. Deseri. Springer, 2011 (cit. on p. 43).

[40] C Majidi. "Remarks on formulating an adhesion problem using Euler's elastica". In: *Mech. Res. Comm.* 34.1 (2007), pp. 85–90. DOI: 10.1016/j.mechrescom.2006.06.007 (cit. on pp. 49, 78).

[41] C. Majidi, O.M. O'Reilly, and J.A. Williams. "On the stability of a rod adhering to a rigid surface: Shear-induced stable adhesion and the instability of peeling". In: *J. Mech. Phys. Solids* 60.5 (2012), pp. 827–843. DOI: 10.1016/j.jmps.2012.01.015 (cit. on pp. 49, 50, 78, 85, 91, 112, 127).

[42] L.W. He et al. "Directional adhesion behavior of a single elastic fiber". In: *J. Appl. Phys.* 112.1 (2012), p. 013516. DOI: 10.1063/1.4733331 (cit. on p. 49).

[43] L.I. Balabukh et al. "On work done by reaction forces of moving supports". In: *Research on Theory of Constructions*. Vol. 18. Moscow, 1970, pp. 190–200 (cit. on pp. 49, 86, 138).

[44] R. Courant and D. Hilbert. *Methods of Mathematical Physics*. Vol. II. New York: J. Wiley and Sons, 1962 (cit. on pp. 50, 51, 85, 86).

[45] A. Humer. "Elliptic integral solution of the extensible elastica with a variable length under a concentrated force". In: *Acta Mech.* 222 (2011), pp. 209–223. DOI: 10.1007/s00707-011-0520-0 (cit. on pp. 59, 67, 71, 73, 74).

[46]   A. Humer and H. Irschik. "Large deformation and stability of an extensible elastica with an unknown length". In: *Int. J. Solids Structures* 48 (2011), pp. 1301–1310. DOI: `10.1016/j.ijsolstr.2011.01.015` (cit. on p. 59).

[47]   W.-C. Ro, J.-C. Chen, and S.-Y. Hong. "Vibration and stability of a constrained elastica with variable length". In: *Int. J. Solids Structures* 47 (2010), pp. 2143–2154. DOI: `10.1016/j.ijsolstr.2010.04.015` (cit. on p. 59).

[48]   W.-C. Ro, J.-C. Chen, and S.-Y. Hong. "Deformation and stability of an elastica subjected to an off-axis point constraint". In: *J. Appl. Mech.* 77 (2010), p. 031006. DOI: `10.1115/1.4000426` (cit. on p. 59).

[49]   D. Zaccaria et al. "Structures buckling under tensile dead load". In: *Proc. Roy. Soc. A* 467.2130 (2011). DOI: `10.1098/rspa.2010.0505` (cit. on p. 77).

[50]   J. Shim et al. "Buckling-induced encapsulation of structured elastic shells under pressure". In: *Proc. Natl. Acad. Sci. U.S.A.* 109.16 (2012), pp. 5978–5983. DOI: `10.1073/pnas.1115674109` (cit. on p. 77).

[51]   D. Bigoni et al. "Effects of the constraint's curvature on structural instability: tensile buckling and multiple bifurcations". In: *Proc. Roy. Soc. A* 468.2144 (2012), pp. 2191–2209. DOI: `10.1098/rspa.2011.0732`. URL: `http://www.ing.unitn.it/~bigoni/paper/curvature_buckling_26-1-2012.pdf` (cit. on pp. 77, 101).

[52]   D. Bigoni and G. Noselli. "Experimental evidence of flutter and divergence instabilities induced by dry friction". In: *J. Mech. Phys. Solids* 59.10 (2011), pp. 2208–2226. DOI: `10.1016/j.jmps.2011.05.007`. URL: `http://www.ing.unitn.it/~bigoni/paper/flutter_by_friction_bigoni_noselli.pdf` (cit. on p. 77).

[53]   E.P. Chan et al. "Surface Wrinkles for Smart Adhesion". In: *Advanced Materials* 20 (2008), pp. 711–716. DOI: `10.1002/adma.200701530` (cit. on p. 77).

[54]   J.A. Rogers, T. Someya, and Y. Huang. "Materials and mechanics for stretchable electronics". In: *Science* 327.5973 (2010), pp. 1603–1607. DOI: `10.1126/science.1182383` (cit. on p. 77).

[55]   K. Bertoldi and M.C. Boyce. "Mechanically triggered transformations of phononic band gaps in periodic elastomeric structures". In: *Phys. Rev. B* 77.5 (2008), p. 052105. URL: `10.1103/PhysRevB.77.052105` (cit. on p. 77).

[56]   J. Li et al. "Switching periodic membranes via pattern transformation and shape memory effect". In: *Soft Matter* 8.40 (2012), pp. 10322–10328. DOI: `10.1039/c2sm25816a` (cit. on p. 77).

[57]   V.I. Feodosyev. *Selected Problems and Questions in Strength of Materials*. Moscow: MIR, 1977 (cit. on pp. 77, 83, 111).

[58]   J. Tarnai. "Destabilizing effect of additional restraint on elastic bar structures". In: *Int. J. Mech. Sci.* 22.6 (1980), pp. 379–390. DOI: `10.1016/0020-7403(80)90054-5` (cit. on pp. 77, 83, 111).

[59]   M. Potier-Ferry. "Foundations of elastic postbuckling theory". In: *Buckling and Post-Bucklings*. Ed. by J. Arbocz et al. Vol. 288. Lecture Notes in Physics. Springer Berlin Heidelberg, 1987, pp. 1–82. DOI: `10.1007/BFb0009197` (cit. on pp. 78, 93).

[60]   B. Van Brunt. *The calculus of variations*. Springer, 2005 (cit. on pp. 91, 112).

[61]   E. Robens, S.A.A. Jayaweera, and S. Kiefer. *Balances. Instruments, Manufacturers, History*. Springer Berlin Heidelberg, 2014 (cit. on pp. 119, 129).

[62]   J. Gray. "The mechanism of locomotion in snakes". In: *J. Exp. Biol.* 23 (1946). Ed. by Pennwell, pp. 101–120 (cit. on pp. 135, 140).

[63]   J. Gray and H.W. Lissmann. "The kinetics of locomotion of the grass-snake". In: *J. Exp. Biol.* 26 (1950). Ed. by Pennwell, pp. 354–367 (cit. on pp. 135, 140).

[64]   J. Gray. *How animals move*. Cambridge, UK: Cambridge University Press, 1953 (cit. on pp. 135, 140).

[65]   J. Beckman. "Smart snake well achieves record flow for BSP off Brunei". In: *Offshore (Conroe, Tex.)* 66.4 (2006). Ed. by Pennwell, pp. 44–47. URL: `http://www.refdoc.fr/Detailnotice?idarticle=6656286` (cit. on p. 135).

[66]   R. De Pascalis, M. Destrade, and G. Saccomandi. "The stress field in a pulled cork and some subtle points in the semi-inverse method of nonlinear elasticity". In: *Proc. Roy. Soc. A* 463.2087 (2007), pp. 2945–2959. DOI: `10.1098/rspa.2007.0010` (cit. on p. 136).

[67]   A. Dorfmann and R.W. Ogden. "Nonlinear magnetoelastic deformations of elastomers". In: *Acta Mechanica* 167.1-2 (2004), pp. 13–28. DOI: `10.1007/s00707-003-0061-2` (cit. on p. 136).

[68]   A. Goriely and S. Neukirch. "Mechanics of Climbing and Attachment in Twining Plants". In: *Phys. Rev. Lett.* 97.1-2 (2006), p. 184302. DOI: `10.1103/PhysRevLett.97.184302` (cit. on p. 136).

[69]   E. Kirkinis and R.W. Ogden. "On Extension and Torsion of a Compressible Elastic Circular Cylinder". In: *Math. Mech. Solids* 7.4 (2002), pp. 373–392. DOI: `10.1177/108128028476` (cit. on p. 136).

[70]   T. McMillen and A. Goriely. "Tendril Perversion in Intrinsically Curved Rods". In: *Journal of Nonlinear Science* 12.3 (2002), pp. 241–281. DOI: `10.1007/s00332-002-0493-1` (cit. on p. 136).

[71]   S. Neukirch. "Extracting DNA Twist Rigidity from Experimental Supercoiling Data". In: *Phys. Rev. Lett.* 93.19 (2004), p. 198107. DOI: `10.1103/PhysRevLett.93.198107` (cit. on p. 136).

[72]   E. Shmoylova, S. Potapenko, and A. Dorfmann. "Weak solutions to anti-plane boundary value problems in a linear theory of elasticity with microstructure". In: *Arch. Mech.* 59.6 (2007), pp. 539–519 (cit. on p. 136).

[73]   G.H.M. Van Der Heijden, M.A. Peletier, and R. Planque. "On end rotation for open rods undergoing large deformations". In: *Quart. Appl. Math.* 65.2 (2007), pp. 385–402. DOI: `10.1090/S0033-569X-07-01049-X` (cit. on p. 136).

[74]   M.A. Lavrentiev and M.M. Lavrentiev. "On a principle for creating a tractive force of motion". In: *J. Apppl. Mech. and Tech. Physics* 4 (1962). in Russian (cit. on p. 136).

[75]   V.M. Kuznetsov, B.A. Lugovtsov, and Y.N. Sher. "On the motive mechanism of snakes and fish". In: *Arch. Rat. Mech. Analysis* 25.5 (1967), pp. 367–387. DOI: `10.1007/BF00291937` (cit. on p. 136).